Computational Structure Analysis of Multicomponent Oxides

by

Yoyo Hinuma

Submitted to the Department of Materials Science and Engineering
in partial fulfillment of the requirements for the degree of

Doctor of Philosophy in Materials Science and Engineering

at the

MASSACHUSETTS INSTITUTE OF TECHNOLOGY

June 2008

Author . . . . . .
Department of Materials Science and Engineering
April 10, 2008

Certified by . . . . . .
Gerbrand Ceder
R. P. Simmons Professor of Materials Science and Engineering
Thesis Supervisor

Accepted by . . . . . .
Samuel Miller Allen
POSCO Professor of Physical Metallurgy
Chair, Department Committee on Graduate Students

Computational Structure Analysis of Multicomponent Oxides

by

Yoyo Hinuma

Submitted to the Department of Materials Science and Engineering
on April 10 in partial fulfillment of the requirements for the degree of
Doctor of Philosophy in Materials Science and Engineering

Abstract

First principles density functional theory (DFT) energy calculations combined with the cluster expansion and Monte Carlo techniques are used to understand the cation ordering patterns of multicomponent oxides. Specifically, the lithium ion battery cation material $LiNi_{0.5}Mn_{0.5}O_2$ and the thermoelectric material P2-Na_xCoO_2 ($0.5 \leq x \leq 1$) are investigated in the course of this research. It is found that at low temperature the thermodynamically stable state of $LiNi_{0.5}Mn_{0.5}O_2$ has almost no Li/Ni disorder between the Li-rich and transition metal-rich (TM) layer, making it most suitable for battery applications. Heating the material above ~600^{o}C causes an irreversible transformation, which yields a phase with 10~12% Li/Ni disorder and partial disorder of cations in the TM layer. Phase diagrams for the Na_xCoO_2 system were derived from the results of calculations making use of both the Generalized Gradient Approximation (GGA) to DFT and GGA with Hubbard U correction (GGA+U). This enabled us to study how hole localization, or delocalization, on Co affects the ground states and order-disorder transition temperatures of the system. Comparison of ground states, *c* lattice parameter and Na1/Na2 ratio with experimental observations suggest that results from the GGA, in which the holes are delocalized, matches the experimental results better for $0.5 \leq x \leq 0.8$. We also present several methodological improvements to the cluster expansions. An approach to limit phase space and methods to deal with multicomponent charge balance constrained open systems while including both weak, long-range electrostatic interactions and strong, short-range interactions in a single cluster expansion.

Thesis Supervisor: Gerbrand Ceder
Title: R. P. Simmons Professor of Materials Science and Engineering

Acknowledgments

First of all, I would like to thank my advisor Prof. Gerbrand Ceder for funding, research advice and all the other nice things. I also thank my thesis committee, Prof. Yang Shao-Horn and Prof. Yet-Ming Chiang for helping me improve this thesis, and to Dr. Robert Doe for proofreading the thesis document.

My computational work was greatly helped by cluster expansion and Monte Carlo code by Dr. Anton van der Ven and Dr. Tim Mueller. Dr. Ying Shirley Meng helped me with scientific discussion and improvement of my paper writing and survival skills. I also appreciate my past and present lab mates and other people at MIT who made my life here a great experience.

Finally, I would like to thank my daughter Sumika for being a nice kid while daddy was working on his thesis, and my wife Junko for supporting and encouraging me.

(We) can't reach (the goal) unless (we) mistake correctly…

Wait! If (we) correctly mistake, (we) can reach (the goal)!

-Risa Ito, from Oi Pi-tan! 8

Contents

Chapter 1 Introduction

Altering the properties of materials always requires a change in the local environment of the atoms within the material. For example, doping creates some atomic environments that include the dopant as neighbors, while annealing enables more frequent atomic diffusion that results in new, energetically favorable atomic environments at the annealing temperature. Quenching differs from slow cooling because atomic environments favored in high temperature are more likely to remain after cooling. These examples illustrate how many different local structures can be obtained during the experimental process, some being more energetically favorable than others.

It should be possible to make materials with ideal properties if the optimum atomic environments and corresponding processing conditions are known. The primary problem is that an understanding of the atomic environments cannot be easily obtained or measured except in the simplest systems; thus atomic scale engineering is not commonly utilized as a means of property improvement or control. Currently, a variety of experimental methods such as X-ray diffraction (XRD), nuclear magnetic resonance (NMR), transmission electron microscopy (TEM) and X-ray absorption fine structure spectroscopy (XAFS) are utilized to probe different length scales, yielding some idea of the environments. Computational methods such as first principles density functional theory (DFT) are being utilized to conduct total energy calculations with full structural

relaxation from an arbitrary initial configuration. However due to computational restrictions the unit cell size is limited, in turn limiting the description of long range order in a system.

Some systems with structural disorder may be very difficult to understand using experimental techniques. Lithium transition metal oxides such as $LiNi_{0.5}Mn_{0.5}O_2$ or $LiNi_{1/3}Co_{1/3}Mn_{1/3}O_2$ are one example: XRD or electron diffraction cannot distinguish the transition metals in these materials because they have a similar number of electrons. However, structural disorder can be precisely controlled in computation, where arbitrary unit cells can be used as input.

In this thesis, a computational "atomic engineering" approach is used to gain insight into the optimal material (phase) for a specific use of a system in consideration. Figure 1-1 shows a schematic flow chart of this approach. First, energies (E_{FP}) of various atomic configurations (σ) are obtained using first principles methods. Next, the cluster expansion formalism is used to fit the first principles energies to a simple polynomial of occupation variables on sites within a lattice model. It is also possible to understand the relevant interactions between atoms of the system in consideration from the cluster expansion. Afterward, Monte Carlo simulation is conducted to quickly sample energies of large unit cells using relatively accurate energies (E_{CE}) from the cluster expansion approximation. The goal of the Monte Carlo simulation is to compile a phase diagram in

temperature (T) - composition (x) space. Finally, physical intuition of the system is used to gain insight into processing conditions or composition ranges for possible property improvements. This method should allow us to overcome the unit cell size restriction in DFT while retaining a useful degree of accuracy.

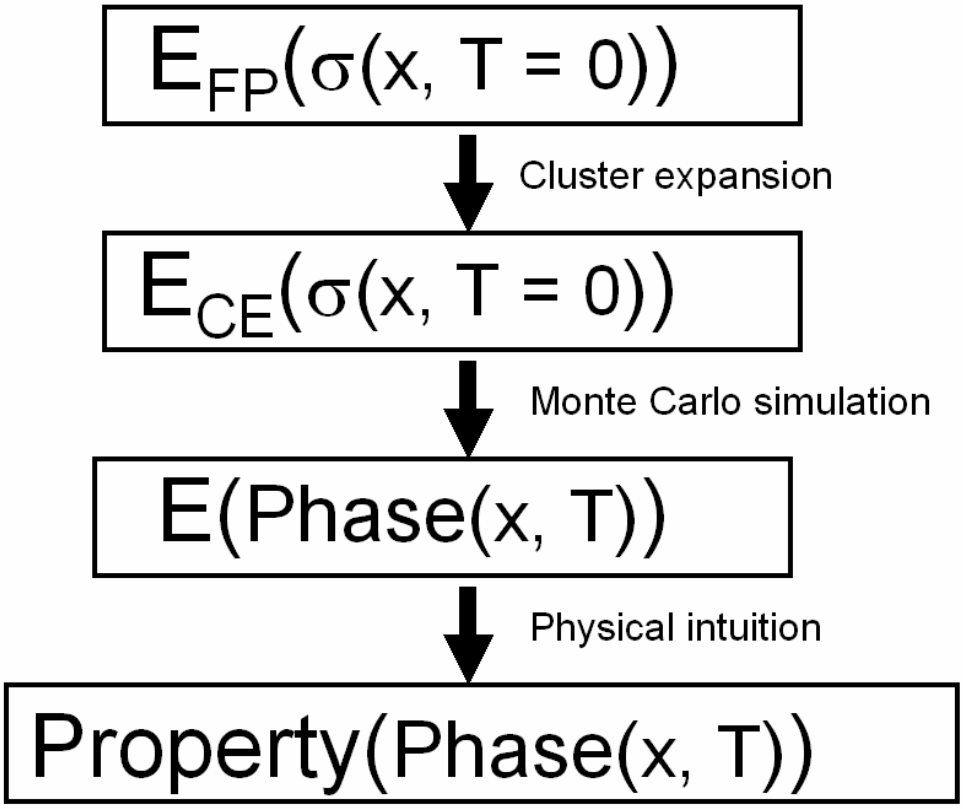

Figure 1-1. Schematic flow chart of properties optimization based on an atomic engineering approach.

This work is composed of explicit application of computational atomic engineering in two systems relevant from both engineering and science viewpoints: in the lithium ion battery cathode material, $LiNi_{0.5}Mn_{0.5}O_2$, and in the thermoelectric material,

Na_xCoO_2. This is also the first work to address cluster expansion in restricted phase space (penalized cluster expansion). Specifically, some atomic configurations were not allowed in each system studied because of too high energy results from the repulsion or overlap of atoms. This restriction was resolved by introducing a penalty to discourage sampling in restricted phase space during the Monte Carlo simulations.

The outline of this thesis is as follows: Chapter 2 covers the general methodology of phase diagram generation while the atomic engineering approach is applied to $LiNi_{0.5}Mn_{0.5}O_2$ and Na_xCoO_2 in Chapter 3 and Chapter 4 respectively. The methodological details specific to each system (semi-canonical binary-ternary coupled penalized cluster expansion for $LiNi_{0.5}Mn_{0.5}O_2$, and charge constrained grand canonical binary or binary-binary coupled penalized cluster expansion for Na_xCoO_2) are described in Chapters 3 and 4. The main objective of Chapters 3 and 4 is to understand the relevant physics and obtain a phase diagram showing the thermodynamically stable phases for each of these systems. Finally, Chapter 5 includes concluding remarks, and ideas regarding the direction of future work are presented in Chapter 6.

Chapter 2 Computational phase diagram generation

2.1 Overview

A temperature-composition (*T*-*x*) phase diagram is a key component in the atomic engineering approach because it is used to show what phases, or structures, are thermodynamically stable at a given temperature and composition. First principles calculations (Density Functional Theory: DFT) is a very powerful method of obtaining accurate ground state energies. However, one drawback previously mentioned is computing power limiting the size of the unit cell to roughly ~10^2 atoms, while another detriment is the inability of DFT to predict accurate energy at finite temperature. Cluster expansion (*1*) is one possible method of gaining insight into partially disordered states at finite temperatures. Its use has been demonstrated in alloy systems (*1-9*) as well as Li-vacancy ordering studies in lithium transition metal oxide systems (*10-13*). In general, the process of cluster expansion involves fitting DFT energies to a simple polynomial (cluster expansion) in order to quickly obtain energies of large cells on the order of ~10^5 atoms. Additionally, finite temperature behavior can be investigated by combining Monte Carlo simulations with cluster expansion.

It is necessary to conduct the following steps, summarized as a schematic flow chart in Figure 2-1, in order to generate a phase diagram:

1) First, parameterize the degrees of freedom and obtain the configurational information regarding the structures, then coarse grain out vibrational, electronic and magnetic information (*14*). The exception to this rule occurs when a single element must be configured with different valences (e.g. ordering of Co^{3+} and Co^{4+}) or different magnetic spin (e.g. ordering of Ni^{2+} with up-spin and down-spin). Although the element is the same, if this is an issue that cannot be neglected, then these have to be treated as different species.
2) Decide which structures (ordering patterns) will be considered in fitting the cluster expansion.
3) Obtain first principles energies for each of the structures. The lattice parameters and atomic coordinates will be relaxed in the first principles calculations.
4) Construct a cluster expansion.
5) Complete Monte Carlo simulations with the Metropolis algorithm.
6) If the cluster expansion does not seem to be a good model of the system, then iterate again from step 1.
7) Obtain phase transition temperatures from the simulated energy and/or heat capacity as a function of temperature. As described in detail later, this step may require free energy integration.
8) If grand canonical calculations are conducted, then stable phases for a given temperature may be obtained by observing discontinuities in composition as a function of chemical potential.

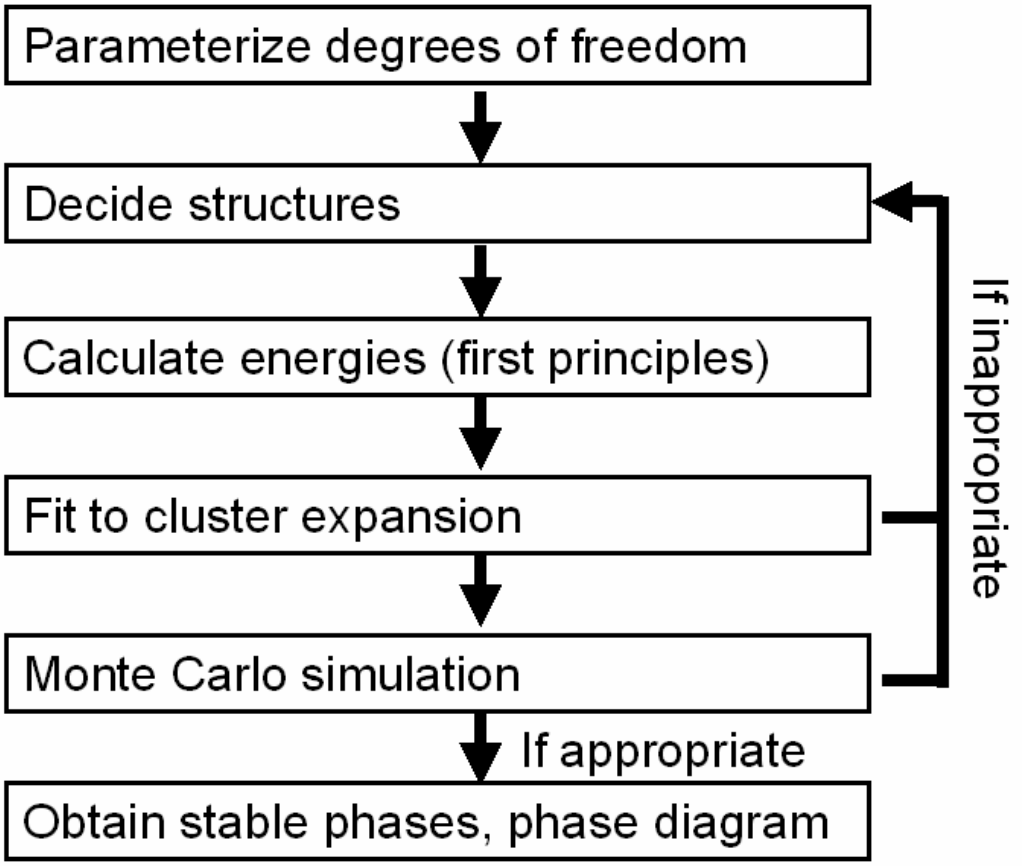

Figure 2-1. Schematic flow chart of phase diagram generation.

The key assumption is that configurational entropy causes the most significant energetic difference between various phases, while the contribution to free energy from other sources of entropy (e.g. vibrational, magnetic and electronic) is insignificant between phases and can be ignored (coarse grained out) (*14*). However, it should be noted that the fully relaxed energy for a given configuration is used as the energy for a configuration of species in ideal sites on the lattice model. It is possible to extend this formalism to incorporate other entropy sources. For instance, the formalism where vibrational entropy is also taken into consideration is shown in Garbulsky and Ceder (*15*).

Details of the cluster expansion construction, Monte Carlo simulation and free energy integration are discussed in the following section 2.2.

2.2 Cluster expansion

2.2.1 Formalism (*I*)

We consider a lattice model system with N sites where m species can occupy each site. There are m^N possible configurations ($\boldsymbol{\sigma}$), and we assume the energy ($E_{\boldsymbol{\sigma}}$) is known for each $\boldsymbol{\sigma}$. An m^N-dimensional vector ($\boldsymbol{\phi}(\boldsymbol{\sigma})$) is defined where the components are all possible combinations of one out of (1, σ_i, σ_i^2 … σ_i^{m-1}) multiplied over all i. Here, i is the label of a site, and σ_i is the occupation variable of site i. For example, if $N = 2$ and $m = 3$, i can be either 1 or 2, and one definition of $\boldsymbol{\phi}(\boldsymbol{\sigma})$ is

$$\boldsymbol{\phi}(\boldsymbol{\sigma}) = (1, \sigma_1, \sigma_2, \sigma_1^2, \sigma_1\sigma_2, \sigma_2^2, \sigma_1^2\sigma_2, \sigma_1\sigma_2^2, \sigma_1^2\sigma_2^2). \quad (2.1)$$

Occupation variables can take m different values depending on what species is occupying the site i (one example for values of the occupation variables are integers 0, 1, 2 … m–1). An m^N-dimensional vector ($\boldsymbol{V}$) exists such that $E_{\boldsymbol{\sigma}}$ is obtained by

$$E_{\boldsymbol{\sigma}} = \boldsymbol{V} \bullet \boldsymbol{\phi}(\boldsymbol{\sigma}). \quad (2.2)$$

Going back to the N = 2 and m = 3 example, if the occupation variables for site i are defined as σ_i = 0 if species A is occupying site i, 1 if species B is occupying and 2 if species C is occupying, three out of nine possible relations for $\boldsymbol{\phi}(\boldsymbol{\sigma})$ are the following:

$$\phi(\mathrm{AA}) = (1, 0, 0, 0, 0, 0, 0, 0, 0)$$

$$\phi(\mathrm{AB}) = (1, 0, 1, 0, 0, 1, 0, 0, 0)$$

$$\phi(\mathrm{BC}) = (1, 1, 2, 1, 2, 4, 2, 4, 4). \tag{2.3}$$

For

$$\boldsymbol{V} = (V_{00}, V_{10}, V_{01}, V_{20}, V_{11}, V_{02}, V_{21}, V_{12}, V_{22}) \tag{2.4}$$

examples of relations obtained by combining equation 2.2 with equations 2.3 and 2.4 are:

$$E_{\mathrm{AA}} = V_{00}$$

$$E_{\mathrm{AB}} = V_{00} + V_{01} + V_{02}$$

$$E_{\mathrm{BC}} = V_{00} + V_{10} + 2V_{01} + V_{20} + 2V_{11} + 4V_{02} + 2V_{21} + 4V_{12} + 4V_{22} \tag{2.5}$$

It is possible to uniquely calculate the explicit value of $\boldsymbol{V}$ by solving the full set of equations such as those in equation 2.5. It is important to note that values of $\boldsymbol{V}$ do not have any meaning unless the corresponding occupation variables are specified.

In the case of a *coupled* system with two sublattices, where there is an additional sublattice with N' sites and m' species, $m'^{N'}$ possible configurations (τ) exist. Defining j as the sites and τ_j as the occupation variables on the additional sublattice as, $\phi(\sigma,\tau)$ is defined as a $m^N m'^{N'}$-dimensional vector where the components are all possible combinations of products of $(1, \sigma_i, \sigma_i^2 \ldots \sigma_i^{m-1})$ over all i and $(1, \tau_j, \tau_j{}^2 \ldots \tau_j{}^{m'-1})$ over all i. $E_{\sigma\tau}$ is obtained by

$$E_{\sigma\tau} = \boldsymbol{V} \bullet \phi(\sigma,\tau). \tag{2.6}$$

It is possible to expand this formalism to systems with three or more sublattices in a similar way.

Now we attempt to simplify the cluster expansion using symmetry of the lattice. For simplicity, we can assume a system with one sublattice and $m = 2$, which is the case for a binary system. This enables equation 2.2 to be rearranged based on the total number of σ_i in each term:

$$E = V_0 + \sum_i V_i \sigma_i + \sum_{ij} V_{ij} \sigma_i \sigma_j + \sum_{ijk} V_{ijk} \sigma_i \sigma_j \sigma_k + \cdots \tag{2.7}$$

where i, j, k indicate different sites. As seen in the previous example, when $m > 2$, terms with squares and higher powers of σ_i will appear (equation 2.1) (*16*). Also note that in a coupled system some terms include products of both σ_i and τ_j (*17*). When sites are symmetrically equivalent, for example if the sites are on a simple hexagonal lattice, equation 2.7 can be greatly simplified. If all the sites are symmetrically equivalent, V_i no longer depends on the site i, thus the index can be dropped. The set of coefficients $\boldsymbol{V}$, named effective cluster interactions (ECI), may be regarded as a function of the relevant cluster, or configuration of sites. Similarly, the number of independent coefficients for pair clusters (clusters involving two sites) or triplet clusters (clusters with three sites) may be drastically reduced.

2.2.2 Cluster expansion approximation for energy prediction

The cluster expansion formalism in section 2.2.1 is exact, and in principle the cluster expansion (e.g. equation 2.7) has to be summed over all pairs, triplets, quadruplets, and larger clusters of sites. However, in practice the cluster expansion can be used to approximate the energy of a complicated system with very few coefficients. The ECI can be regarded as the effect of interactions in the cluster on the total energy. Therefore irrelevant clusters, such as those that include long-distance pairs, or contain too many sites, can be removed from the cluster expansion (ECI set to zero).

The main difficulty in making a good cluster expansion approximation is choosing which clusters to include in the cluster expansion and in choosing which structures to include when fitting (training) the cluster expansion. Relevant clusters are selected on the basis of how well they minimize the weighted cross-validation (CV) score. This is a means of describing how good the cluster expansion is at predicting the energy of a structure not included in the fit (*18*). A large number of structures close to the convex hull, or the line connecting the minimum energy possible in a given composition, should be calculated since it is crucial to obtain the correct ground states, and an accurate energy scale of the low energy excitations, to compile an accurate phase diagram. These low energy structures should also be weighed heavily when obtaining the CV score. Some structures with large excitation energies are also necessary to "pin" at high energy

structures in the cluster expansion so the local environments of high energy structures do not form in the Monte Carlo simulations. These high energy structures may be weighed lightly since it is not necessary to accurately predict the energy of these structures as compared to structures with lower energy.

It is crucial to have some insight into the physics of the system when determining the form of the cluster expansion. For example, if there are noticeably strong interactions, the ECI for clusters that represent such interactions should have larger magnitude. In general, larger clusters should have ECI of less magnitude than the ECI for smaller clusters, as well as a small ECI for clusters near the truncation cutoff. There are some cases, such as Na_xCoO_2 discussed in Chapter 4, where there are long-range electrostatic interactions that cannot be truncated to a short distance, necessitating a large number of pair clusters. To capture the physics of these systems, the energy from "background" ECIs representing the electrostatic interactions is removed prior to fitting the DFT energies to the cluster expansion, and then added back to the fitted cluster expansion.

When parts of the phase space are inaccessible or accurate energies are hard to obtain (e.g. if the simultaneous occupancy of nearest-neighbor pair is prohibited), it is possible to remove affected clusters thus removing any resulting linear dependencies in the fitting. Then, a penalty on the cluster expansion is added to increase the energy of the system in the restricted phase space. The penalized cluster expansion is applied to the

$LiNi_{0.5}Mn_{0.5}O_2$ system and Na_xCoO_2 system in Chapters 3 and 4 respectively, and there the actual forms of the cluster expansions are shown.

2.3 Monte Carlo simulation

Monte Carlo simulation is an efficient method to understand finite temperature behavior. The most common algorithm is the Metropolis algorithm (*19*) where perturbations to the system are accepted or denied according to the following criteria:

1) If $H_{old} \geq H_{new}$, then accept the perturbation

2) If $H_{old} < H_{new}$ and $\exp\left(-\frac{H_{new} - H_{old}}{kT}\right) < rand(0,1)$, then accept the perturbation

3) Else, deny the perturbation.

Here, H_{old} and H_{new} are the Hamiltonian values of the original (old) and perturbed (new) systems, k is a coefficient (Boltzmann constant), T is the temperature and *rand* (0,1) is a random number between 0 and 1 (0 and 1 exclusive) that is generated every time a perturbation is considered.

The perturbation is always accepted when it lowers the Hamiltonian (energy) and is sometimes accepted when the perturbation increases the energy; the likelihood exponentially decreasing with increase in energy. When implementing this method, it is crucial to not allow 0 as the random number to prevent *any* perturbation from being accepted.

If a grand canonical Monte Carlo simulation is being conducted, the Hamiltonian is the thermodynamic potential defined as

$$\Omega = E - \mu N . \tag{2.8}$$

Here, E is the energy, and μ is the chemical potential for the relevant composition N. Although a variety of perturbations are allowed to be used (e.g. simultaneously changing multiple occupation variables that conserve charge balance), the simplest perturbation is changing the occupation variable of one site. Such grand canonical simulation is the preferred method when composition is allowed to change because no two-phase regions appear in a temperature-chemical potential (T-μ) phase diagram. Two-phase regions do appear in the T-x phase diagram because discontinuity of composition is allowed at first-order phase transition boundaries.

Monte Carlo simulations are typically conducted with either fixed temperature or fixed chemical potential to scan T-μ phase space. The correlation length and correlation time of the system diverges close to phase transitions (*20*). Finite size effects are observed near transitions because the correlation length is limited to the Monte Carlo cell dimensions. For example, the magnitude of peaks in the thermodynamic potential fluctuation (e.g. heat capacity) changes with system size. First order transitions, such as some order-disorder transitions, are detected when E or the slope of Ω is discontinuous. The heat capacity cannot be defined at the transition point, however a peak is often observed. Second-order transitions, such as some order-order transitions, have continuous

E at the transition point and are characterized by the peak in the fluctuation that changes with the system size.

Free energy integration is needed when the phase transition temperature cannot be simply be obtained from the energy and/or heat capacity calculated during Monte Carlo simulations. One example occurs when there is a significant hysterisis between grand canonical heating and cooling runs at the same chemical potential, as seen in the next section.

2.4 Free energy integration

In thermodynamics, the free energy of a system with one compositional degree of freedom $F(T, N)$ is defined as

$$F = -kT \ln Q \tag{2.9}$$

where k is the Boltzmann constant. The partition function

$$Q = \sum_{\sigma} \exp(-\beta E_{\sigma}) \tag{2.10}$$

is summed over all configurations (σ). Here, β is equal to $(kT)^{-1}$.

The Legendre transformation is used to obtain the free energy

$$\Phi(T, \mu) = F - \mu N \tag{2.11}$$

for Ω. Φ is given by:

$$\Phi = -kT \ln Z \tag{2.12}$$

using the (grand canonical) partition function:

$$Z(\beta,\mu) = \sum_{\sigma} \exp\left(-\beta\left(E_{\sigma} - \mu N_{\sigma}\right)\right) = \sum_{\sigma} \exp\left(-\beta\Omega_{\sigma}\right). \tag{2.13}$$

Free energy integration can be conducted when the free energy (Φ_0) is known for a given temperature (T_0) and chemical potential (μ_0). The free energy F (Φ) is equivalent to the energy E (Ω) when there are no excitations (T = 0 or entropy S = 0), and these points are useful as primary reference points. The following integration methods can be used to obtain the free energy for other points:

1) Along a fixed temperature trajectory,

$$\left(\frac{\partial\Phi}{\partial\mu}\right)_T = -kT\left(\frac{\partial \ln Z}{\partial\mu}\right)_T = -kT\frac{\sum_{\sigma}\beta N_{\sigma}\exp\left(-\beta\left(E_{\sigma}-\mu N_{\sigma}\right)\right)}{\sum_{\sigma}\exp\left(-\beta\left(E_{\sigma}-\mu N_{\sigma}\right)\right)} = -\langle N\rangle \tag{2.14}$$

where $\langle N\rangle$ is the grand canonical thermodynamical average of N.

Integrating equation 2.14 leads to:

$$\Phi(T_0,\mu) = \Phi(T_0,\mu_0) - \int_{\mu_0}^{\mu}\langle N(T_0,\mu)\rangle d\mu\,. \tag{2.15}$$

2) Along a fixed chemical potential trajectory,

$$\left(\frac{\partial(\Phi\beta)}{\partial\beta}\right)_{\mu} = -\left(\frac{\partial \ln Z}{\partial\beta}\right)_{\mu} = \frac{\sum_{\sigma}\Phi_{\sigma}\exp\left(-\beta\Omega_{\sigma}\right)}{\sum_{\sigma}\exp\left(-\beta\Omega_{\sigma}\right)} = \langle\Omega\rangle \tag{2.16}$$

Integrating equation 2.16 yields:

$$\frac{\Phi(T,\mu_0)}{kT} = \frac{\Phi(T_0,\mu_0)}{kT_0} + \int_{T_0}^{T} \langle \Omega(T,\mu_0) \rangle d\beta . \tag{2.17}$$

These integrations are typically conducted numerically by trapezoidal summation, represented as:

$$\int_{x_0}^{x_k} f(x)dx = \sum_{i=1}^{k} \frac{f(x_i) + f(x_{i-1})}{2} \cdot (x_i - x_{i-1}). \tag{2.18}$$

Figure 2-2 depicts two representative phase diagrams with the free energy integration trajectories shown as bold lines in the T-μ phase diagram in Figure 2-2a. The phase transition point is where F (for canonical calculations) or Φ (for grand canonical calculations) of the low temperature phase and high temperature phase equal. For the low temperature phase, method 2 is used to obtain Φ by integrating Ω of a fixed chemical potential heating simulation from a low enough temperature (equation 2.17). For the high temperature phase, method 1 is used to obtain a reference free energy at T_{high} with a fixed temperature calculation (equation 2.15). Afterward, method 2 can be utilized to integrate Ω of a fixed chemical potential cooling simulation (equation 2.17). Figure 2-2b shows the trajectories in T-x space, and how the discontinuity in concentration at the phase transition point leads to a two-phase region.

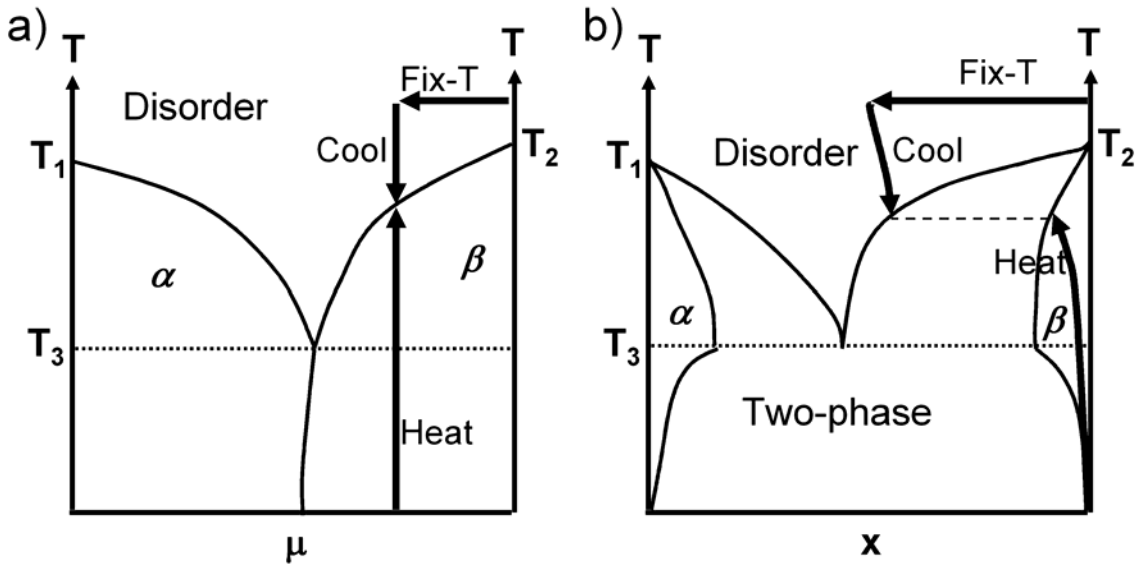

Figure 2-2. Schematic phase diagram in (a) temperature-chemical potential space and (b) temperature-composition space. Free energy integration trajectories are shown with arrows.

Figure 2-3 shows an actual simulation result demonstrating phase transition temperature determination from free energy integration in Na_xCoO_2. The grand canonical energy (Ω) as a function of temperature obtained from Monte Carlo simulation are shown in Figure 2-3a. The phase transition temperature is between 430K (transition observed from cooling simulation) and 480K (transition observed from heating simulation), but cannot be obtained with higher precision unless there is other information. In contrast, the phase temperature is determined accurately as 450K from the free energy (Φ) as a function of temperature in Figure 2-3b because the free energies of cooling and heating simulations intersect at this point.

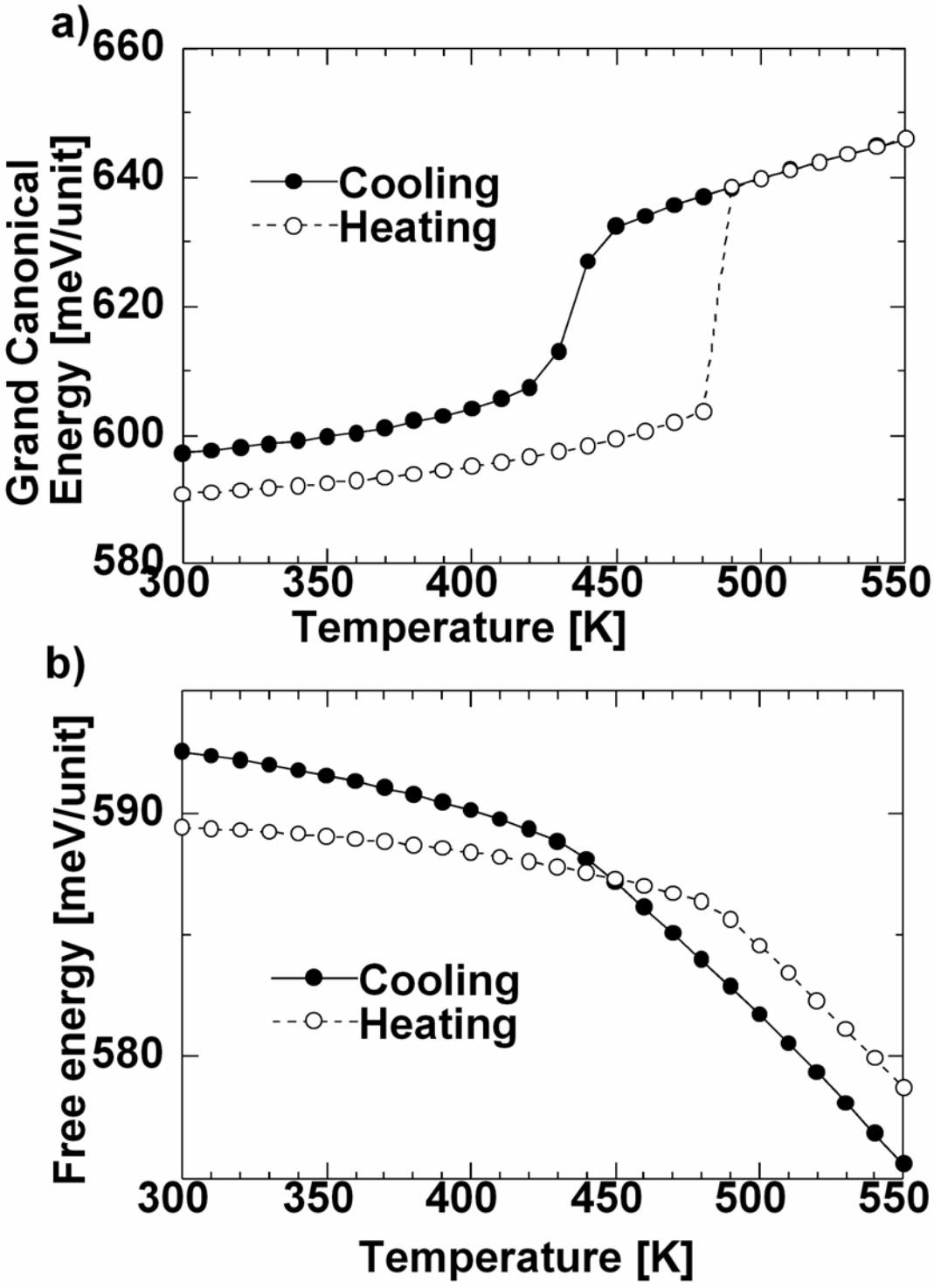

Figure 2-3. Demonstration of phase transition temperature from free energy integration. (a) Grand canonical energy (Ω) from Monte Carlo simulation. (b) Free energy (Φ) obtained from the energies in (a).

2.5 References

1. J. M. Sanchez, F. Ducastelle, D. Gratias, *Physica A: Statistical and Theoretical Physics* **128**, 334 (1984).
2. D. de Fontaine, in *Solid State Physics - Advances in Research and Applications*. (1994), vol. 47, pp. 33-176.
3. G. Ceder, A. Van der Ven, C. Marianetti, D. Morgan, *Modelling and Simulation in Materials Science and Engineering* **8**, 311 (May, 2000).
4. M. Asta, S. M. Foiles, A. A. Quong, *Physical Review B* **57**, 11265 (May 1, 1998).
5. C. Wolverton, *Philosophical Magazine Letters* **79**, 683 (Sep, 1999).
6. V. Ozolins, B. Sadigh, M. Asta, *Journal of Physics-Condensed Matter* **17**, 2197 (Apr 6, 2005).
7. M. Asta, V. Ozolins, C. Woodward, *Jom-Journal of the Minerals Metals & Materials Society* **53**, 16 (Sep, 2001).
8. C. Wolverton, D. Defontaine, *Physical Review B* **49**, 8627 (Apr 1, 1994).
9. M. Asta, C. Wolverton, D. Defontaine, H. Dreysse, *Physical Review B* **44**, 4907 (Sep 1, 1991).
10. A. Van der Ven, M. K. Aydinol, G. Ceder, G. Kresse, J. Hafner, *Physical Review B* **58**, 2975 (1998).
11. C. Wolverton, A. Zunger, *Physical Review Letters* **81**, 606 (Jul 20, 1998).
12. C. Wolverton, A. Zunger, *Journal of the Electrochemical Society* **145**, 2424 (Jul, 1998).
13. M. de Dompablo, A. Van der Ven, G. Ceder, *Physical Review B* **66**, 64112 (Aug 1, 2002).
14. G. Ceder, *Computational Materials Science* **1**, 144 (1993).
15. G. D. Garbulsky, G. Ceder, *Physical Review B* **53**, 8993 (Apr 1, 1996).
16. G. Ceder, G. D. Garbulsky, D. Avis, K. Fukuda, *Physical Review B* **49**, 1 (Jan 1, 1994).
17. P. D. Tepesch, G. D. Garbulsky, G. Ceder, *Physical Review Letters* **74**, 2272 (Mar 20, 1995).
18. A. van de Walle, G. Ceder, *Journal of Phase Equilibria* **23**, 348 (Aug, 2002).
19. N. Metropolis, A. W. Rosenbluth, M. N. Rosenbluth, A. H. Teller, E.Teller, *Journal of Chemical Physics* **21**, 1987 (1953).
20. N. E. J. Newman, G. T. Barkema, *Monte Carlo Methods in Statistical Physics* (Clarendon Press, Oxford, 1999), pp. 83-85.

Chapter 3 The lithium battery material $Li_xNi_{0.5}Mn_{0.5}O_2$

3.1 Introduction to lithium ion batteries

Batteries are charge storage devices in which electrical energy can be extracted from a chemical reaction known as discharging. In the case of a secondary, or rechargeable, battery the reaction chemistry is reversible and the charge can also be restored (charged). When a battery is charged or discharged electrons move from one electrode to the other through an external circuit in order to store or release energy. The two electrodes, referred to as the cathode and anode, are electronically separated by a separator (e.g. polypropylene sheets) in the battery. Electron transfer through the external circuit of the cell is compensated by ionic transfer through the electrolyte between the electrodes.

Figure 3-1 shows the dependency of energy density on the various battery chemistries. Among these, lithium ion (Li-ion) batteries exhibit the highest theoretical energy density (I). For this reason, Li-ion batteries are an attractive choice for applications where space and weight constraints are stringent, such as in portable electronics and space applications. In Li-ion batteries, this charge transfer is done by Li^+ diffusion. The first commercialized rechargeable Li-ion battery was released by Sony in June 1991. The cell chemistry consisted of graphite anode combined with a high

temperature phase of lithium cobalt oxide (HT-$LiCoO_2$, or simply $LiCoO_2$) as the cathode (*2*).

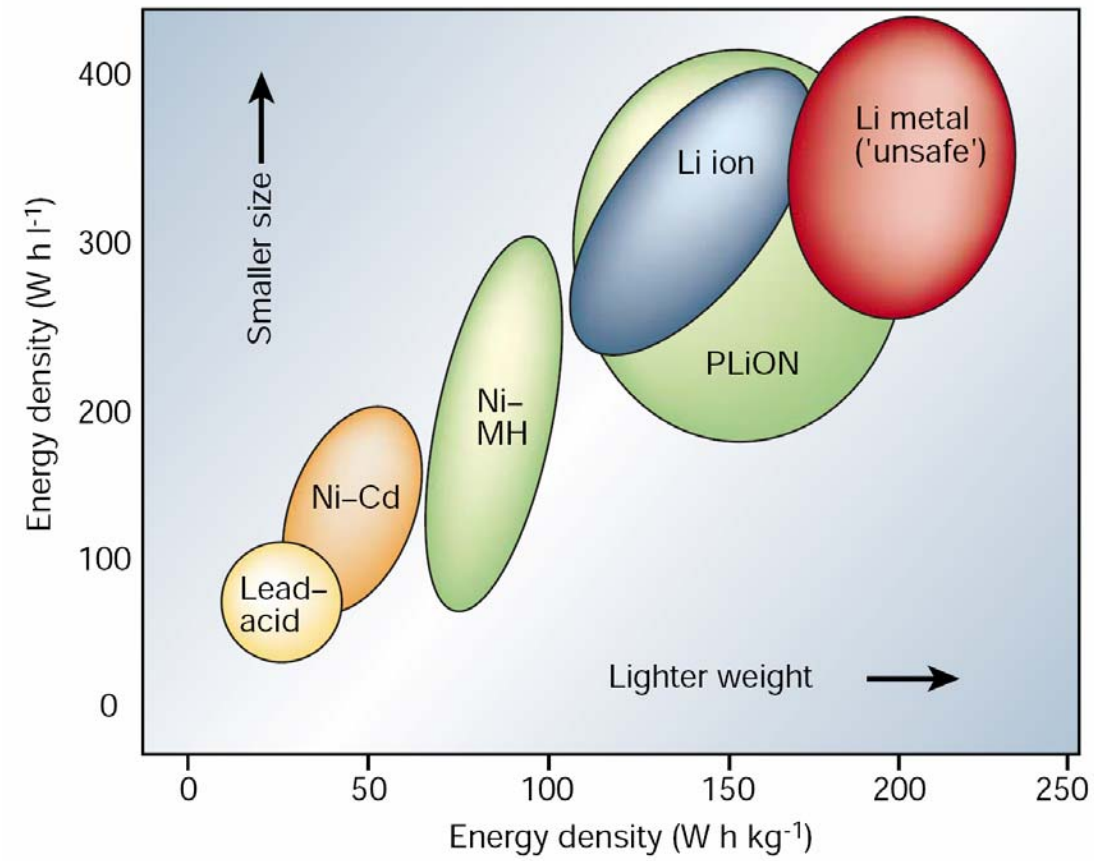

Figure 3-1. Comparison of the different battery technologies in terms of volumetric and gravimetric energy density (*1*).

HT-$LiCoO_2$ has a layered O3 structure (*3*) as shown in Figure 3-2. If all the cations consist of the same element, then this is equivalent to the rocksalt structure. However, $LiCoO_2$ consists of alternating Li and transition metal layers that form along the hexagonal axis. In a perfect crystal there is no disorder, in turn yielding the R-3m space group.

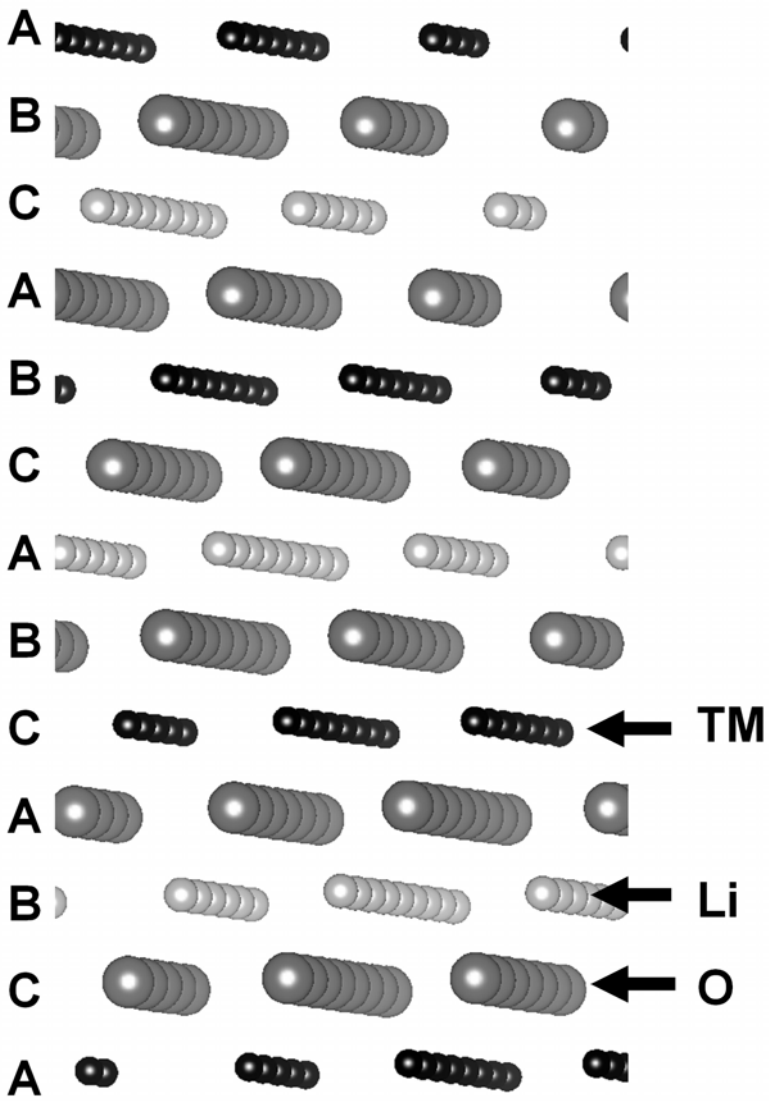

Figure 3-2. Lithium transition metal oxide ($LiTMO_2$) in the O3 structure. In $LiCoO_2$, all transition metals are Co.

The most important feature of the O3 lithium transition metal oxide family is that the Li layer acts as a two-dimensional Li^+ diffusion channel, allowing Li^+ to be

inserted and removed with relative ease. The activation barrier to Li^+ diffusion within this channel is reported to be about 200meV, or about $8k_BT$ at room temperature from first principles calculations (*4*).

One major drawback of $LiCoO_2$ is that the usable capacity is ~150mAh/g, roughly half of its theoretical capacity. This is because discharge above this threshold, or overdelithiation, causes a sudden decrease in the *c* lattice parameter (*5, 6*) due to a phase transition from the O3 phase to the H1-3 phase (*6, 7*). Upon further discharge, there is another phase transition to the O1 phase (*6, 7*). There are also safety issues with $LiCoO_2$, since $Li_{0.4}CoO_2$ has been shown to release oxygen upon heating to ~200^oC (*8*). This oxygen can combust the organic electrolyte and lead to a rapid battery fire.

During the search for next-generation Li-ion battery cathode materials, Co was replaced by other transition metals including Ni or Mn. When compared with $LiCoO_2$, $LiNiO_2$ shows less thermal stability as a cathode material (*8*). The thermodynamically stable phase of $LiMnO_2$ is not the O3 rocksalt structure, and Li^+ removal causes irreversible structural transformation, forming a less electrochemically active phase (*9*). To circumvent problems like these, a combination of transition metals has been used to substitute Co. Two promising materials that have exhibited significantly better stability are $LiNi_{1/3}Co_{1/3}Mn_{1/3}O_2$ and $LiNi_{0.5}Mn_{0.5}O_2$. $LiNi_{1/3}Co_{1/3}Mn_{1/3}O_2$ has capacity of 150mAh/g in the 3.5V-4.2V range, which increases to 200mAh/g by charging to 5.0V

versus Li^+/Li (*10*). $LiNi_{0.5}Mn_{0.5}O_2$ also has higher reversible capacity of about 200mAh/g by charging to 4.5V (*11-14*).

3.2 Characteristics of $LiNi_{0.5}Mn_{0.5}O_2$

$LiNi_{0.5}Mn_{0.5}O_2$ (*11-16*) is an interesting material for both its engineering and scientific aspects. As mentioned in the previous section, the theoretical capacity of $LiNi_{0.5}Mn_{0.5}O_2$ is about 280 mAh/g, of which 200 mAh/g can now routinely be achieved at low rates such as C/20 (*11-14, 16*). Moreover, since $LiNi_{0.5}Mn_{0.5}O_2$ does not contain the rather expensive cobalt, a reduction of cost for Li batteries may be realized with this material. Other properties of the material, such as thermal stability and safety, have also been demonstrated to be better than $LiCoO_2$ (*11, 13*).

Though the rate capability of the material has generally been shown to be poor, recent efforts indicate that it may be possible to overcome this issue by structural modifications (*16*), keeping this an attractive electrode material. Much of the desirable properties are derived from the synergetic combination of Mn^{4+} and Ni^{2+}. Mn^{4+} is one of the most stable octahedral ions, maintaining the structural integrity when Li is extracted, while Ni^{2+} can be fully oxidized to Ni^{4+}, thereby compensating for the fact that Mn^{4+} cannot be oxidized further (*17-19*).

On average, the cation positions of $LiNi_{0.5}Mn_{0.5}O_2$ are characterized as the O3-type layered structure (*20*) similar to $LiCoO_2$, however elucidating the details of the cation ordering has been difficult (*12, 21-27*). In addition, there is a significant correlation between structure and electrochemical performance, which becomes clear when comparing different synthesis conditions. For instance a small amount of Ni in the Li layers is always observed in materials synthesized at temperatures around 900~1000^{o}C with conventional solid state processes. In general, there is about 8~11% of this type of Li/Ni disorder (*11, 13, 21, 23, 24, 28-32*). Some literature suggests that Li/Ni disorder will *increase* slightly as annealing temperature is *decreased* (*13, 28*).

Li/Ni disorder has negative effects on deintercalation of Li^+ (*16*) because Ni atoms positioned in the Li layer reduce the region of space in which Li^+ diffuses, resulting in an increased Li^+ diffusion activation barrier and reduced rate capability (*16*). As a result, there is an incentive to find methods to move these Ni into the TM layer and to investigate whether Ni is mobile during delithiation. Earlier XAFS results from a study by Arachi et al (*21*) suggest migration of Ni into tetrahedral sites, though the details of the mechanism are not known. Van der Ven and Ceder (*25*) succeeded in developing a reasonable first principles model of the delithiation voltage, however, in their model, a perfect "flower" ordering was assumed for transition metals, and no transition metal movement was allowed during delithiation (*25*).

The valence states of Ni and Mn are observed to be +2 and +4 respectively in both first principles computation (*32*) and X-ray absorption spectroscopy (*33, 34*). Thus, electrostatic interactions are likely to have a strong effect on the ordering of Ni and Mn in the Transition Metal-rich layer (TM layer). Four different structural models of the TM layer in $LiNi_{0.5}Mn_{0.5}O_2$ have been proposed by various theoretical and experimental investigations: 1) The *zigzag* structure (*30*) in which Mn and Ni are ordered in zigzag lines without any significant amount of Li present in the TM layer (Figure 3-3a); 2) the *flower* structure with a $2\sqrt{3} \times 2\sqrt{3}$ unit cell, which consists of concentric hexagons of Mn and Ni around a central Li (Figure 3-3b) (*25*); 3) the partially disordered *honeycomb* structure with $\sqrt{3} \times \sqrt{3}$ unit cell (*23*) in which the symmetry is broken between a Mn-rich and a Li-rich sublattice (Figure 3-3c) (*35*); and 4) a disordered model without any particular ordering between Mn and Ni (*28*). The honeycomb model seems to agree best with the available experimental evidence. Experiment suggests that two types of sites, denoted α and β, compose the TM layer (*23*). The α sites are generally occupied by either Li or Ni, while the β sites are preferred by Ni or Mn. The α sites are always the nearest neighbors to a β site. The flower structure is commensurate with the honeycomb model, but it displays a higher degree of long-range order, and can be considered a special case of the honeycomb model. Understanding cationic arrangement in this material is important as the electrochemical lithiation/delithiation process and the subsequent structural stability depends on the initial structure as suggested from Nuclear Magnetic Resonance (NMR) and first principles studies (*25, 31*).

This chapter first shows how Li/Ni disorder limits technologically important factors such as rate capability and capacity. Second, computational evidence of a complex thermal disordering process is presented to show how the system undergoes a phase transition from a low temperature zigzag-like state with no Li/Ni exchange to a partially disordered flower structure with increased temperature. The initial phase change is followed by further disordering which creates a honeycomb superstructure at higher temperature.

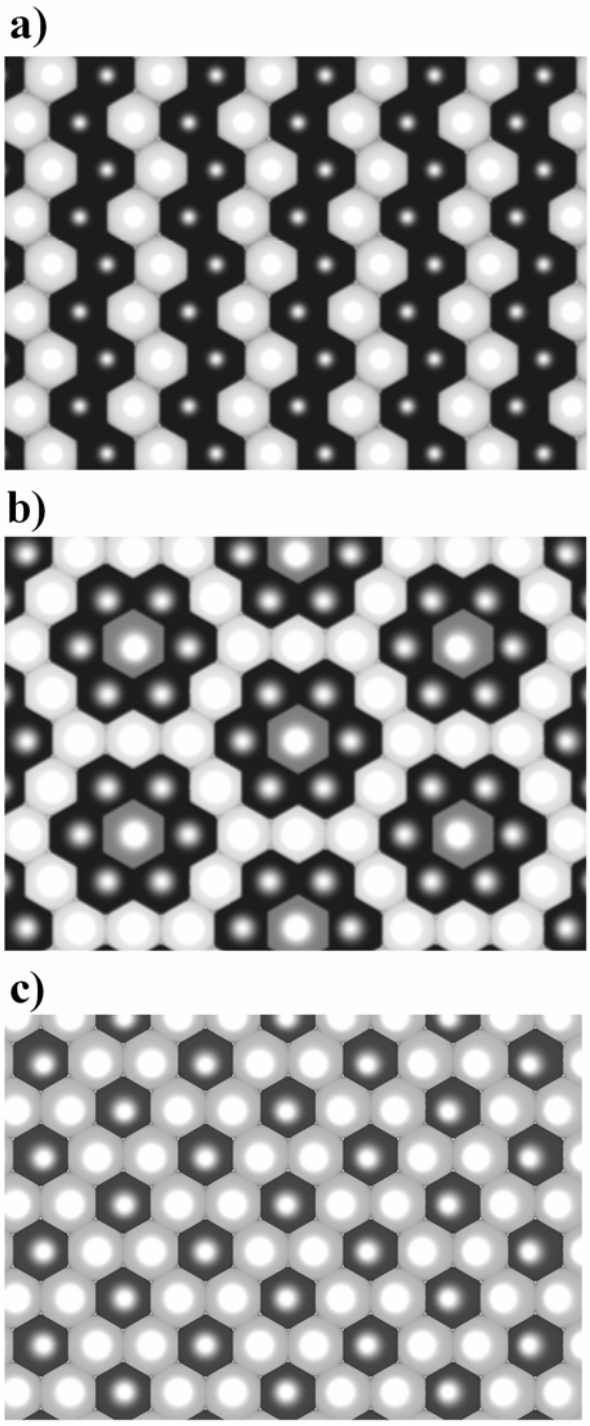

Figure 3-3 (a) Transition Metal layer (TM layer) ordering of the zigzag structure. There is no Li in the TM layer. (b) TM layer ordering of the flower structure. There is 8.3% Li/Ni disorder, or 8.3% Li in the TM layer. Legend: black: Mn, white: Ni, gray: Li. (c) TM layer ordering of the honeycomb pattern. Legend: dark gray: α sites that can be occupied by Li or Ni, light gray: β sites that can be occupied by Ni or Mn.

3.3 Methodology

Calculations were performed on various ordered arrangements (*7, 25, 36-38*) utilizing the Generalized Gradient Approximation and Hubbard U correction within Density Functional Theory (GGA+U). Core electron states were represented by the Projector Augmented-Wave method (*39*) as implemented in the Vienna Ab Initio Simulation Package (VASP) (*40*). The Purdew-Burke-Ernzenhof (PBE) exchange correlation (*41*) and a plane wave representation for the wavefunction with a cutoff of 370 eV were used. The Brillouin zone was sampled with a mesh including the gamma point. A 3 x 3 x 3 mesh was used for the flower configuration unit cell with 48 atoms, and for cells with different sizes a mesh with similar density was used. The charge density was spin polarized, with Mn spins aligned ferromagnetically with other Mn, and antiferromagnetically with Ni in the transition metal layer. The moment of Ni in the Li layer was aligned ferromagnetically with Mn. These spin configurations are similar to those suggested in the flower structure (*25*). The Hubbard U values applied to the Hamiltonian were needed to correct for the self-interaction error that occurs with transition metals with DFT (*42, 43*). These values have been calculated elsewhere to be 5eV per Mn atom and 5.96eV per Ni atom (*42*).

A binary-ternary coupled cluster expansion (*44*) was used to model partially disordered states at finite temperatures. Li and Ni were allowed to occupy sites in the Li

layer creating binary disorder, whereas ternary disorder was modeled by allowing Li, Ni and Mn to occupy sites in the TM layer. The site variables are designated as $\tau = 0$ for Li and $\tau = 1$ for Ni in the Li layer, and $\sigma = -1$ for Mn, $\sigma = 0$ for Ni, and $\sigma = 1$ for Li in the TM layer. The Hamiltonian becomes:

$$E_v^{predict} = C + \sum_i V_0 \tau_i + \sum_{i,j} V^{Li}(i,j)\, \tau_i \tau_j + \sum_{i,j,k} \sum_{s=1}^{2} V_s^{\text{int}}(i,j)\, \sigma_i^s \tau_j + \sum_{i,j,k} \sum_{s=1}^{2} \sum_{t=1}^{2} V_{st}^{TM}(i,j)\, \sigma_i^s \sigma_j^t + \sum_{i,j,k} V^{Li}(i,j,k)\, \tau_i \tau_j \tau_k + \sum_{i,j,k} \sum_{s=1}^{2} V_s^{\text{int}\,1}(i,j,k)\, \sigma_i^s \tau_j \tau_k + \sum_{i,j,k} \sum_{s=1}^{2} \sum_{t=1}^{2} V_{st}^{\text{int}\,2}(i,j,k)\, \sigma_i^s \sigma_j^t \tau_k + \sum_{i,j,k} \sum_{s=1}^{2} \sum_{t=1}^{2} \sum_{u=1}^{2} V_{stu}^{TM}(i,j,k)\, \sigma_i^s \sigma_j^t \sigma_k^u + \cdots \quad (3.1)$$

Here, V are the Effective Cluster Interactions (ECI), and V_0 specifically acts as a site energy of the Li layer sites. The ECI V^{Li}, V^{int} and V^{TM} represent respectively Li layer clusters, clusters that contain both Li and TM layer sites, and TM layer clusters respectively. The indices i, j, and k are labels of sites in the cluster. The dummy indices s, t, and u are used to distinguish different ECI on the same cluster and are either 1 or 2. The cluster expansion was fitted to the energies of 183 different configurations of Li, Ni and Mn.

Canonical Monte Carlo simulations were conducted with this cluster expansion in cells of 2592 formula units (2592 Li layer sites, 2592 TM layer sites). In general, 50,000 equilibrium passes and 100,000 sampling passes were used at every temperature between 200K and 1500K. In the range near the phase transitions (700-990K), 100,000

equilibrium passes were used to allow better equilibration. Note that one sampling pass amounts to one possible perturbation of each site on the lattice.

3.4 Results

3.4.1 Comparison of GGA and GGA+U

The energy of the flower (*25*) and zigzag (*30*) structures were calculated with both the GGA and GGA+U approximations to investigate the energy difference between structures with and without Li/Ni disorder. These structures are representative of the limiting states with (flower) and without (zigzag) Li/Ni disorder. Table 3-1 shows the energy differences between the two structures. Note that the energy difference in the two structures is an order of magnitude smaller in GGA than in GGA+U. This is consistent with prior work suggesting that the flower and zigzag structures are almost degenerate in the GGA approximation (*25*). Though further discussion will follow, all energies used for the cluster expansion fit were calculated with the GGA+U approximation because this method is believed to be a more accurate description of the system.

Table 3-1. Difference in energy in meV/FU between GGA and GGA+U approximations for flower and zigzag structures.

	GGA (ΔE)	GGA+U (ΔE)
Flower	**0 (Ground state)**	**26**
Zigzag	**2**	**0 (Ground state)**

3.4.2 Delithiation behavior of $Li_xNi_{0.5}Mn_{0.5}O_2$

First principles energy calculations were conducted on $Li_xNi_{0.5}Mn_{0.5}O_2$ for structures with TM layer cations in the flower ordering and zigzag ordering in an effort to understand the difference in delithiation behavior. The energies pertaining to the two scenarios of the flower ordering with 8.3% Li/Ni exchange were calculated, one where diffusion of the Ni in the Li layer to the TM layer was allowed, and another where it was not allowed.

Figure 3-4 shows the convex hull resulting from formation energies of partially delithiated $Li_xNi_{0.5}Mn_{0.5}O_2$. Formation energies are the energy difference between the mixed state and a compositionally averaged combination of lowest energy states of $Li_1Ni_{0.5}Mn_{0.5}O_2$ and $Ni_{0.5}Mn_{0.5}O_2$. Delithiation of the flower structure causes the Li^+ in the TM layer, and one Li^+ in the Li layer, to move into the tetrahedral sites adjacent to the

octahedral site that was previously occupied by Li^+ in the TM layer. This forms a dumbbell-like pattern that vacates all Li in octahedral sites adjacent to the two tetrahedral Li^+. These pairs of Li^+ in the tetrahedral sites are the last Li to be removed during delithiation (*25, 45*). Ni in the Li layer will not diffuse to the TM layer until the end of delithiation, which is also when tetrahedral Li is removed, even when the diffusion of Ni in the Li layer of flower ordering is allowed. Our findings indicate that TM cation migration is never energetically favorable during delithiation of zigzag ordered $Li_xNi_{0.5}Mn_{0.5}O_2$.

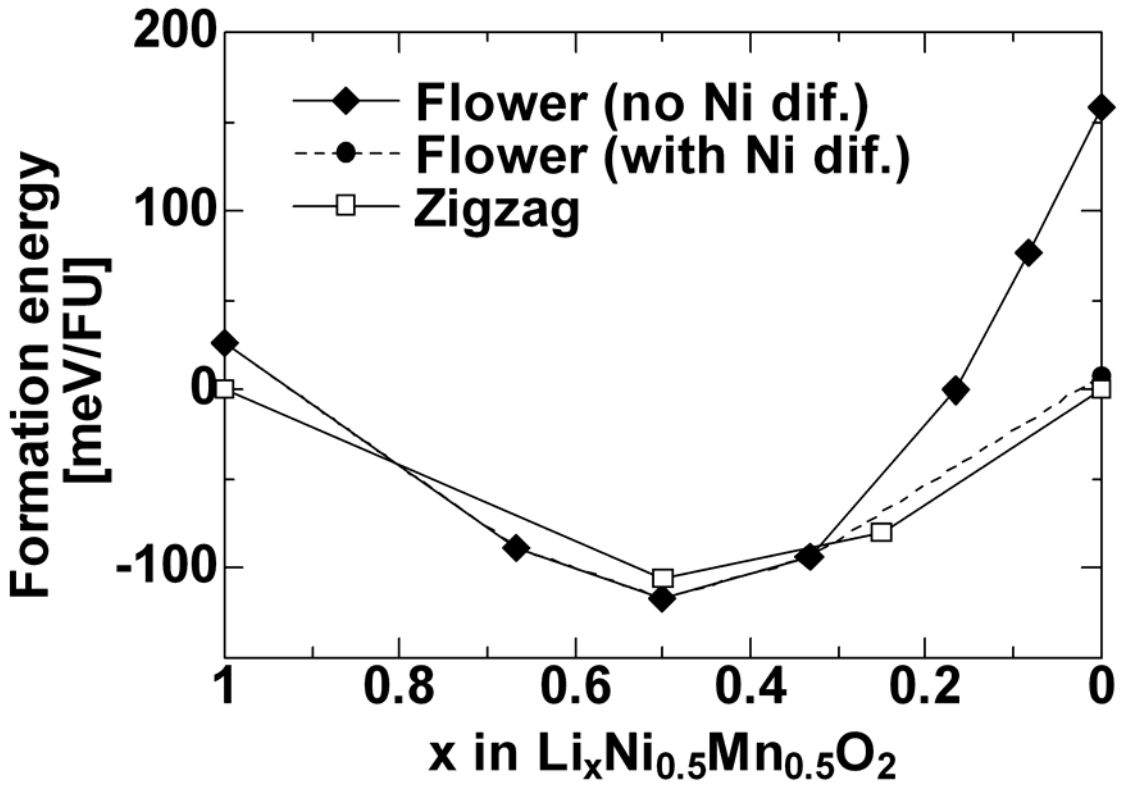

Figure 3-4. Formation energies from first principles calculations of partially delithiated $Li_xNi_{0.5}Mn_{0.5}O_2$. When cations in the TM layer was arranged in the flower ordering, energies were calculated in the two scenarios where diffusion of the Ni in the Li layer to the TM layer upon delithiation was allowed (with Ni diffusion) or not allowed (no Ni diffusion). One FU contains one transition metal atom.

Initial ordering and different scenarios of Ni migration have dramatic effects on the Li deintercalation potential, because the potential is the derivative of the total energy with respect to concentration at zero Kelvin. Figure 3-5 is a plot of the voltage from one concentration to the next upon Li deintercalation of the three different structural

evolution scenarios discussed in Figure 3-4. The voltage is calculated as the average in small concentration intervals. Most steps are artificial because the average voltage switches from one concentration to the next. This simple plot gives insight into the evolution of the voltage as a function of composition under different structural assumptions and does not require a complete chemical potential computation, though a more defined voltage profile can be obtained by computing many Li-vacancy configurations and using the cluster expansion and Monte Carlo simulation technique. The experimentally observed potential between $x = 1$ and $x \sim 0.67$ for the flower structure corresponds to the simultaneous removal of Li from the TM layer and the Li layer, and the formation of tetrahedrally coordinated Li as discussed previously (*25, 45*). There is only one significant voltage difference between the two structural models occurring near the end of charge at $x < 0.33$. If the last 16.7% of Li is to be removed from the tetrahedral sites without any other configurational changes, then a potential as high as 5.2V is required. In contrast, a significantly lower charge voltage is required if the oxidized Ni ions can migrate from the Li layer into the TM layer. The potential predicted for this reaction is 4.5V, remarkably close to the rest potentials in the open circuit voltage for cells charged up to 5.2V (*26*). These calculations suggest that at the end of charge Li removal is possible through two different processes: a fast process at very high potential that involves direct extraction of Li from tetrahedral sites, and a lower voltage process that can only occur when the structure can relax through the migration of Ni ions. The latter process does allow for removal of all Li from the material in "normal" voltage

windows, which seems to be in agreement with the fact that the capacity in the first charge of most experiments approaches the theoretical limit. In stark contrast, examination of the delithiation pathway of the zigzag structures shows that it is possible for all Li atoms to migrate out in "normal" voltage windows with no required diffusion of Ni into the Li layer. In conclusion, Li/Ni disorder is shown to limit capacity in battery applications through formation of tetrahedral Li that are difficult to extract.

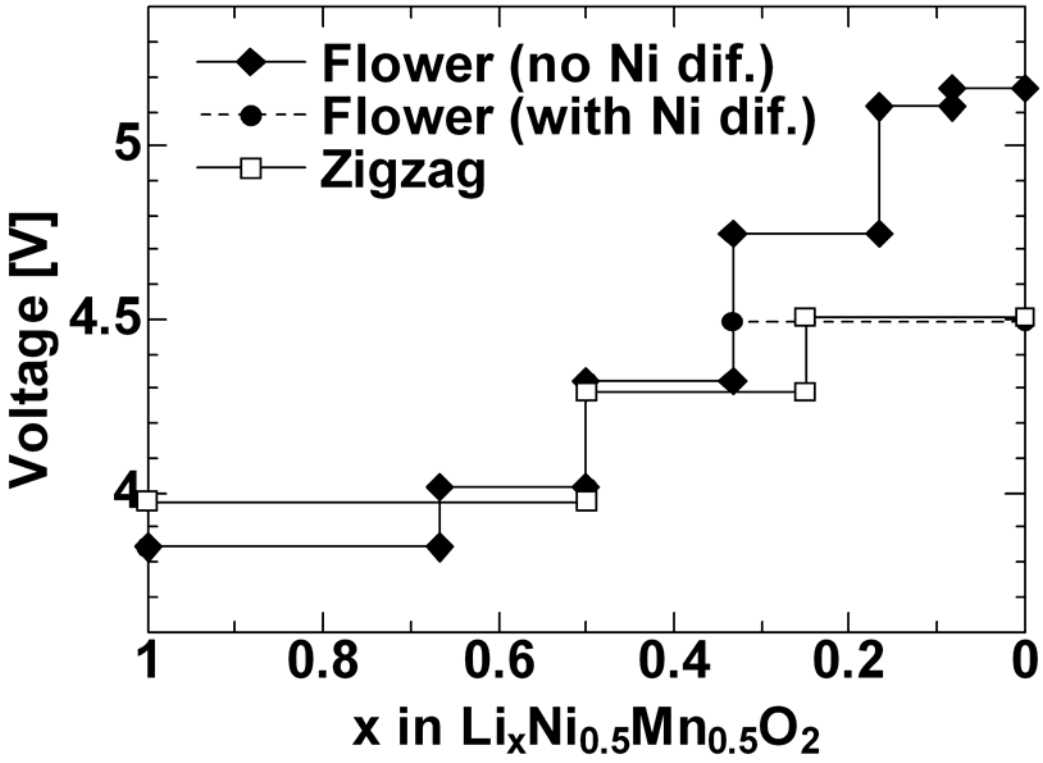

Figure 3-5. Voltage curves for different delithiation scenarios.

3.4.3 Cluster expansion

In the cluster expansion presented here, clusters were selected from a pool including all pair interactions up to 7th cation-cation Nearest Neighbor (NN) distance, and triplets with a maximum pair subcluster up to 3rd NN distance. Any pairs that span over three or more cation layers and triplets that include only sites in the Li layer were removed. There is 1 empty cluster, 1 point cluster, 22 pair clusters and 28 triplet clusters in the pool. From this pool, a set of relevant clusters and ECI were obtained with a weighted average cross validation (CV) score of 6.94 meV/FU and weighted root mean square error of 3.43 meV/FU. The CV score may be thought as the prediction error. A CV score of about 7meV can be considered to be small enough for this study because the energy difference between flower and zigzag structures is 26meV/FU (see Table 3-1). Table 3-2 shows the ECI obtained from this fit, and the clusters defining the interactions are shown in Figure 3-6. Note that clusters including sites that can be occupied by three species (TM layer sites) need multiple ECI per cluster to independently represent the energy contribution of each possible configuration on that cluster. For more detailed discussions of ternary and higher component representations in the cluster expansion, the reader is referred to references (*46-48*).

The set of ECI in Table 3-2 is used in the Monte Carlo calculations. It should be noted that an additional penalty of 1eV per pair is added to Ni-Ni pairs in the Li layer to

avoid Li / Ni segregation in the Li layer, because it is well known from experiment that there are no Ni clusters in the Li layer. The addition of this penalty was required because it was not possible to accurately sample first principles energies of structures that include NN Ni-Ni pairs in the Li layer. Doing so would result in strong electrostatic repulsion because spin density integration of these structures reveals that electrons do not localize properly on Ni. This is an indication that such configurations are very high in energy. The exact magnitude of the penalty is not important because these configurations are not allowed to appear in the simulation so they do not affect the value of the average energy.

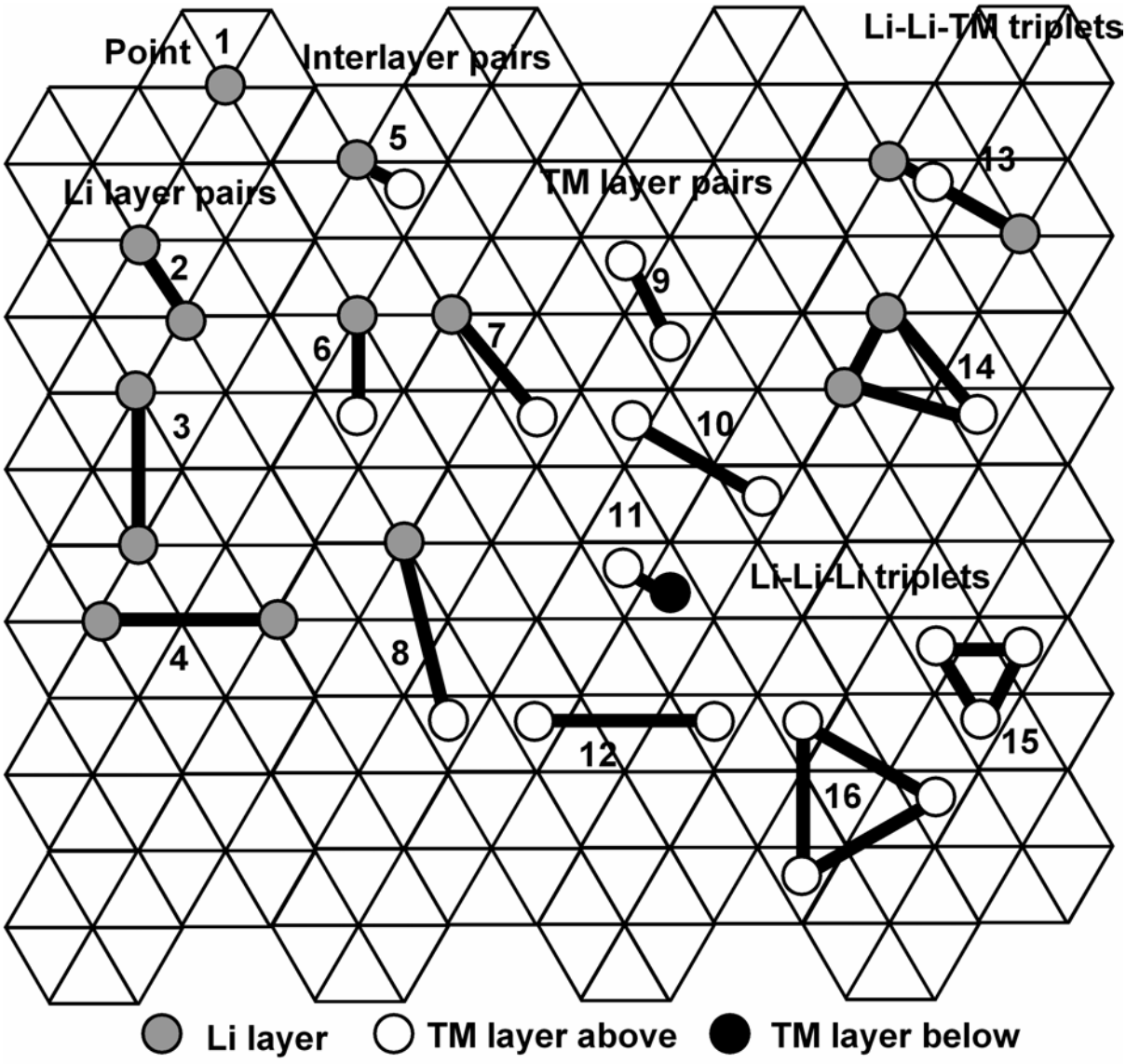

Figure 3-6. Clusters used in the cluster expansion.

Table 3-2. Values of ECI used in Monte Carlo calculations. Clusters corresponding to each number are shown in Figure 8.

Point cluster: V_0= –452.6 meV

Pairs [meV]								
Li layer pairs		**Interlayer pairs**			**TM layer pairs**			
Cluster	**V^{Li}_{11}**	**Cluster**	**V^{int}_{11}**	**V^{int}_{21}**	**Cluster**	**V^{TM}_{11}**	**$V^{TM}_{21}=V^{TM}_{12}$**	**V^{TM}_{22}**
2	107.5	5	–90.8	22.2	9	434.8	73.0	656.7
3	–6.1	6	–101.8	52.4	10	-24.6	7.2	1.2
4	–32.3	7	18.7	11.0	11	15.5	14.2	31.0
		8	–13.1	–1.2	12	71.3	–15.1	8.7

Triplets [meV]							
Li-Li-TM triplets			**TM-TM-TM triplets**				
Cluster	**V^{int1}_{1}**	**V^{int1}_{2}**	**Cluster**	**V^{TM}_{111}**	**$V^{TM}_{112}=V^{TM}_{121}=V^{TM}_{211}$**	**$V^{TM}_{122}=V^{TM}_{212}=V^{TM}_{221}$**	**V^{TM}_{222}**
13	17.8	–21.5	15	–25.0	25.8	–13.1	–61.3
14	30.8	–90.1	16	113.7	12.3	–45.1	–378.7

3.4.4 Monte Carlo simulation

Figure 3-7a shows the thermally averaged energy as a function of increasing temperature in Monte Carlo calculations starting from either a zigzag structure or a flower structure. Even though the flower structure has higher energy at low temperature, it does not transform to the zigzag configuration, indicating that the flower configuration is metastable. In addition, low temperature Monte Carlo calculations reveal that the energy of the partially disordered flower structure (about 10 meV/FU) is significantly lower than the energy of the perfect flower structure (about 26 meV/FU). This indicates that some change takes place in the structure with essentially no kinetic barrier. The driving force of such a change will be discussed later in section 3.5.1. Monte Carlo simulations show that the zigzag structure undergoes a phase transition close to $T_1 \sim$ 810K, but above this temperature its energy is equal to that of the flower structure. This is indicative of the two initial phases becoming the same phase. Furthermore, an additional phase transition occurs is found at $T_2 \sim 870$K in both sets of calculations.

Figure 3-7b shows the thermally averaged heat capacity from the calculations. This heat capacity only includes the effect of configurational entropy. The result of the zigzag structure simulation show two heat capacity peaks at T_1 and T_2, which are consistent with the two phase transitions observed in the energy in Figure 3-7a. The heat

capacity peak in the simulation starting from the flower structure only shows a single peak at T_2.

Figure 3-8 shows the Li/Ni disorder, measured as the concentration of Ni in the Li layer and averaged over 50 snapshots of structures at each temperature. The snapshots of the structures were taken at regular intervals (every 2000 passes) during the sampling calculations. The Li/Ni disorder of the zigzag phase is close to zero at the start of the simulation, however, it increases to 8~9% at the first phase transition at $T = T_1$. Above $T > T_1$, the Li/Ni disorder amount seems to be independent of the starting configuration of the simulation, consistent with the results of the energy and heat capacity calculations.

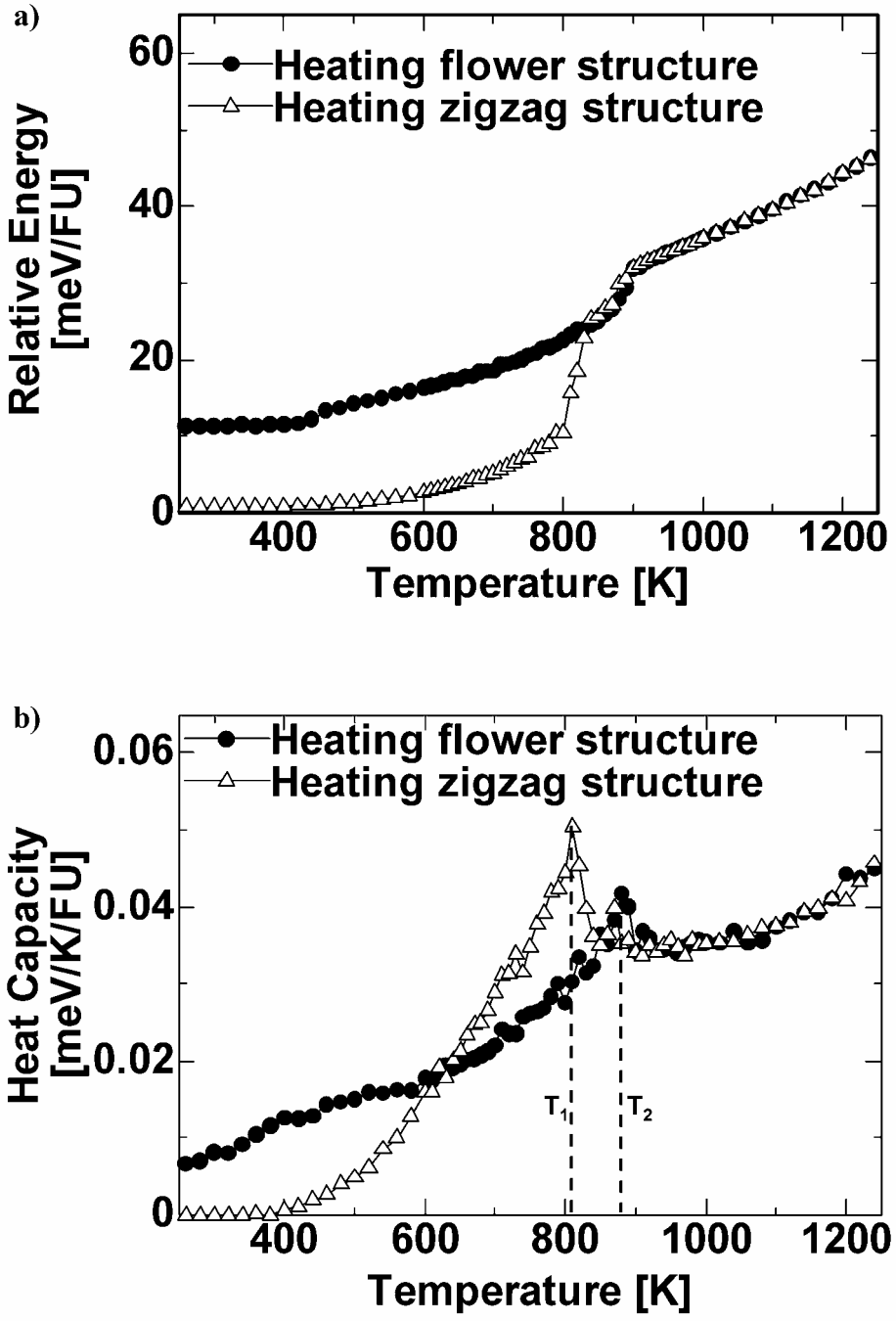

Figure 3-7. (a) Monte Carlo energy as a function of temperature. (b) Monte Carlo heat capacity as a function of temperature.

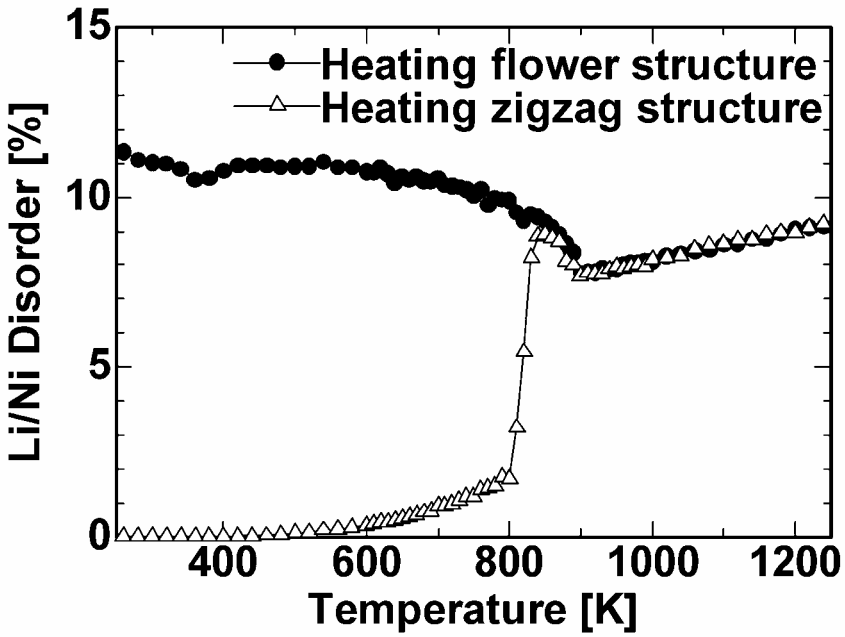

Figure 3-8. Calculated Li/Ni exchange between the Li and TM layers as a function of temperature.

Figure 3-9 is a snapshot of the structure at 850K, which is just above the first phase transition. Figure 3-9a is a good representation of cation arrangement in the TM layer at this temperature range regardless of the starting configuration. There are well-formed "flower" rings consisting of a Li ion surrounded by six Mn ions, which in turn are surrounded by a larger Ni ring. However, substantial disorder, such as $LiMn_5Ni$ rings, Ni-Mn zigzag domains, and even a few $MnNi_6$ rings are present. The presence of Li surrounded by five Mn and one Ni (as in a $LiMn_5Ni$ ring) was also observed in NMR (*30*). The ordering in the TM layer discussed further below seems to correlate clearly with the ionic occupation and ordering in the adjacent Li layers.

The cation ordering patterns observed in the Monte Carlo simulations shows significant local charge imbalance in structures below T_2. When flower patterns exist, as shown in Figure 3-9a, there is a corresponding 2×2 ordering pattern of Ni and Li in the Li layer as seen in Figure 3-9b, making this specific region excess in Ni. Although the Monte Carlo cell as a whole is charge balanced, the Monte Carlo snapshot of the Li layer in Figure 3-9b shows concentration of Ni that is a few percent higher than the average Li/Ni disorder value in Figure 3-8.

Above T_2, the Ni present in the Li layer disorders and no longer arranges in 2×2 patterns. This can be observed in a snapshot of the structure at 1200K in Figure 3-10. Although the TM layer shown in Figure 3-10a appears completely disordered, the average site occupations correspond to the honeycomb scheme mentioned in section 3.2 (*30, 31*). Li and Ni positions seem to be uncorrelated in the Li layer as shown in Figure 3-10b.

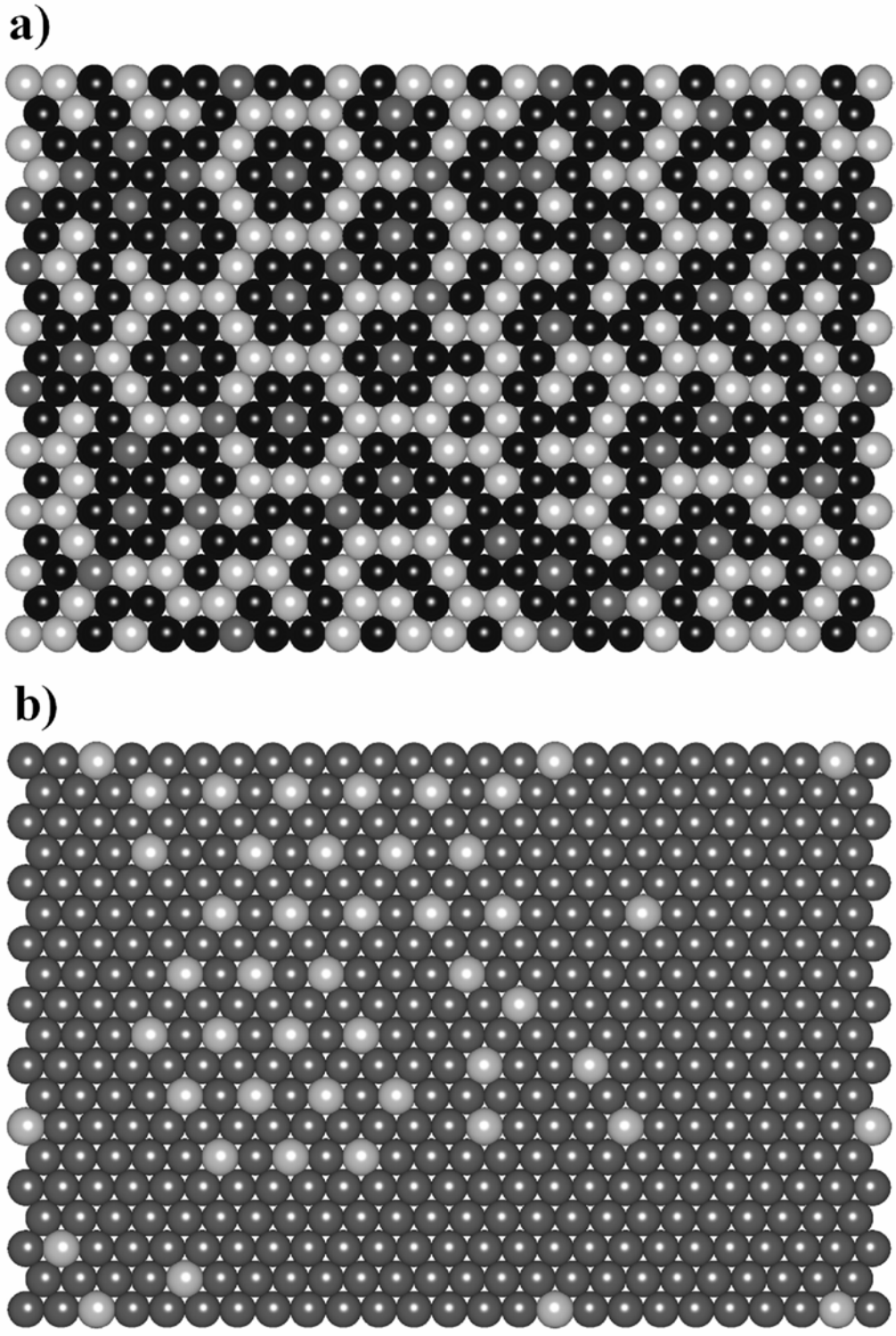

Figure 3-9. Monte Carlo snapshot at T = 850K of (a) transition metal-rich layer; (b) Li-rich layer. Legend: black: Mn, white: Ni, gray: Li.

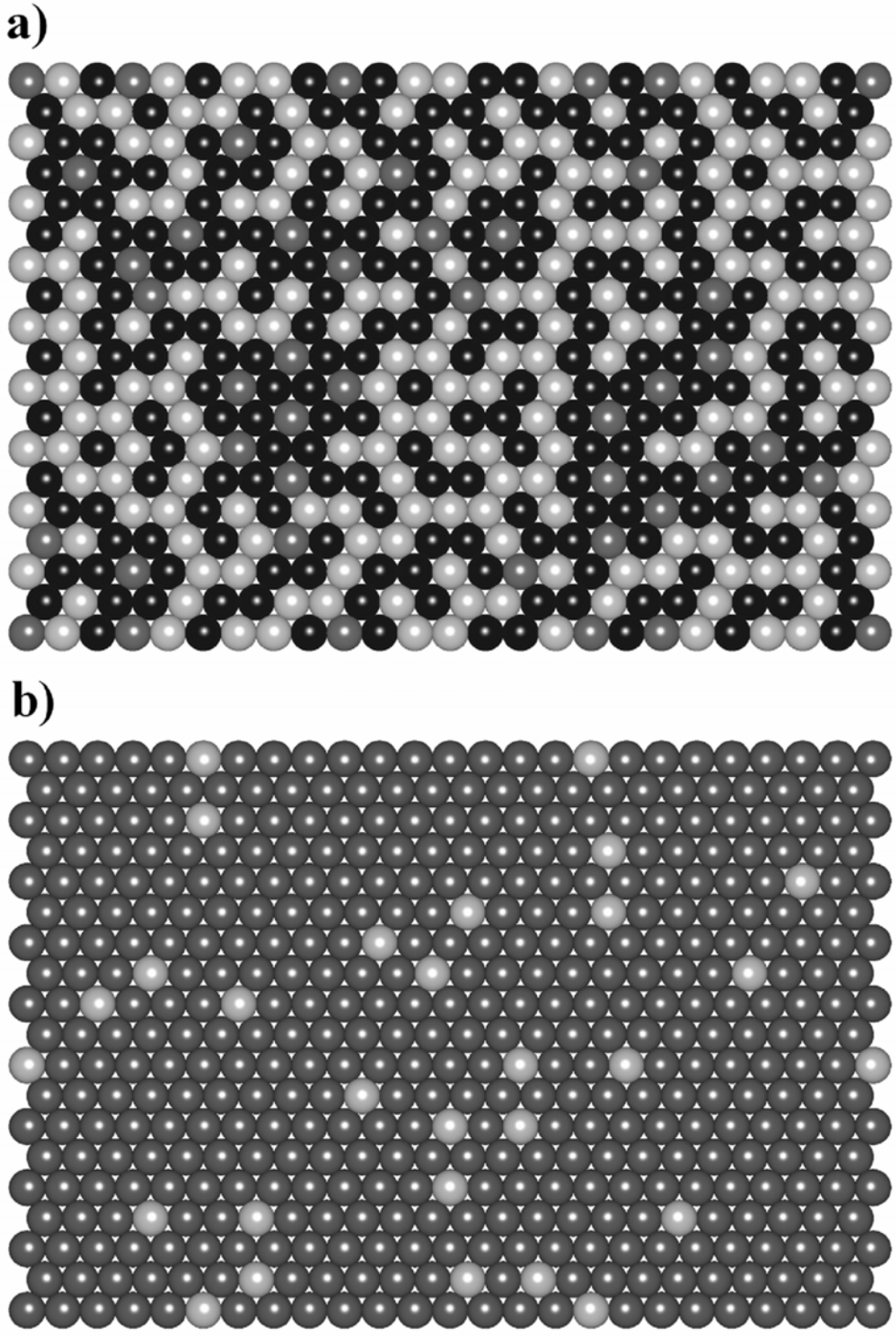

Figure 3-10. Monte Carlo snapshot at T = 1200K of (a) transition metal-rich layer; (b) Li-rich layer. Legend: black: Mn, white: Ni, gray: Li.

3.5 Discussion

3.5.1 Driving force for the order-disorder transformation in the flower structure

The Monte Carlo simulation shows the most energetically stable cation ordering in the $LiNi_{0.5}Mn_{0.5}O_2$ system as a function of temperature as well as revealing some of the physics that drive the ordering. The flower pattern can be considered to be a superstructure of the honeycomb structure. In the flower ordering, Li orders in $2\sqrt{3} \times 2\sqrt{3}$ patterns in the TM layer. This pattern can be mapped perfectly onto the α sites of the honeycomb pattern, which has $\sqrt{3} \times \sqrt{3}$ ordering. The central Li atoms in the flower structure occupy 1/4 of the α sites, with Ni occupying the remaining α sites. Mn ions, which occupy the six sites surrounding Li, are all located on β sites. Hence the transformation from the partially ordered flower structure to honeycomb ordering is an order-order transformation whereby Li and Ni disorder on the α sites. Several physical interactions seem to contribute to the ordering into a flower-like arrangement. First, flower ordering was previously shown (*49*) to be the electrostatically favored configuration of +1, +2 and +4 cations on a two-dimensional triangular lattice describing the TM layer. However, this alone does not seem to fully capture the energetics of the flower structure. The difference between the GGA and GGA+U computation also helps to elucidate the order mechanism. These results point to Ni_{TM} - O - Ni_{Li} superexchange between the Li and TM layers which as driving the honeycomb pattern to further order into the flower arrangement (*25*). Finally when the spins on the Ni in the TM layer and Li

layer are aligned antiferromagnetically, the Ni 3*d* orbitals can each hybridize with the same spatial (but different spin) oxygen 2*p* orbital and delocalize onto the oxygen. This interaction is consistent with the Goodenough-Kanamori rules (*50*). We have some evidence that this antiferromagnetic interaction is crucial for the stability of the flower. When Ni spins are forced to be ferromagnetic in GGA calculations the flower structure is not the most stable state (*25*). Furthermore, flower patterns do not form without Li in the TM layer, or in other words, without including Ni in the Li layer (*30*). A similar case in which interactions that bridge an oxygen are an important factor in the structural stability is the Li_A-O-Ni^{3+}-O-Li_B 180-degree interaction in $LiNiO_2$ (*51, 52*).

As seen in Figure 3-9, the flower pattern is accompanied by a 2 × 2 ordering of Ni in the Li layer. The stability of the 2 × 2 pattern can be rationalized by looking at the flower structure in three dimensions (Figure 3-11a). The top and bottom layers show the flower patterns in the TM layer. There are three sites for each flower unit in the Li layer between the two layers (shown in dark gray) that can have the maximum of four Ni_{TM} - O - Ni_{Li} bonds. Occupation of *all* these sites by Ni results in 2 × 2 ordering of Ni in the Li layer, as is observed in the Monte Carlo calculations.

The competition between the Ni_{TM} - O - Ni_{Li} bonding and local charge neutrality leads to frustration in the flower ordered $LiNi_{0.5}Mn_{0.5}O_2$ system. Complete 2 × 2 ordering of Ni in the Li layer would lead to a local charge imbalance in regions that have perfect

flower ordered in the TM layer. The solution to these competitive forces seems to be to create somewhat higher Li/Ni disorder than the 8.3% (1/12) of the perfectly ordered flower structure. This additional Li/Ni exchange creates more (less) Ni in the Li (TM) layer and as such *increases* the number of Ni_{TM} - O - Ni_{Li} bonds that can be formed. This is why more Li/Ni disorder is created (about 11%) in the Monte Carlo simulations as soon as the temperature is above 0K (Figure 3-8). However, increasing Li/Ni exchange leads to more Li in the TM layer other than the core site of the flower. The Li in sites other than the core site have higher site energy, as they are only coordinated by three or four Mn. Therefore, a Li/Ni exchange of 8 ~ 11 % is observed as a balance of creating favorable Ni_{TM} - O - Ni_{Li} bonds and unfavorable Li sites in the TM layer. This may also explain why the Li/Ni disorder *decreases* with temperature: As the flower structure partially disorders, the frustration between the local charge balance and the Ni_{TM} - O - Ni_{Li} bonding can be more easily resolved and requires less additional Li/Ni exchange. Note in particular how the Li/Ni disorder rapidly decreases in our simulation as the partially disordered flower further disorders into the honeycomb structure at about 620^{o}C (see Figure 3-8).

3.5.2 Partially disordered flower structure

One way to understand the partially disordered flower structure is to look at the structure in both the layered R-3m and the spinel Fd-3m space group settings. In

LT-$LiCoO_2$, an example of a lithiated spinel-like material, Li occupies 16*c* sites and Co occupies 16*d* sites (*13*). The relations between the flower structure in the layered and spinel space group settings are similar and depicted in Figure 3-11. Figure 3-11b shows the layered flower structure, but with the sites marked in the spinel setting: the Li layer is composed of 75% 16*c* sites and 25% 16*d* sites, and the TM layer is composed of 25% 16*c* sites and 75% 16*d* sites. The Ni sites in the Li layer that are likely to create more Ni_{TM} - O - Ni_{Li} superexchange bonds are labeled as Li/Ni sites in Figure 3-11a. Note that these Li/Ni sites correspond to the Li layer 16*d* sites in Figure 3-11b. The 16*c* sites in the Li layer are unlikely to contain Ni because these sites do not have the maximum possible number of Ni_{TM} - O - Ni_{Li} superexchange bonds when the TM layer has a perfect flower ordering. The 16*c* sites in the TM layer (top and bottom layers of Figure 3-11b) correspond to the "core" of the flower (the site surrounded by a Mn ring) and the six "corners" of the flower. Each corner is simultaneously a corner of three flower motifs, so there are two corner sites for each core site. The core is Li and the corners are Ni in the perfect flower structure shown in Figure 3-11c. This means that about 2/3 (66.7%) of the 16*c* sites in the TM layer, which amount to 25% of all 16c sites, are occupied by Ni. Therefore, Ni occupies 1/6 (16.7%) of the total 16c sites in the spinel setting of the flower model because there is no Ni in the 16*c* sites of the Li layer. On the other hand, Li occupies 2/3 of the 16*d* sites in the Li layer in the flower structure. In fact, full occupation of all 16*d* sites in the Li layer by Ni can happen with relatively low energy penalty if the additional Li created in the TM layer only occupies the 16*d* sites in the TM layer ("edge"

sites). This exchange leads to the extreme case of a partially disordered flower structure as shown in Figure 3-11d: an ordered structure with all Li/Ni sites (16*d*) in the Li layer occupied by Ni. In the TM layer, Li occupies some flower "edge" sites (16*d*), maintaining charge balance of the system as a whole. This configuration has lower energy than the perfect flower structure in GGA+U calculations, but still higher energy than the zigzag structure due to unfavorable Li site occupation in the TM layer. Interestingly, the Li occupancy on the TM-rich 16*d* sites, or the Ni occupancy on the Li-rich 16*c* sites is 1/6, although in this scenario, the Li/Ni disorder has increased from 8.3% to 25%. It can be clearly seen that the partially disordered flower structure has the characteristics of both layered (with 3*a*/3*b* disorder) and spinel (with 16*c*/16*d* disorder) features. One example of such case is in the $LiNi_{0.5}Mn_{0.5}O_2$ sample annealed at 600^{o}C by Lu et al (*13*). Rietveld refinement showed 16.1% Li/Ni disorder between the Li and TM layers in the layered setting, and 17.4% Li/Ni disorder between Li-rich 16c sites and TM-rich 16d sites in the spinel setting (*13*).

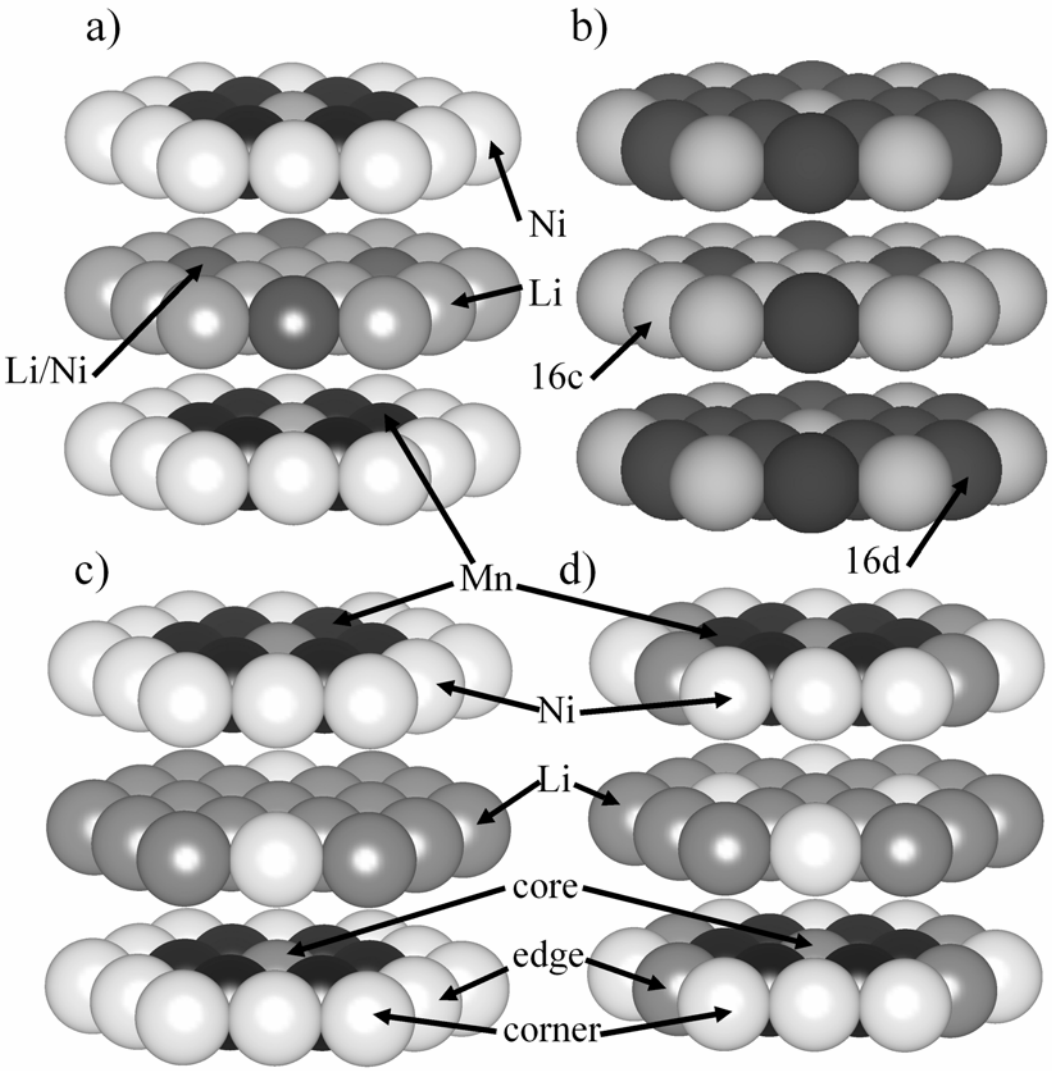

Figure 3-11. (a) Flower structure with emphasis on interaction across layers. Of the 12 sites in the Li layer per flower unit, there are three sites that have four Ni-Ni second nearest neighbors. The Ni in the Li layer prefers these sites. Legend: black: Mn, white: Ni, light gray: Li, dark gray: Li/Ni sites. (b) The flower unit viewed in the spinel setting. Legend: light gray: Li-rich 16c sites, dark gray: Li-poor 16d sites. (c) Perfect flower structure. (d) Partially disordered flower structure with lower first principles energy than the flower shown in (c). Legend: black: Mn, white: Ni, gray: Li.

3.5.3 Phase transitions

As seen in Figures 3-7 and 3-8, the Monte Carlo simulation clearly shows that upon heating the zigzag structure, at a certain critical temperature (T_1) a phase transition occurs to the flower phase. The perfect flower structure must have achieved higher entropy than the zigzag structure at T_1 because it has higher energy at 0K. The entropy difference can be rationalized through the excitations available for both phases. The zigzag phase has fewer low-energy excitation states than the flower phase. The excitations observed in snapshots of the Monte Carlo simulation from the zigzag phase are simple exchanges of Li and Ni between the Li and TM layers. However, Li in the TM layer prefers to be surrounded by all Mn, which is not possible when it occupies a Ni position in the zigzag structure. Breaking the zigzag ordering in the TM layer requires relocation of a large number of cations, which is difficult in Monte Carlo simulations at low temperatures. Therefore, putting Li in the TM layer of the zigzag phase carries a heavy energy penalty since Li can at best be surrounded by four Mn. In contrast, the majority of Li are surrounded by six Mn in the flower phase. In addition, the flower patterns can form and disintegrate relatively easily in the honeycomb framework in the TM layer (*30, 31*). The honeycomb ordering guarantees that no Li-Li nearest-neighbor pairs occur in the TM layer, which would come with a strong electrostatic energy penalty. Also the flower phase becomes stable above a certain temperature where the zigzag phase cannot tolerate much Li/Ni disorder because of the difference in excitations.

Such a phase transition from a low Li/Ni disorder phase to a high disorder phase is indeed experimentally observed using both XRD and DSC/TEM (*53*), and together with the simulation results paint a consistent picture of the phase evolution of $LiNi_{0.5}Mn_{0.5}O_2$. Based on to the simulation results, IE-$LiNi_{0.5}Mn_{0.5}O_2$, a representative material with little or no Li/Ni site disorder (*53*), is probably the stable phase at low temperature, and transforms to a partially disordered flower arrangement near 810K. The phase transition temperature obtained from DSC measurement (*53*) is about 873K. The latent enthalpy obtained from DSC peak integration of the phase transition is about 1.2 kJ/mol for IE-$LiNi_{0.5}Mn_{0.5}O_2$, however could not be accurately determined due to the fact that the phase transition is unfinished at 873K due to partial transformation of some large particles (*53*). The latent heat for this transformation obtained from Monte Carlo simulations is about 1 kJ/mol, consistent with the DSC result.

It was also found in our Monte Carlo simulations that the phase transition from zigzag to flower is *not* reversible upon cooling. The values of the energy, heat capacity, and Li/Ni disorder for cooling track closely the values obtained during heating of the flower structure. This can only be explained by a kinetic limitation because zigzag, not flower, is the thermodynamic ground state at low-enough temperature. One possible reason for the irreversibility may lie in the extreme stability of the Li in the transition metal layer. Those Li ions are typically surrounded by five or six Mn ions and this configuration is very difficult to break up due to its favorable short-range electrostatic

interactions. This keeps the Li ions in the transition metal layer and prevents the formation of zigzag configurations. Such kinetic limitations observed in our first-principles Monte Carlo simulations may be a representation of reality, since even slow cooling of $LiNi_{0.5}Mn_{0.5}O_2$ samples never leads to low Li/Ni disorder.

The Monte Carlo simulation indicates that the partially disordered flower structure undergoes a phase transition to the honeycomb structure upon heating above temperature T_2 (~620^{o}C). The well-defined heat capacity peak in Figure 3-7b indicates that this is a phase transition, rather than a gradual disordering of the flower structure. We were not able to study this transition in our DSC experiment because of the limited temperature range and resolution of the instrument. However, this phase transition implies the existence of a possible intermediate phase between the ground state and the high temperature disordered state of $LiNi_{0.5}Mn_{0.5}O_2$, and may be a reason why some of the literature shows that the electrochemical behavior of $LiNi_{0.5}Mn_{0.5}O_2$ strongly depends on the processing temperature (*13, 28*).

The combined simulation and DSC data (*53*) lead us to propose the phase diagram in Figure 3-12. The temperatures included are derived from the simulations. At low temperature, a structure with little or no Li/Ni exchange is the ground state. Above ~810K, this structure transform to a partially disordered flower structure with regions of substantial Li/Ni mixing. At slightly higher temperature around 620^{o}C, the flower

structures disintegrate and partially disorder becoming the honeycomb structure. However, only the flower structure can be obtained upon cooling.

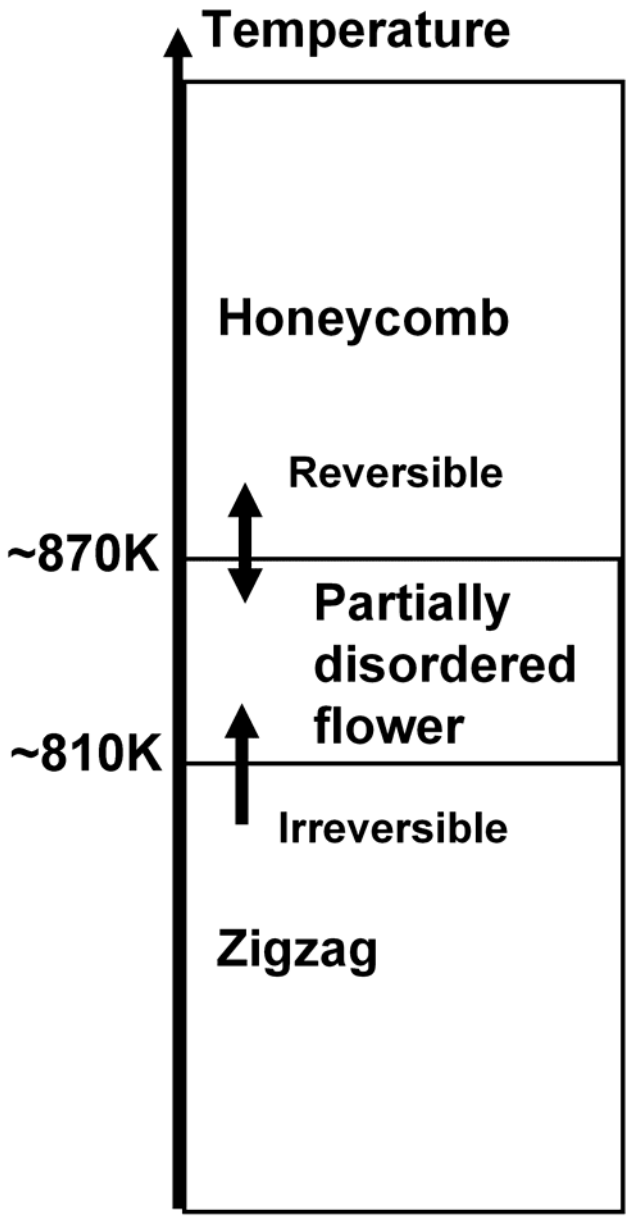

Figure 3-12. Schematic phase diagram of $LiNi_{0.5}Mn_{0.5}O_2$. The temperatures were are based on simulations results.

3.5.4 Limitation of the simulation

Finally, the limitations of our approach should be noted. Locally non-charge-balanced structures appear easily in Monte Carlo simulations of $LiNi_{0.5}Mn_{0.5}O_2$, for example in Figure 3-7. The electrostatic repulsion of locally charged regions is underestimated due to the use of short-range cluster expansion. If the structure is locally charge balanced, then electrostatic forces from relatively small regions decay rapidly, because the net charge of that small region is close to zero and multipole (dipole, quadrupole, and higher) terms dominate at longer ranges (*54*). These multipole terms decay very quickly, making the cluster expansion applicable to such systems. In reality, the electrostatic forces extend to long range for locally non-charge-balanced systems. While the short-range term of the electrostatics is captured in the ECI, the long-range part is not.

3.6 Conclusion

The cation ordering in $LiNi_{0.5}Mn_{0.5}O_2$ is a complex function of the temperature and the heating/cooling history. The zigzag model, which has very little Li/Ni disorder, is the ground state of $LiNi_{0.5}Mn_{0.5}O_2$ in the GGA+U approach. A model that points out the phase transition upon heating in the $LiNi_{0.5}Mn_{0.5}O_2$ system is discussed with underlying physics, and a phase diagram is proposed as shown in Figure 3-12. Zigzag ordering first

transforms to a partially disordered flower structure, which upon further heating, transforms to a disordered honeycomb structure. The cluster expansion and Monte Carlo simulation of GGA+U energies match TEM, DSC, and XRD results (*53*) along with previous NMR studies (*35*)**.** Once cation exchange between Li and TM layers occurs, and Mn rings form around the Li in the TM layer, it is very difficult to break up the ring, explaining why states with low Li/Ni disorder cannot be obtained by cooling from high temperature. The unusual ordering of this material with temperature is due to the competition between electrostatics and Ni_{TM} - O - Ni_{Li} hybridization. Li / Ni disorder in $LiNi_{0.5}Mn_{0.5}O_2$ leads to Li in tetrahedral sites during delithiation that negatively impacts battery properties and requires high voltage to remove. Therefore, it is crucial not to heat low Li/Ni disorder materials above a critical temperature where Li/Ni exchange would occur, which is around 810K.

3.7 References

1. J. M. Tarascon, M. Armand, *Nature* **414**, 359 (Nov 15, 2001).
2. T. Nagaura, K. Tozawa, *Progress in Batteries and Solar Cells* **9**, 209 (1990).
3. J. B. Goodenough, A. Manthiram, B. Wnetrzewski, *Journal of Power Sources* **43**, 269 (Mar 15, 1993).
4. A. Van der Ven, G. Ceder, *Journal of Power Sources* **97-8**, 529 (Jul, 2001).
5. T. Ohzuku, A. Ueda, *Journal of the Electrochemical Society* **141**, 2972 (Nov, 1994).
6. G. G. Amatucci, J. M. Tarascon, L. C. Klein, *Journal of the Electrochemical Society* **143**, 1114 (Mar, 1996).
7. A. Van der Ven, M. K. Aydinol, G. Ceder, G. Kresse, J. Hafner, *Physical Review B* **58**, 2975 (1998).
8. J. R. Dahn, E. W. Fuller, M. Obrovac, U. von Sacken, *Solid State Ionics* **69**, 265

(1994/8, 1994).
9. M. Winter, J. O. Besenhard, M. E. Spahr, P. Novak, *Advanced Materials* **10**, 725 (Jul 9, 1998).
10. T. Ohzuku, Y. Makimura, *Chemistry Letters*, 642 (Jul 5, 2001).
11. T. Ohzuku, Y. Makimura, *Chemistry Letters*, 744 (Aug 5, 2001).
12. Y. Makimura, T. Ohzuku, *Journal of Power Sources* **119**, 156 (Jun 1, 2003).
13. Z. H. Lu, L. Y. Beaulieu, R. A. Donaberger, C. L. Thomas, J. R. Dahn, *Journal of the Electrochemical Society* **149**, A778 (Jun, 2002).
14. Z. H. Lu, D. D. MacNeil, J. R. Dahn, *Electrochemical and Solid State Letters* **4**, A191 (Nov, 2001).
15. M. E. Spahr, P. Novak, O. Haas, R. Nesper, *Journal of Power Sources* **68**, 629 (1997).
16. K. Kang, Y. S. Meng, J. Breger, C. P. Grey, G. Ceder, *Science* **311**, 977 (Feb 17, 2006).
17. J. Reed, G. Ceder, *Chemical Reviews* **104**, 4513 (Oct, 2004).
18. J. Reed, G. Ceder, A. Van Der Ven, *Electrochemical and Solid-State Letters* **4**, A78 (2001).
19. K. Kang, C. H. Chen, B. J. Hwang, G. Ceder, *Chemistry of Materials* **16**, 2685 (2004).
20. C. Delmas, C. Fouassier, P. Hagenmuller, *Physica* **99B**, 81 (1980).
21. Y. Arachi *et al.*, *Solid State Ionics* **176**, 895 (Mar 15, 2005).
22. M. S. Islam, R. A. Davies, J. D. Gale, *Chemistry of Materials* **15**, 4280 (Nov 4, 2003).
23. Y. S. Meng, G. Ceder, C. P. Grey, W. S. Yoon, Y. Shao-Horn, *Electrochemical and Solid State Letters* **7**, A155 (2004).
24. Y. S. Meng *et al.*, *Chemistry of Materials* **17**, 2386 (2005).
25. A. Van der Ven, G. Ceder, *Electrochemistry Communication* **6**, 1045 (2004).
26. J. Breger *et al.*, *Journal of the American Chemical Society* **127**, 7529 (May 25, 2005).
27. H. Kobayashi, Y. Arachi, H. Kageyama, K. Tatsumi, *Journal of Materials Chemistry* **14**, 40 (2004).
28. Z. H. Lu, Z. H. Chen, J. R. Dahn, *Chemistry of Materials* **15**, 3214 (Aug 12, 2003).
29. Z. Lu, D. D. MacNeil, J. R. Dahn, *Electrochemical and Solid State Letters* **4**, A200 (2001).
30. W. S. Yoon *et al.*, *Electrochemical and Solid State Letters* **7**, A167 (2004).

31. C. P. Grey, W. S. Yoon, J. Reed, G. Ceder, *Electrochemical and Solid State Letters* **7**, A290 (2004).
32. J. Reed, G. Ceder, *Electrochemical and Solid State Letters* **5**, A145 (Jul, 2002).
33. W. S. Yoon *et al.*, *Electrochemical and Solid State Letters* **5**, A263 (2002).
34. W. S. Yoon *et al.*, *Journal of the Electrochemical Society* **151**, A246 (Feb, 2004).
35. J. Breger *et al.*, *Journal of Solid State Chemistry* **178**, 2575 (Sep, 2005).
36. G. Ceder, A. Van der Ven, C. Marianetti, D. Morgan, *Modelling and Simulation in Materials Science and Engineering* **8**, 311 (May, 2000).
37. M. de Dompablo, A. Van der Ven, G. Ceder, *Physical Review B* **66** (Aug 1, 2002).
38. F. Zhou, T. Maxisch, G. Ceder, *Physical Review Letters* **97**, 155704 (2006).
39. P. E. Blochl, *Physical Review B* **50**, 17953 (Dec 15, 1994).
40. G. Kresse, J. Furthmuller, *Computational Materials Science* **6**, 15 (Jul, 1996).
41. J. P. Perdew, K. Burke, Y. Wang, *Physical Review B* **54**, 16533 (Dec 15, 1996).
42. F. Zhou, M. Cococcioni, C. A. Marianetti, D. Morgan, G. Ceder, *Physical Review B* **70**, 235121 (Dec, 2004).
43. F. Zhou, K. Kang, T. Maxisch, G. Ceder, D. Morgan, *Solid State Communications* **132**, 181 (Oct, 2004).
44. P. D. Tepesch, G. D. Garbulsky, G. Ceder, *Physical Review Letters* **74**, 2272 (Mar 20, 1995).
45. J. Breger *et al.*, *Chemistry of Materials* **18**, 4768 (Oct 3, 2006).
46. R. McCormack, D. Defontaine, C. Wolverton, G. Ceder, *Physical Review B* **51**, 15808 (Jun 15, 1995).
47. G. Ceder, G. D. Garbulsky, D. Avis, K. Fukuda, *Physical Review B* **49**, 1 (Jan 1, 1994).
48. G. Inden, W. Pitsch, *Materials Science and Technology: A comprehensive treatment (eds. Cahn, R. W., Haasen, P. & Kraamer, E. J.)*, 497 (1991).
49. G. Ceder, *IMLB 14 meeting* (2004).
50. J. Kanamori, *Journal of Physics and Chemistry of Solids* **10**, 87 (1959/7, 1959).
51. M. de Dompablo, G. Ceder, *Chemistry of Materials* **15**, 63 (Jan 14, 2003).
52. M. de Dompablo, G. Ceder, *Journal of Power Sources* **119**, 654 (Jun 1, 2003).
53. Y. Hinuma, Y. S. Meng, K. Kang, G. Ceder, *Chemistry of Materials* **19**, 1790 (Apr 3, 2007).
54. G. Ceder, G. D. Garbulsky, P. D. Tepesch, *Physical Review B* **51**, 11257 (May 1, 1995).

Chapter 4 The thermoelectric material Na_xCoO_2

4.1 Introduction to thermoelectric materials (*1*)

Electric and thermal currents are two related phenomena because both can involve electrons or holes. Seebeck noted that when a temperature gradient (ΔT) exists between two sides of a material or between two dissimilar materials, there is a corresponding voltage difference (ΔV) between these two sides (Seebeck effect). The Seebeck coefficient, or thermopower (S), is defined as

$$\Delta V = S\Delta T \,. \tag{4.1}$$

Peltier discovered that heat transfer happens between two sides of a material, or between two dissimilar materials, if there is a voltage difference between the sides (Peltier effect). This effect is the opposite of the Seebeck effect. Lord Kelvin realized that if temperature gradients exist on a conductor carrying electric current, heat generation or absorption occurs (Thompson effect). These three effects are different from Joule heating, where heat is irreversibly dissipated with flow of electric current.

The Seebeck and Peltier effects can be used to convert electricity directly into heat and vice versa, and materials that do this efficiently (i.e. have a high Seebeck coefficient) are called thermoelectric materials. The Seebeck effect can be used to generate electric current. One application is deep space probes, where the heat source is a

nuclear reactor and the heat sink is outer space. The Peltier effect can be used to make coolers without any mechanical parts, which minimizes noise and reduces the need for maintenance, and is useful for supercomputing.

The efficiency of thermoelectric materials are measured by the figure of merit (Z) defined as

$$Z = S^2\sigma/\kappa \tag{4.2}$$

where σ is the electric conductivity and κ is the thermal conductivity. Thermal conductivity can be separated into contributions from electrons and phonons, and both have to be taken into account. The dimensionless figure of merit (ZT), which is the product of Z and the temperature (T), is also used frequently. A good thermoelectric material should have high Seebeck coefficient, high electric conductivity but low thermal conductivity.

In metals, the Wiedemann-Franz-Lorenz law states that

$$\kappa/T\sigma = L, \tag{4.3}$$

where the Lorenz number (L) is empirically determined as approximately 2.45×10^{-8} V^2K^{-2} (Sommerfeld value). This is because at high temperature heat and electrical transport are both primarily governed by the free electrons in the metal. The Seebeck coefficient Strong ground states occur only at concentrations where the Co ordering pattern is commensurate with the symmetry of the Na lattice (*27*). Co orders with a

supercell of $a_{hex} \times \sqrt{3}a_{hex}$, $\sqrt{3}a_{hex} \times \sqrt{3}a_{hex}$, and $2a_{hex} \times 2a_{hex}$ at x = 0.5, 0.67, and 0.75 respectively. The Na layer ordering for these structures is $2a_{hex} \times \sqrt{3}a_{hex}$, $2\sqrt{3}a_{hex} \times 2\sqrt{3}a_{hex}$ and $2\sqrt{3}a_{hex} \times 2\sqrt{3}a_{hex}$ respectively.

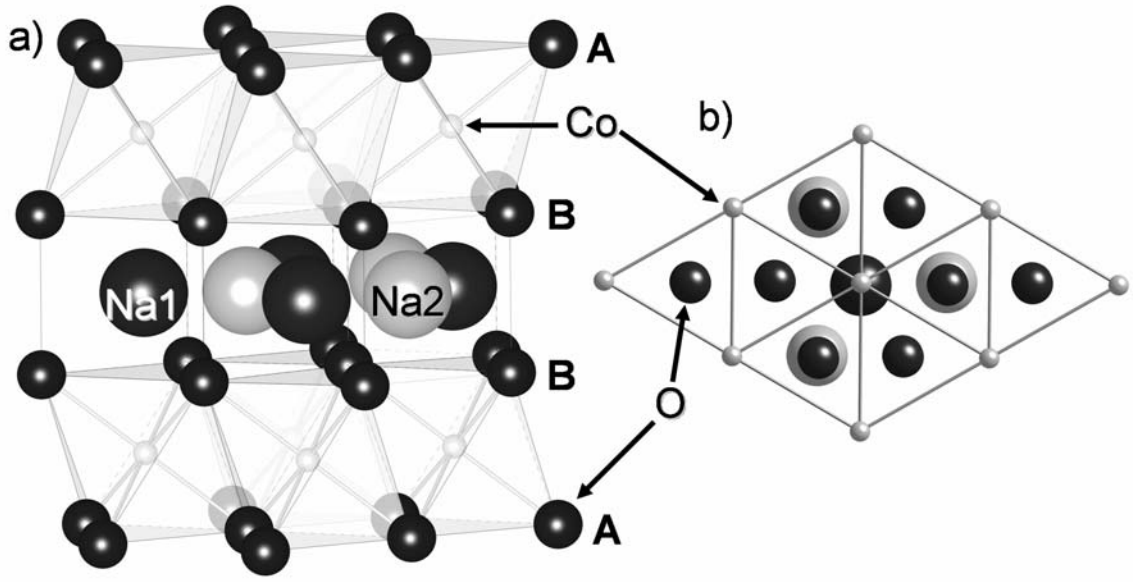

Figure 4-2. Two perspectives of the layered P2-Na_xCoO_2 structure. (a) View perpendicular to the layers to show the oxygen stacking. (b) Top view to show relative positions of Na1, Na2, Co and oxygens.

Despite the enormous interest in P2-Na_xCoO_2, its structure as a function of Na concentration is not fully characterized. Experimental (*19-23*) and theoretical (*20, 24-26*) work has led to proposed structures for several Na-vacancy ordered states. The ground state ordering of $Na_{0.5}CoO_2$ has been determined experimentally with electron diffraction (*21, 23*) and is in agreement with results from first principles calculations (*24, 25*). Three ordering schemes are proposed at the composition $Na_{0.75}CoO_2$ based on experiments. The

first, referred to as the "droplet" phase by Roger et al. from neutron diffraction (*20*) with $2\sqrt{3}a_{hex} \times 2\sqrt{3}a_{hex}$ ordering and formation of isolated three-Na1 droplet motifs. The second, known as the "stripe" phase, found by Geck et al. from high energy X-ray diffraction (*22*) with $2a_{hex} \times 2\sqrt{3}a_{hex}$ ordering and formation of three-Na1 and three-Na2 droplet motifs that are connected by two corners each to droplets of the same type. Thirdly, the "diamond" phase by Zandbergen et al. from electron diffraction (*21*) with $4a_{hex} \times \sqrt{3}a_{hex}$ ordering and formation of connected diamond-like Na1 and Na2 motifs. The "diamond" phase is also computationally suggested as a ground state by Zhang et al. (*25*), however detailed first principles calculations by Meng et al. (*26*) show that a different "zigzag" structure with $4a_{hex} \times \sqrt{3}a_{hex}$ ordering where Na1 orders in a zigzag pattern has lower energy. At $x > 0.85$, six-Na1 droplet patterns (*24, 27*), analogous to the three-Na1 droplet motifs by Roger et al. (*20*), are suggested by computation.

Understanding and predicting the Na-vacancy ordering is complicated by the fact that the Co ions have an average valence $+(4-x)$, and the nature of this mixed valence state is under considerable dispute. Whether or not charge localizes on Co and forms distinct Co^{3+} and Co^{4+} ions is an important issue that will affect Na-vacancy ordering. Bond length analysis from neutron diffraction shows delocalization of Co charge in $Na_{0.5}CoO_2$ (*16*), however magnetic susceptibility and conductivity measurements suggest that at low temperatures $Na_{0.5}CoO_2$ is a charge-ordered insulator (*28*). Magnetic

susceptibility and conductivity measurements also suggest that Na_xCoO_2 is a Curie-Weiss metal between $0.5 < x < 0.75$ and is in a weak-moment magnetically ordered state at $x \geq 0.75$, possibly because of spin density waves. Specifically, at $x = 0.65$ (*29*) and ~ 2/3 (*28*) these measurements imply delocalization of Co charge. In contrast, partial localization of Co charge is suggested at $x = 0.75$ by observation of a magnetic transition (*30*), and from results of muon spin rotation and relaxation (*31*) and neutron scattering (*32*) measurements. The presence of superstructures with antiferromagnetic ordering at $x = 0.82$ observed during neutron scattering measurements also suggests partial localization of charge on Co (*33*). Another possibility that should not be excluded is that both delocalized and localized Co^{4+} holes exist depending on the local Na arrangement. Some evidence exists for a strong coupling between the Na positions and charge on the Co ion. For example, Marianetti and Kotliar proposed a computational model within the Dynamic Mean Field Theory (DMFT) in which a Co^{4+} hole that is nearest neighbor to a Na1 is penalized by 400 meV (*17*). Hence occupancy of the Na1 sites in this model reduces the number of Co ions over which holes can delocalize and encourages Co^{4+} localization. Comparing results from the GGA and GGA+U methods, Meng et al. (*26*) showed that the Na-vacancy ordering is strongly coupled with Co^{3+}/Co^{4+} charge ordering in $Na_{0.75}CoO_2$.

Phase transition temperatures of Na_xCoO_2 have been experimentally measured at key compositions. Electronic and magnetic transitions have been observed at 87K, 53K, and 20K for one such composition, $x = 0.5$ (*23*). Additional structural transitions at 210K

and 410 ~ 470K have been observed by electron diffraction (*34*), and incipient localization of holes are reported to be evident at 300K (*28*). A magnetic ordering is found below 22K (*35*), and resistivity transitions are observed at approximately 285K and 315K at $x = 0.75$ (*20*), while no magnetic transition has been found down to 2K for $x = 0.65$ (*35*).

The cause of high Seebeck coefficient in Na_xCoO_2 is debated because there are many sources of entropy that contribute to the thermopower, and different types of entropy may dominate at different temperatures. There is a configurational degree of freedom of what Na sites to occupy. It is possible that there is partial charge localization on Co, therefore there may be an electronic degree of freedom. Co^{3+} has no spin, but Co^{4+} has non-zero spin, meaning that there is spin (magnetic) degree of freedom on Co^{4+}. The asymptoted spin contribution to the thermopower is two-thirds of the total thermopower from experimental results by Wang et al (*36*). Koshibae et al. theoretically deduced that electronic entropy causes high thermopower in $Na_{0.5}CoO_2$ (*37, 38*). However, evaluation of the Na configurational entropy contribution to the total thermopower is difficult, and there are few detailed investigations.

It is necessary to note that it is difficult to experimentally obtain the exact stoichiometry. Chou et al. (*39*) point out the possibility of oxygen non-stoichiometry in Na_xCoO_2 on single crystals prepared with the floating zone method. $Na_{0.75}CoO_2$ prepared

with the floating zone method was observed to cross two tie lines upon heating close to 1020°C. An oxygen deficiency level of $\delta \sim 0.073$ was observed in $Na_{0.7}CoO_{2-\delta}$ prepared in air (*40*) while $\delta \sim 0.08$ was observed in $Na_{0.75}CoO_{2-\delta}$ prepared in an oxygen atmosphere (*39*). Oxygen deficiency is important as it modifies the relation between the Na content and the average Co-valence. Additional error in the stoichiometry may result for impurities such as CoO_x formation, as been suggested both by magnetic susceptibility measurement (*41*) and differential thermal analysis (*39*) of samples prepared with the floating zone method. Finally, samples with Na concentration lower than $x = 0.7$ are usually prepared by removal of Na with I_2 from $Na_{0.75}CoO_2$ (*16, 18*) though composition control of the final product is very difficult. Electrochemical methods to alter the Na content (*8, 19*) offer better control provided that the composition of the initial compound is accurately determined.

First principles methods are used to study the temperature-composition phase diagram of P2-Na_xCoO_2 for $0.5 \leq x \leq 1$ in this work. The dependence of the energy on Na-vacancy configuration (or Co^{3+}/Co^{4+} configuration) is accounted for using the cluster expansion technique, so that Monte Carlo simulations can be used to equilibrate the system at non-zero temperature. Both the GGA and GGA+U methods are used to construct the phase diagram, allowing us to understand how charge localization on Co affects the Na-vacancy ordering. The objective of this work is to computationally determine the significant interactions in this material, the ordered states and their

transition temperatures as a function of Na concentration, and to gain an understanding of the role that possible $Co^{3+/4+}$ charge localization plays on the phase diagram.

4.3 Methodology

4.3.1 First principles calculations

First principles calculations were performed on various ordered arrangements in the spin-polarized GGA and GGA+U method. Core electron states were represented by the Projector Augmented-Wave method (*42*) as implemented in the Vienna Ab Initio Simulation Package (VASP) (*43*). All Co^{4+} spins were initialized ferromagnetically while Co^{3+} has no net spin because it is low spin in these materials. The Perdew-Burke-Ernzerhof (PBE) exchange correlation (*44*) and a plane wave representation for the wavefunction with a cutoff of 450 eV were used. Both internal coordinates and unit cell lattice parameters were fully relaxed, unlike in previous work (*22, 24, 25*) where the unit cell lattice parameters were fixed. Full relaxation has been reported to be crucial in identifying the correct order of phase stability (*27*). The Brillouin zones were sampled with a mesh including the gamma point. The density of the mesh for all calculations is approximately one point per 0.01 $Å^{-3}$. The Hubbard U value in the Hamiltonian ($U_{eff} = U - J$, or afterwards simply U) is taken to be 5eV for Co in the GGA+U calculations. This U value is between the values of $U = 4.91$eV for Co^{3+} and $U = 5.37$eV for Co^{4+} obtained with first principles perturbation theory in Li_xCoO_2 (*45*). It was previously shown that

removal of the self-interaction leads to strong charge localization and significant changes in the ground state structures in related systems (*45, 46*). A value of U = 5eV is sufficient to cause hole localization in $Na_{0.5}CoO_2$ (*47*) and is consistent with our previous work on $Na_{0.75}CoO_2$ (*26*), but slightly higher than the value in the work by Wang et al. (*24*) (U = 4eV). The rotationally invariant approach to GGA+U by Liechtenstein et al. (*48*) was used for calculations in this work for consistency with previous work (*26*), but different from the rotationally invariant approach by Dudarev et al. (*49*) used by Wang et al. (*24*).

4.3.2 Cluster expansion

The Na sites can be described by a lattice model, with variables describing whether Na, or a vacancy, sits on each site. The essential idea is to expand the energy of the system in terms of these variables. For the GGA approximation, using the occupation variables $\sigma = 1$ for Na, and $\sigma = -1$ for vacancies for Na sites, the Hamiltonian becomes:

$$E_\nu^{predict} = C + \sum_{i \in Na1\,site} V^{Na1}\sigma_i + \sum_{i \in Na2\,site} V^{Na2}\sigma_i + \sum_{i,j} V^{ij}\sigma_i\sigma_j + \sum_{i,j,k} V^{ijk}\sigma_i\sigma_j\sigma_k + \ldots \tag{4.4}$$

Here, $E_\nu^{predict}$ is the predicted energy for structure ν, C is a constant, and V represents the Effective Cluster Interactions (ECI). The point terms are broken out explicitly in Na1-type and Na2-type sites in equation 4.4. The energy difference between Na on a Na1 and a Na2 site, averaged over all possible occupations surrounding the sites is given by $2\left(V^{Na1} - V^{Na2}\right)$. The indices i, j and k are labels of sites in the interaction cluster. The

final GGA cluster expansion was fitted to the energies of 211 different Na-vacancy configurations in the concentration range $0.5 \le x \le 1$.

An additional problem of organizing charge occupancy on Co^{3+}/Co^{4+} appears in the GGA+U approximation. This is complicated by the interaction between the Na / vacancy and Co^{3+} / Co^{4+} sublattices. Such a system, with two partially disordered sublattices that interact with each other, can be studied with a coupled cluster expansion (*50-52*). The GGA+U cluster expansion Hamiltonian becomes:

$$E_v^{predict} = C + \sum_{i \in Na2\ site} V^{Na2}\sigma_i + \sum_{i \in Co\ site} V^{Co}\tau_i + \sum_{i,j} V^{ij}\sigma_i\sigma_j + \sum_{i,j} V^{ij}\sigma_i\tau_j + \sum_{i,j} V^{ij}\tau_i\tau_j + \sum_{i,j,k} V^{ijk}\sigma_i\sigma_j\sigma_k + \sum_{i,j,k} V^{ijk}\sigma_i\sigma_j\tau_k + \sum_{i,j,k} V^{ijk}\sigma_i\tau_j\tau_k + \sum_{i,j,k} V^{ijk}\tau_i\tau_j\tau_k + \ldots \quad (4.5)$$

where the occupation variables are $\sigma = 1$ for Na, and $\sigma = -1$ for vacancies for Na sites, and $\tau = 1$ for Co^{3+}, and $\tau = -1$ for Co^{4+} at Co sites. Note that due to the charge balance constraint,

$$\sum_{i \in Na1\ site} \sigma_i + \sum_{i \in Na2\ site} \sigma_i - \sum_{i \in Co\ site} \tau_i = const. \quad (4.6)$$

,

one interaction term for a point variable must be removed. The ECI for the Na1 point term was removed in our cluster expansion. Hence the point ECI for Na2 and Co^{3+} / Co^{4+} are taken with respect to this term. The final GGA+U cluster expansion was fitted to the energies of 131 different Na-vacancy and Co^{3+}/Co^{4+}configurations in the concentration range $0.5 \le x \le 1$.

It was necessary to subtract a "background cluster expansion" prior to fitting the

first principles energies to the cluster expansion to capture the slowly decaying long-range electrostatic interactions in the Na layers in the GGA cluster expansion. The background cluster expansion is defined as

$$E'_{\nu} = \sum_{In\text{-}plane\ pair} V'_{ij}\sigma_i\sigma_j \tag{4.7}$$

with

$$V'_{ij} = A\frac{erfc(\alpha r_{ij})}{\alpha r_{ij}}. \tag{4.8}$$

Here, r_{ij} is the distance in angstroms between two sites *i* and *j* that form the pair cluster. *A* (magnitude) and α (decay length) are constants that are manually chosen. The background interaction V_{ij}' has the same form as the real-space term in an Ewald summation, which was shown to reproduce well low energy structures in ionic systems governed by unscreened electrostatic interactions (*53*). The cluster expansion in equation 4.4 is fitted to energies $E_{GGA,\nu} - E'_{\nu}$ instead of directly fitting to first principles energies $E_{GGA,\nu}$.

The phase space for which first principles energies can be obtained is limited because Na1-Na2 nearest neighbor (NN) simultaneous occupancy cannot be stabilized in both GGA and GGA+U approximations due to overlapping of ions. Furthermore, Na1-Co^{4+} NN simultaneous occupancy drastically increases the energy in the GGA+U approximation due to strong electrostatic repulsion. Therefore clusters that include the Na1-Na2 NN pair cluster, or Na1-Co NN pair cluster in the GGA+U cluster expansion, as

a subcluster were not included in the cluster expansion. A penalty of 1eV per Na1-Na2 NN simultaneous occupancy and 400meV per Na1-Co^{4+} NN simultaneous occupancy was added to discourage formation of such pairs in the Monte Carlo simulations. The exact magnitude of the Na1-Na2 NN pair penalty is not important, because these configurations do not affect the value of the average energy as long as they do not appear in the simulation. However, since there is no overlap of ions involved, there is no reason to prohibit Na1-Co^{4+} NN simultaneous occupancy in Monte Carlo simulations at high enough temperatures, and the magnitude of this penalty is chosen to be the same as the value in Marianetti and Kotliar (*17*).

4.3.3 Monte Carlo simulations

Grand Canonical Monte Carlo simulations were conducted within the Metropolis algorithm (*54*) for both the GGA and GGA+U based cluster expansion in order to determine ground states and subsequently derive the phase diagrams. Monte Carlo cells with up to approximately 30,000 Na sites, or 15,000 formula units (FU) containing one Co per FU, were used.

The cluster expansion based on GGA utilized 80,000 equilibrium passes and 120,000 sampling passes at 10K intervals for calculations at fixed chemical potential, and at least half the number of passes were used when the chemical potential was scanned at

650K for integration of free energy. The perturbation in the Metropolis algorithm was a sign inversion of the occupation variable in one site and one sampling pass amounts to one possible perturbation for each site on the lattice.

The GGA+U calculations utilized 40,000 equilibrium passes and 60,000 sampling passes at 10K intervals for temperature scans at fixed chemical potential, and half this number of passes for a chemical potential scan at 750K. The perturbation for the Metropolis algorithm was chosen with the following algorithm to ensure charge balance:

1) Choose a first site randomly.
2) Choose a second site randomly.
3) If inverting the occupation variables in both sites changes the charge balance, discard the choice of the second site and go to 2).
4) Else, the perturbation is inverting the occupation variables in both sites.

One sampling pass amounts to one possible selection as the first candidate site for inversion per site on the lattice. Some phase transition temperatures are obtained by free energy integration because of large hysterisis near the phase transition point between heating and cooling calculations.

4.4 Results

4.4.1 GGA

4.4.1.1 Formation energies and ground states

Figure 4-3a shows the GGA formation energy per FU, which is the energy of a structure compared to phase separation into the lowest energy structures with P2 stacking at x = 0.5 and x = 1. The dotted line in Figure 4-3a shows the convex hull when O3-$NaCoO_2$ (shown with the gray diamond) is considered as an end member. The ground state for $NaCoO_2$ is O3-$NaCoO_2$ (*55*). When oxygen ions are stacked as ABCABC and Na and Co occupy octahedral sites in alternating layers; its energy is 45meV/FU lower than that of P2-$NaCoO_2$. This is why it is difficult to obtain single phase P2-Na_xCoO_2 with Na concentrations above $x > 0.8$ during electrochemical experiments, as in Delmas et al (*8*). Two ground states at $x \sim 0.84$ and 0.86 are removed from the convex hull when O3-$NaCoO_2$ is added on the convex hull.

Figure 4-3b-j shows in-plane Na ordering patterns of the ground state structures, which can be grouped into three types of ordering patterns (*27*). One is the "row" pattern of x = 0.5 (= 2/4, Figure 4-3b) (*21, 23*), 0.56 (= 5/9, Figure 4-3c) and 0.6 (= 3/5, Figure 4-3d), in which Na1 sites order in rows parallel to the $\boldsymbol{a_1}+2\boldsymbol{a_2}$ direction with single or double Na2 rows interdispersed. Another is the "large zigzag" pattern for x = 0.67 (= 4/6, Figure 4-3e) and 0.71 (= 5/7, Figure 4-3f), where Na1 sites form a zigzag pattern with

distance $2|\boldsymbol{a_1}|$ between nearest Na1 sites. The third is the "droplet" pattern for $x = 0.77$ (= 10/13, Figure 4-3g), 0.81 (= 13/16, Figure 4-3h), 0.84 (= 16/19, Figure 4-3i) and 0.86 (= 18/21, Figure 4-3j), where three Na1 form droplet motifs.

Na orders in rows either on Na1 or on Na2 sites at $x = 0.5$, 0.56, and 0.6 (Figure 4-3b-d). The previously proposed structure at $x = 0.5$ (*18, 21*) has equal occupancy of Na1 and Na2 which serves to minimize the electrostatic energy by eliminating Na1-Na1 or Na2-Na2 nearest neighbor interactions. The ordered state, in which all Na atoms form zigzag lines on Na2 sites while no Na1 sites are occupied, has 23meV/FU higher energy. Hence, the ground state gains stability by minimizing the electrostatic repulsions among Na ions even though half of its Na are ordered on less favorable sites (i.e. Na1). The ground state structure at 0.6 (Figure 4-3d) is obtained from the one at $x = 0.5$ by inserting an additional row of Na2 ions between the Na1 rows, thus creating some Na2-Na2 nearest neighbors. We can assume that these row motifs also occur at compositions $0.5 < x < 0.6$ because the common characteristic of the ground states at $x = 0.5$ and $x = 0.6$ is the formation of rows of Na1 and Na2 ions. This assumption reduces the ground state problem, for that concentration range, to finding how the Na1 and Na2 rows alternate along the direction perpendicular to them. The ground states of such one-dimensional models are well known because of the seminal work of Hubbard who found the ground states for arranging electrons and vacant sites on a one-dimensional lattice (*56*). A similar analysis has been applied to explain the oxygen ordering in yttrium barium copper oxides

(*57*). In the Na_xCoO_2 system, a unit consisting of a row of Na1 ions with a vacant row on each side are denoted by <‘1’>, while <2> represents a row of Na2 ions. For example, the ground states at x = 0.5 and x = 0.6 can be denoted as <‘1’2> and <‘1’22> respectively. Repulsive convex decaying interactions are typical of electrostatically interacting systems. In general, these interactions exhibit an infinite branching tree of ground states generated by a continued-fraction algorithm, which is equivalent to a structure combination branching mechanism (*58*). For example, a new ground state would be expected at $x = \frac{2+3}{4+5} = \frac{5}{9}$ (0.56) with Na ordering <‘1’2‘1’22>. Indeed, the first principles energy of this structure (Figure 4-3c) is lower than the compositionally weighted average of <‘1’2> and <‘1’22> structures. It is likely that the continued fraction algorithm leads to additional ground state structures as is the case in $YBa_2Cu_3O_{7-\delta}$ (e.g. for $x = \frac{2+5}{4+9} = \frac{7}{13}$ and $x = \frac{5+3}{9+5} = \frac{8}{14}$) (*57*), but the very large size of the unit cell precludes their energy calculations with DFT. While one could extend the ordering scheme for x > 0.6, the local environment of the “large zigzag” pattern is favored within this concentration range because Na can be separated more evenly.

4.4.1.2 Cluster Expansion

The clusters included in the GGA cluster expansion are shown in Figure 4-4, however in-plane pair clusters that only contribute to the background are not shown. The circles at the intersections of the lines correspond to Na1 sites, and circles inside triangles

represent Na2 sites. Na2 sites are either all at the center of up-pointing triangles or all at the center of down-pointing triangles in one Na layer. These two occupancy patterns alternate as a result of P2 stacking. The circles in black correspond to sites in one layer, and circles in gray represent sites in an adjacent layer. The weighted CV score of this cluster expansion is 4.37meV/FU, while the root mean square (RMS) error was 3.29meV/FU. In-plane ordering of the cluster expansion ground state structures matches the ordering of the first principles ground states within the set of calculated structures.

Figure 4-5 shows the total ECI (including background) for the GGA cluster expansion. Although all clusters are not shown, the non-zero background, shown as the curve in Figure 4-5, is applied to in-plane pair clusters up to 18Å (the Na1-Na1 NN distance is 2.93Å). The background ECI used here is:

$$V'_{ij} = 12\frac{erfc(0.095r_{ij})}{0.095r_{ij}} \text{ [meV]}. \quad (4.9)$$

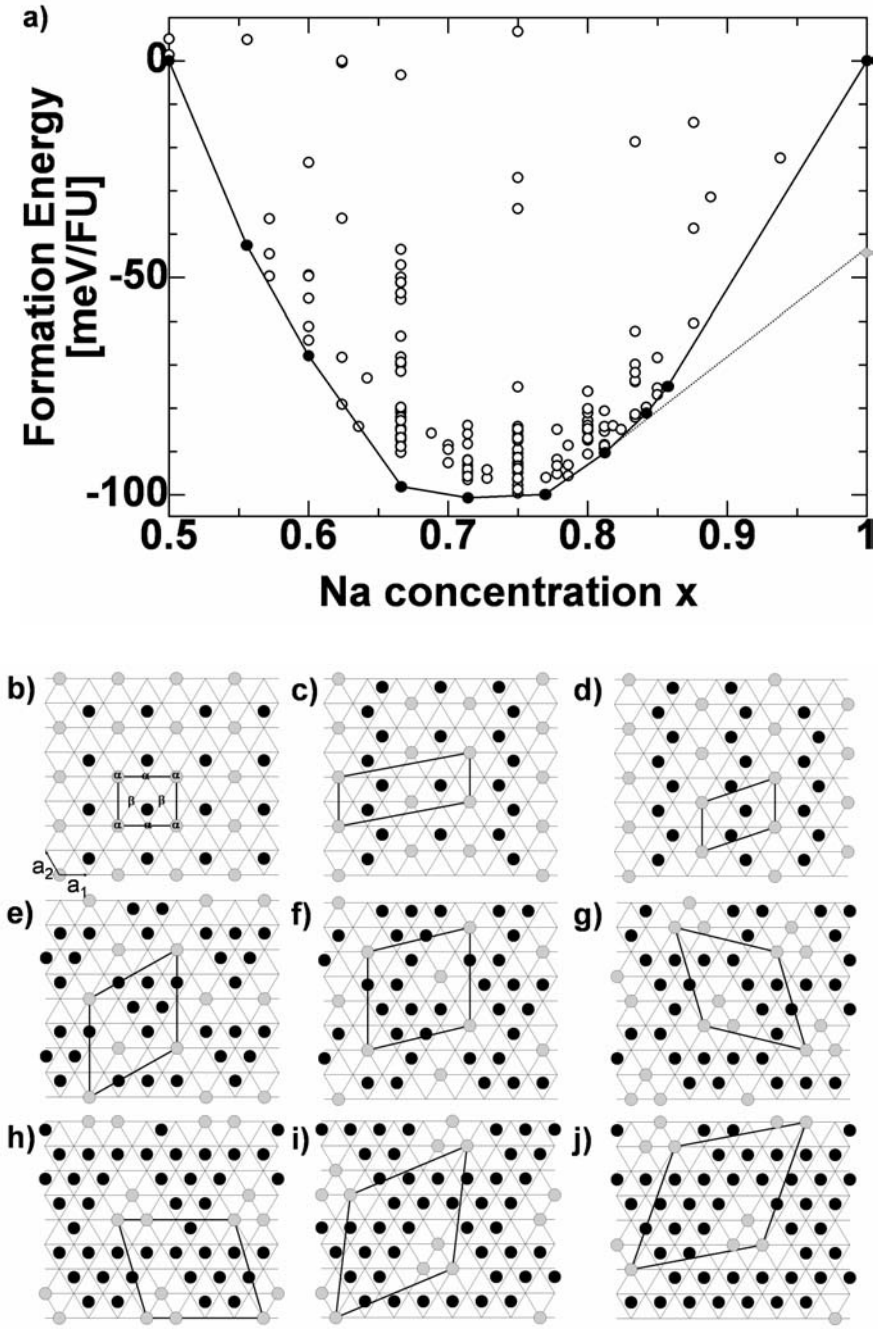

Figure 4-3. (a) First principles GGA formation energy per formula unit. The bold solid line shows the convex hull. The convex hull changes to the dotted line when formation of O3-$NaCoO_2$ (gray diamond) is allowed. (b-j) In-plane ordering of the GGA ground states at x = (b) 0.5, (c) 0.56 (5/9), (d) 0.6, (e) 0.67 (4/6), (f) 0.71 (5/7), (g) 0.77 (10/13), (h) 0.81 (13/16), (i) 0.84 (16/19) and (j) 0.86 (18/21) respectively. Legend: Gray circles: Na1, black circles: Na2. Bold lines indicate unit cell. The symbols α and β in (b) indicate the distinction of α and β sites for order parameter calculation on the Na1 sublattice.

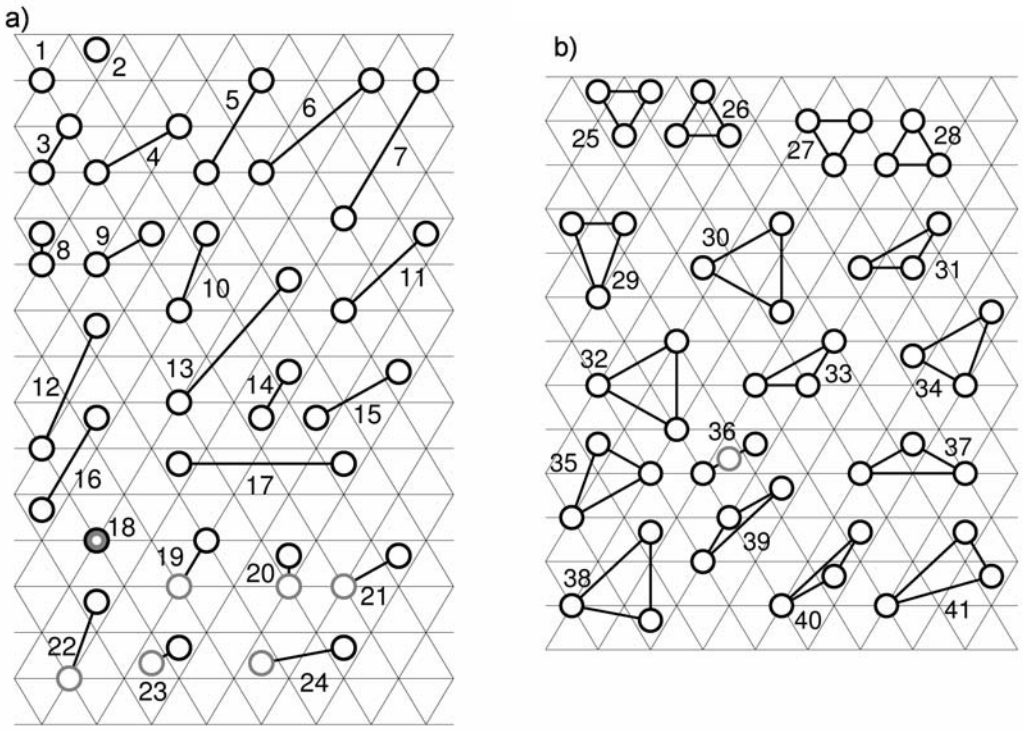

Figure 4-4. Clusters with ECI different from the background included in the GGA cluster expansion. The circles at the intersections of the lines correspond to Na1 sites, and circles inside triangles represent Na2 sites. Circles in black correspond to sites in one layer, and circles in gray represent sites in an adjacent layer. (a) Point and pair clusters. (b) Triplet clusters.

We can clearly observe that both in-plane and out-of-plane interactions are repulsive and convex decaying, and that the out-of-plane interactions decay much faster than the in-plane interactions. This work presents the treatment of out-of-plane interactions as weaker, but not negligible, interactions as compared to in-plane interactions. This treatment is different from previous computational studies, in which electrostatic interactions out-of-plane and in-plane were not distinguished (*20, 25*). Furthermore, the magnitude of the pair interactions seems insensitive to whether the sites

in the pair are Na1 or Na2 sites. Table 4-1 shows the sum of the background ECIs and the fitted ECIs for clusters with non-zero value of the fitted ECIs. Note that the cluster numbers in Table 4-1 correspond to the numbers in Figure 4-4. The Na1-Na2 site energy difference $2\left(V^{Na1} - V^{Na2}\right)$ obtained from Table 4-1 is 61meV per Na. This value determined in this work compares well to previous calculations by Zhang et al., which obtained a value of 67meV for Na1-Na2 site energy difference (*25*).

The fundamental interactions in Na_xCoO_2 were previously considered to be electrostatic in-plane (*20, 25*) or short-range pair interactions (*24*). Contrary to these speculations, we find that there are three different types of interactions, namely strong long-range in-plane electrostatic interactions, strong relaxation effects, and weak short-range out-of-plane interactions. The in-plane screening mechanism is weak since they are less screened by the oxygen ions compared to out-of-plane interactions that extend over oxygen layers. We find that, in addition to electrostatic interactions, relaxation effects are necessary to accurately capture the energetics of the system, therefore many triplet clusters had to be included in the cluster expansion. There is "empty space" between Na1 and patches of Na2 because simultaneous Na1-Na2 NN occupancy is not possible. Relaxation of the structure during first principles calculations reduces this empty space. For example, the average relaxed Na1-Na2 second nearest neighbor distance (corresponding to cluster 9 in Figure 4-4) was consistently about 0.15 Å; about 5% shorter than the distance on an ideal hexagonal lattice with the same cell

volume in the ground state structures for x = 0.67, 0.71 and 0.76 (Figures 4-3e-g). These relaxation effects can only be correctly captured by including triplets, or higher order clusters, in the cluster expansion. The importance of capturing Na1-Na2 distances is shown by the fact that most significant triplets include a Na1-Na2 pair cluster as a subcluster (see Figure 4-4).

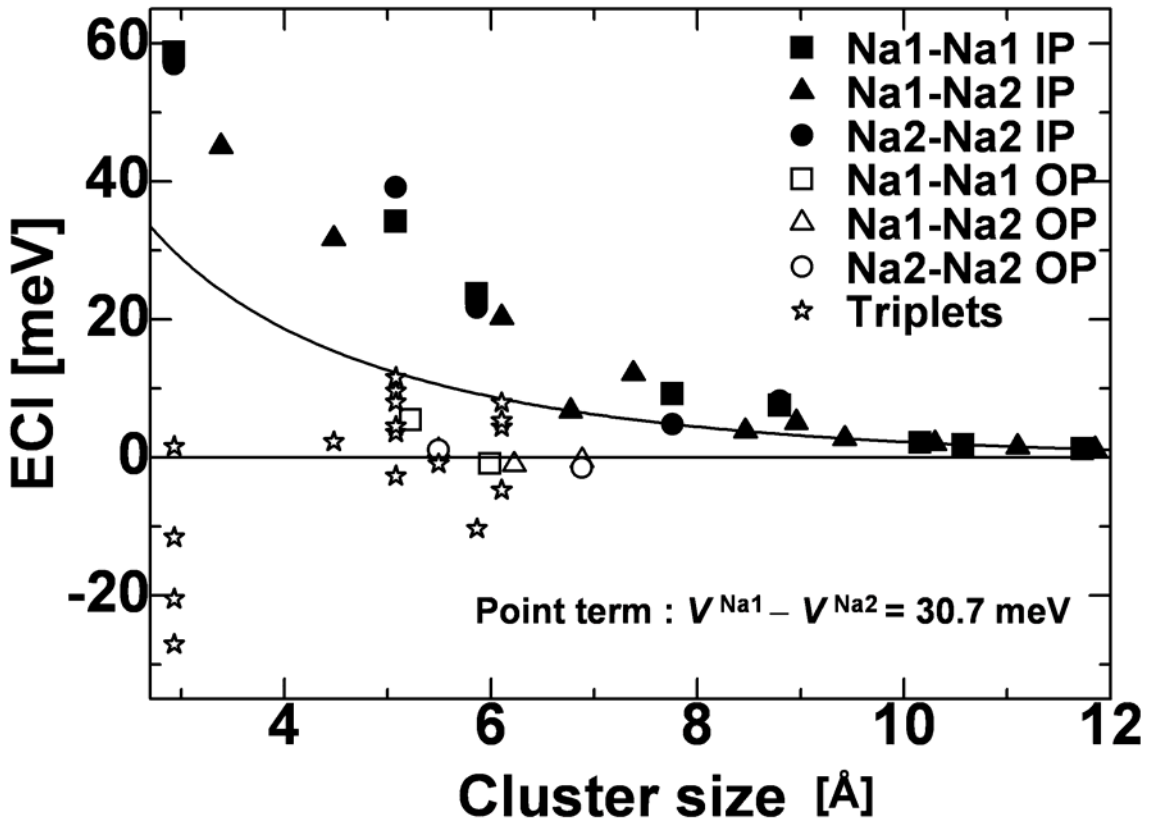

Figure 4-5. Pair ECI for the GGA cluster expansion. Although all clusters are not shown, the non-zero background shown as the curve $V'_{ij} = 12\frac{erfc(0.095r_{ij})}{0.095r_{ij}}$ is applied to in-plane pair clusters up to 18Å (the Na1-Na1 NN cluster distance is 2.93Å). The ECI shown are the sum of the background ECIs and the fitted ECIs. IP: in-plane, OP: out of plane.

Table 4-1. Effective Cluster Interactions (ECI) per meV in the cluster expansion for the GGA.

Points	
Cluster	**ECI**
1	939.65
2	908.94

Pairs (excluding clusters with background contribution only)					
Na1-Na1		**Na1-Na2**		**Na2-Na2**	
Cluster	**ECI**	**Cluster**	**ECI**	**Cluster**	**ECI**
3	58.72	8	250.00	14	56.99
4	34.20	9	45.09	15	39.15
5	23.73	10	31.72	16	21.75
6	9.21	11	20.31	17	8.25
7	7.56	12	2.16		
		13	5.09		
18	5.45	20	1.03	23	1.12
19	–0.88	21	–1.03	24	–1.46
		22	–0.43		

Triplets					
Cluster	**ECI**	**Cluster**	**ECI**	**Cluster**	**ECI**
25	–20.48	31	–2.67	37	–10.31
26	–11.56	32	11.60	38	5.35
27	–11.56	33	3.63	39	4.41
28	–27.02	34	4.56	40	–4.69
29	2.32	35	8.04	41	7.94
30	9.59	36	–0.89		

4.4.1.3 Phase Diagram

Figure 4-6 shows the phase diagram obtained with the GGA cluster expansion. The in-plane ordering of the ground states at x = 0.5, 0.6, 0.67, 0.71, 0.77 and 0.81 are those shown in Figure 4-3. Somewhat surprisingly, all the ordered phases are line compounds, which tolerate very little off-stoichiometry. The phase transition temperatures were obtained by free energy integration. The transition temperatures shown as dotted lines in the phase diagram in Figure 4-6 are a lower bound.

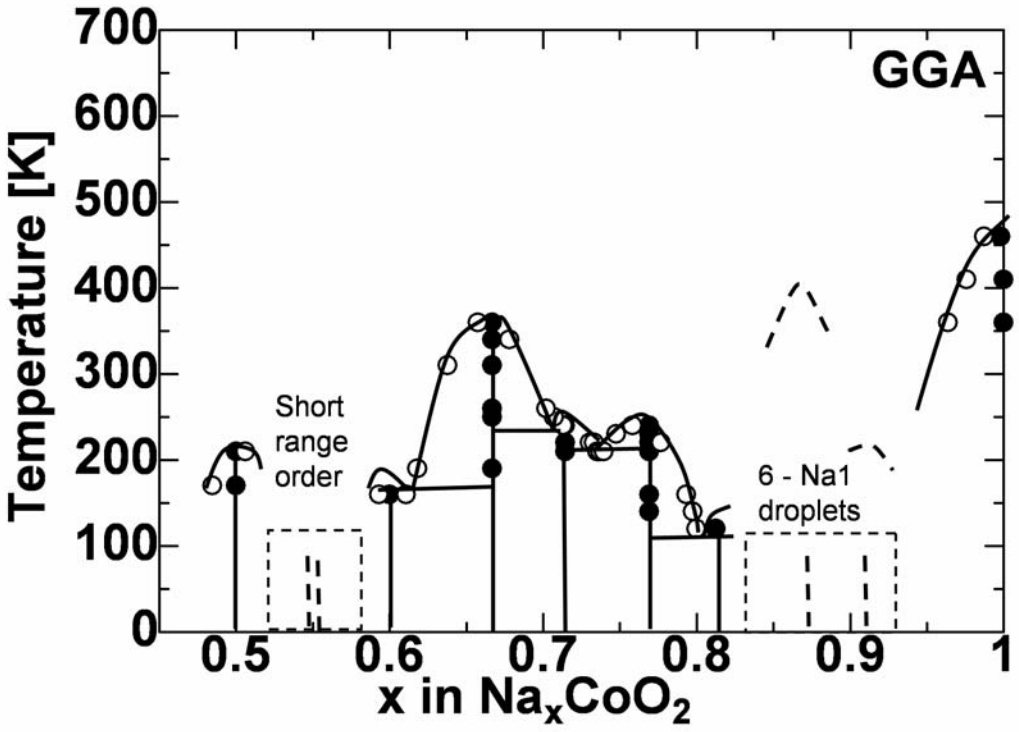

Figure 4-6. GGA phase diagram obtained by Monte Carlo simulation from the cluster expansion in Table 4-1.

Monte Carlo cooling simulations suggest short-range ordered structures with lower energy than the two-phase coexistence between known ordered patterns at $x = 0.5$, 0.56 (5/9) and 0.6 in the region $0.5 < x < 0.6$. One example of such a short-range ordered structure is shown in Figure 4-7, which consists of a snapshot of a Monte Carlo cooling simulation at 100K and $x \sim 0.56$. We could not identify any regular pattern in these simulations. The energy of the first principles ground state at $x = 0.56$ monotonically increases during heating until $T \sim 230$K, above which the energy decreases and the structure disorders. In principle, the energy cannot decrease with temperature along an equilibrium path, thus further indicating that a lower energy configuration, other than the one we identified, must exist. Detailed discussion of the short-range ordered structures is given later in section 4.5.1. For compositions $0.6 \leq x \leq 0.81$, the only ordered phase that persists to room temperature (300K) is $x = 0.67$. Ground states have six-Na1 droplet motifs (*24, 27*) analogous to the three-Na1 droplet motifs in Figure 4-3 within the composition range $0.85 < x < 1$. These six-Na1 droplet motifs are predicted to be ground states using the cluster expansion, however we were unable to obtain a structure with six-Na1 droplet motifs as a ground state in first principles calculations, possibly due to the fact that the optimum stacking of the in-plane ordered Na layers along the c_{hex} axis was not identified.

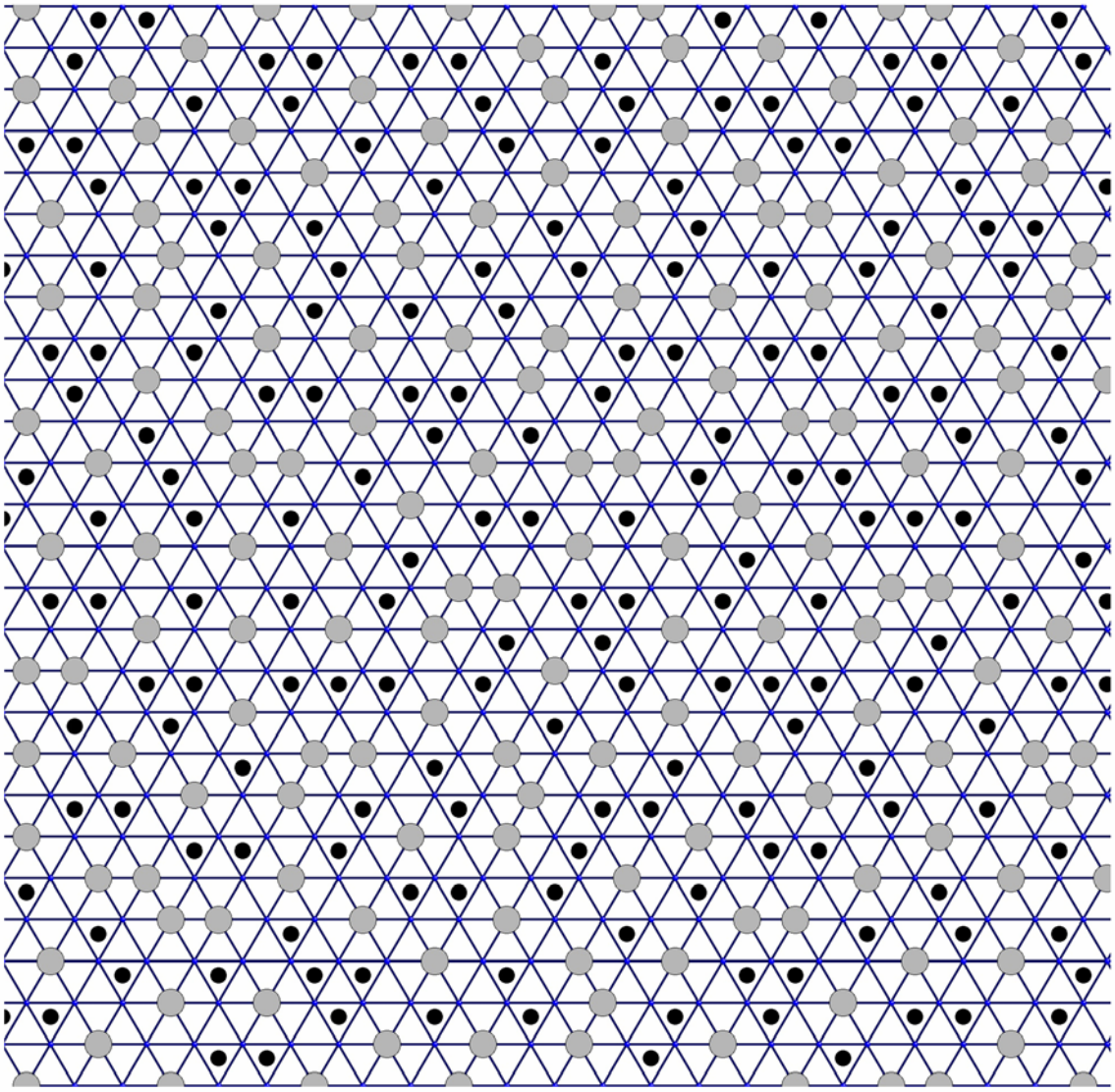

Figure 4-7. Snapshot of a Na layer in a Monte Carlo cooling simulation at 100K, concentration $x \sim 0.56$, GGA approximation. Legend: Gray circles: Na1, black circles: Na2.

Figure 4-8a shows the Na concentration, Na1/Na2 ratio, and Na1 order parameter in a Monte Carlo simulation where the system is heated at fixed chemical potential corresponding to $x \sim 0.5$. The Na concentration does not change much with temperature, however the Na1/Na2 ratio drops sharply at around 300K. The "order parameter" is a

measure of disorder, and 1 signifies a fully ordered structure while 0 denotes a fully disordered structure. Na1 sites are split into α and β sites for $Na_{0.5}CoO_2$. Figure 4-3b shows the positions of α and β sites within this compound. Na1 (large gray circles in Figure 4-3b) may occupy α sites, but not β sites, at 0K. By defining the concentration of Na1 on α and β sites as c_α and c_β respectively, the concentration of Na1 on α sites in the fully ordered state is $c_{\alpha 0} = 0.5$, while the concentration of Na1 on β sites in the fully ordered state is $c_{\beta 0} = 0$, and the order parameter is given by:

$$\frac{c_\alpha - c_\beta}{c_{\alpha 0} - c_{\beta 0}} = 2\left(c_\alpha - c_\beta\right). \tag{4.10}$$

The order parameter drops from approximately 1 to around 0 at about 300K in Figure 4-8a, exactly where the change in Na1/Na2 ratio is observed. It is clear from the snapshot of a Na layer at 320K, shown in Figure 4-8b, that the Na arrangement is disordered at this temperature.

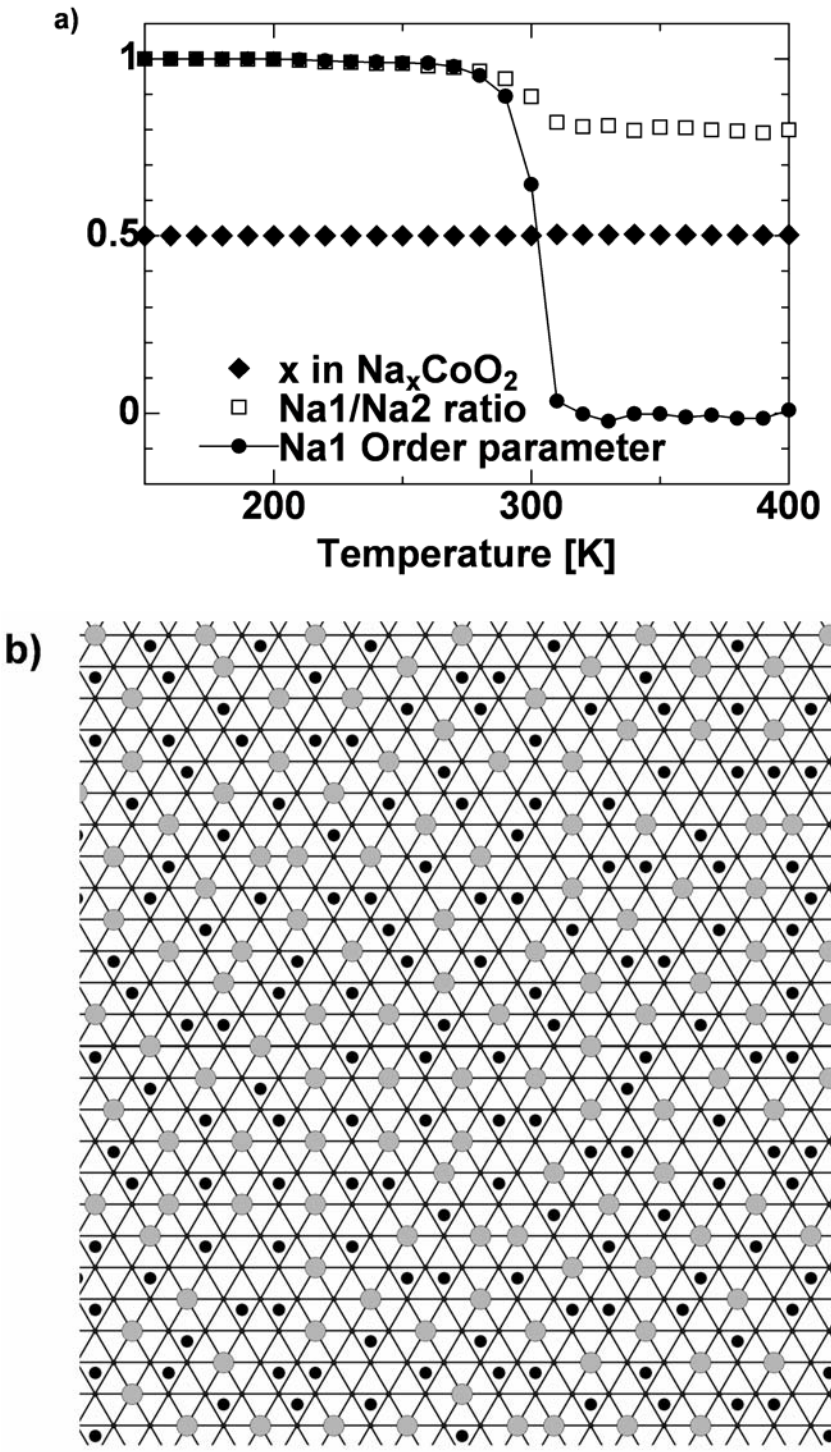

Figure 4-8. (a) Na concentration, Na1/Na2 ratio and Na1 order parameter for a Monte Carlo heating simulation near $x = 0.5$ (GGA approximation). (b) Snapshot of a Monte Carlo cell at 320K, after transition. Legend: Gray circles: Na1, black circles: Na2.

The order-disorder temperature in the heating simulation of Figure 4-8a is approximately 300K, higher than the 220K shown in the phase diagram in Figure 4-6. This difference reflects the strong first order character of the transition. Phase transitions desired for Monte Carlo simulations require that intermediate states between old and new states are accessible. If the energy levels of the intermediate states are high, then increased temperature is necessary to bring the system from the metastable state to the stable state. There are no low-energy excitations accessible to bring the system to the disordered state in perfectly ordered states at higher Na concentrations, such as above $x \geq 0.5$. The system can disorder only by first making space through removing some Na, and then filling back the space by adding Na. The high energy required to overcome this excitation step is feasible only at elevated temperatures compared to the true transition temperature.

The change in phase transition temperature when the formation energy of the ground state is shifted by 1meV/FU is also calculated to obtain a sense of the reliability of the computed transition temperatures. This energy is added/subtracted to the ground state energy, but no change is made to the ECI. As a result, a lower/higher transition entropy is required at the transition. The extent of change can characterize the effect of inaccuracy in the cluster expansion on the phase transition temperature. The sensitivity, or change in phase transition temperature, with +1meV shift in ground state energy ($\Delta T_c / \Delta E_{shift}$) for major phases were –70K, –40K, –40K, and –70K at x = 0.5, 0.67, 0.77

and 0.87 (six-Na1 droplet) respectively. In general, transition temperatures are more reliable for high transition temperatures because the free energy drops more steeply with change in temperature, however the transition temperature for six-Na1 droplet phases are less reliable compared to those of $x \sim 0.67$ and 0.77.

Note that if the ordered structures are line-compounds, then the shift in transition temperature can be estimated from the entropy of the disordered state:

$$\Delta T_c = \Delta E_{shift} / S_{disorder} \,. \tag{4.11}$$

The large shift (ΔT_c) in the transition temperature (T_c) with a small shift in formation energy (ΔE_{shift}) implies small entropies in the disordered states ($S_{disorder}$). One reason is that the restriction of Na1-Na2 NN simultaneous occupancy severely limits the number of possible Na ordering patterns, therefore the Na layer is not totally disordered and the entropy of the "disorder" phase is decreased.

4.4.2 GGA+U

4.4.2.1 Formation energies and ground states

Figure 4-9a shows the GGA+U formation energy per FU. In contrast to the GGA result, the number of ground states obtained with the GGA+U approximation is very small (five including the two end members), although calculations have been conducted at 14 concentrations. The dotted line in Figure 4-9a shows the convex hull when

O3-$NaCoO_2$ (shown with the gray diamond) is considered as an end member. The GGA+U energy of O3-$NaCoO_2$ is 44 meV/FU lower than that of P2-$NaCoO_2$.

Figures 4-9b-e shows the ground state structures at x = 0.5 (= 2/4, Figure 4-9b), 0.6 (= 3/5, Figure 4-9c), 0.67 (= 4/6, Figure 4-9d) and 0.75 (= 9/12, Figure 4-9e). The Na layer ordering patterns for x = 0.5 and 0.67 is the same as these in the GGA calculations, however at x = 0.75 the droplet ordering found in GGA+U is not a ground state in GGA. The stacking in the c-axis direction is such that Na1 between adjacent layers are positioned as far away from each other as possible and Co^{4+} stack on top of each other for each ground state.

Strong ground states occur only at concentrations where the Co ordering pattern is commensurate with the symmetry of the Na lattice (*27*). Co orders with a supercell of $a_{hex} \times \sqrt{3}a_{hex}$, $\sqrt{3}a_{hex} \times \sqrt{3}a_{hex}$, and $2a_{hex} \times 2a_{hex}$ at x = 0.5, 0.67, and 0.75 respectively. The Na layer ordering for these structures is $2a_{hex} \times \sqrt{3}a_{hex}$, $2\sqrt{3}a_{hex} \times 2\sqrt{3}a_{hex}$ and $2\sqrt{3}a_{hex} \times 2\sqrt{3}a_{hex}$ respectively.

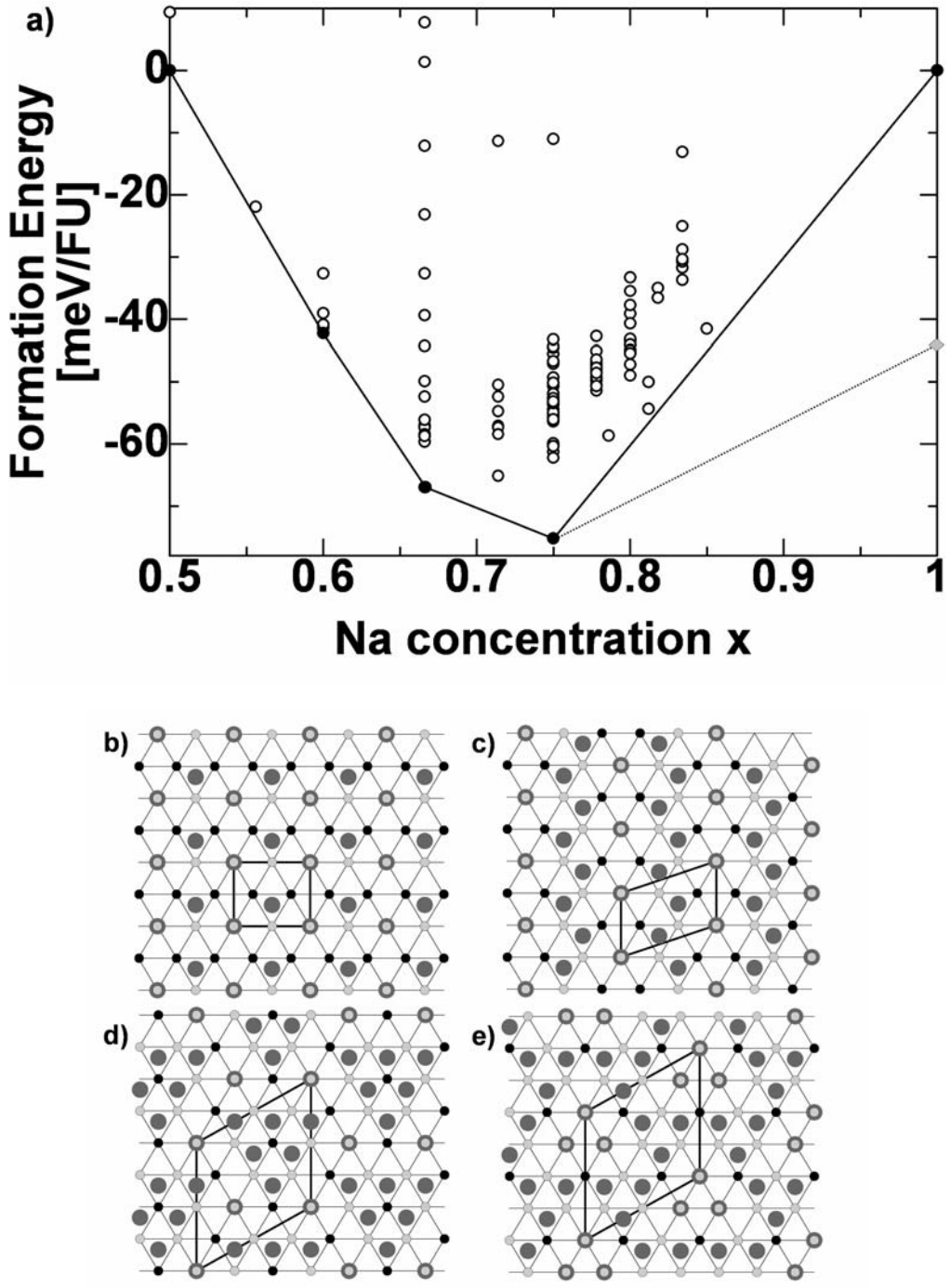

Figure 4-9. (a) First principles GGA+U formation energy per formula unit. The bold solid line shows the convex hull. The convex hull changes to the dotted line when formation of O3-$NaCoO_2$ (gray diamond) is allowed. (b-e) Ground states of first principles GGA+U formation energy at x = (b) 0.5, (c) 0.6, (d) 0.67 (2/3) and (e) 0.75. Legend: Large dark gray circles: Na, small light gray circles: Co^{3+}, small black circles: Co^{4+}. Na1 sites are small light gray circles superimposed on dark gray circles.

4.4.2.2 Cluster Expansion

Figure 4-10 shows the clusters included in the GGA+U cluster expansion. The empty circles at the intersections of the lines correspond to Na1 sites and the empty circles inside triangles represent Na2 sites as in the GGA while the filled circles correspond to Co sites. The weighted CV score of this cluster expansion was 9.33 meV/FU and the RMS error was 3.12 meV/FU. In-plane ordering of cluster expansion ground state structures matches the ordering of ground states within the structures calculated by first principles. Figure 4-11 shows the ECI for the GGA+U cluster expansion, in which the Na1-Na2 NN and Na1-Co^{4+} NN simultaneous occupancy penalties have been added. The Na-Co ECI in the Figure 4-11 have been multiplied by –1 to show interactions between more electrostatically repulsive species with a positive value. The Co NN pair is the strongest interaction, being almost four times higher in magnitude than the second strongest pair interaction. The strength of the Co NN interaction causes ground states in Figure 4-9 to all have a well-ordered Co^{3+}/Co^{4+} layer (x = 0.67 with $\sqrt{3}a_{hex} \times \sqrt{3}a_{hex}$ ordering, x = 0.75 with $2a_{hex} \times 2a_{hex}$ ordering). The values utilized for the ECI are shown in Table 4-2 and it should be noted that these values correspond to the numbers in Figure 4-10. Contrary to the GGA, insight on the Na1 and Na2 site energy difference cannot be obtained from the ECI in Table 4-2 because the magnitude of the Na1-Co^{4+} NN penalty affects the Na2 point term ECI. It could be argued that the Co interactions are represented too strongly in the cluster expansion, as a

consequence of a too large U value. Though U = 5eV per Co gives the right average electrochemical potential between $0.5 \leq x \leq 0.8$ (*8*) (details in section 4.5.3.2.1), however it may not be the optimum value of U for modeling the partial charge localization that is often observed in this material. Therefore our phase diagram results can be taken as a representation of the extreme scenario of complete charge localization.

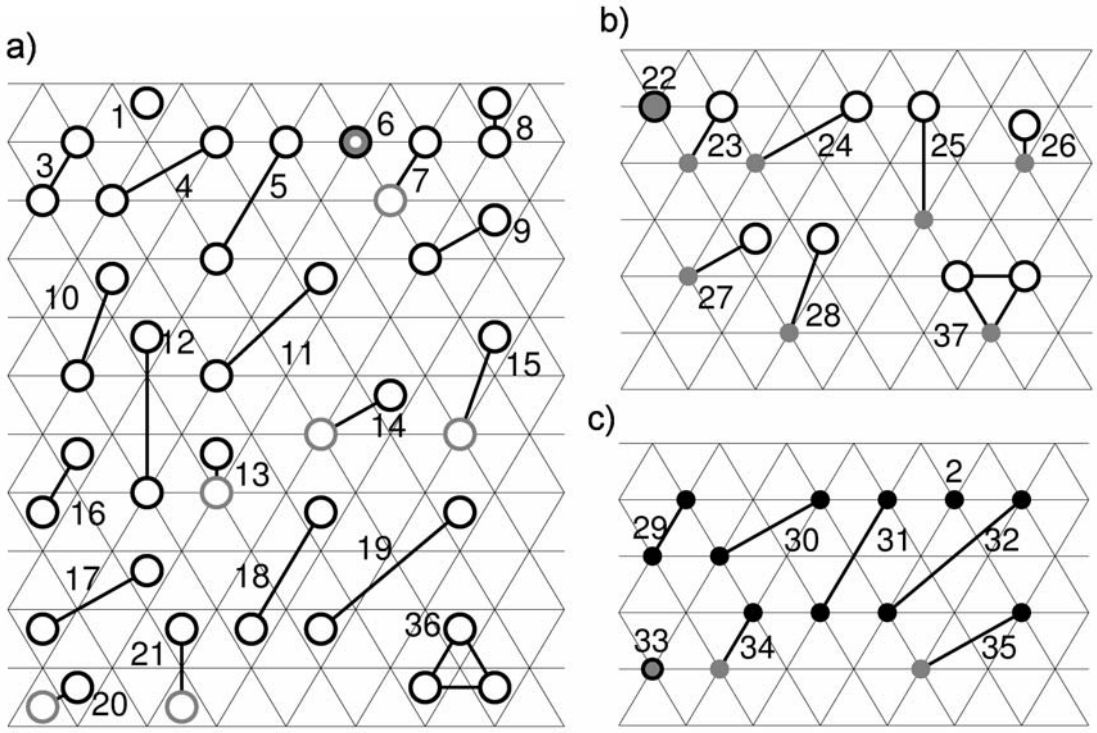

Figure 4-10. Clusters included in the GGA+U cluster expansion. (a) Clusters of Na layer sites. (b) Clusters including both Na layer and Co layer sites. (c) Clusters of Co layer sites. The empty circles at the intersections of the lines correspond to Na1 sites, and empty circles inside triangles represent Na2 sites. Filled circles correspond to Co sites. Circles in black correspond to sites in one layer, and circles in gray represent sites in an adjacent layer.

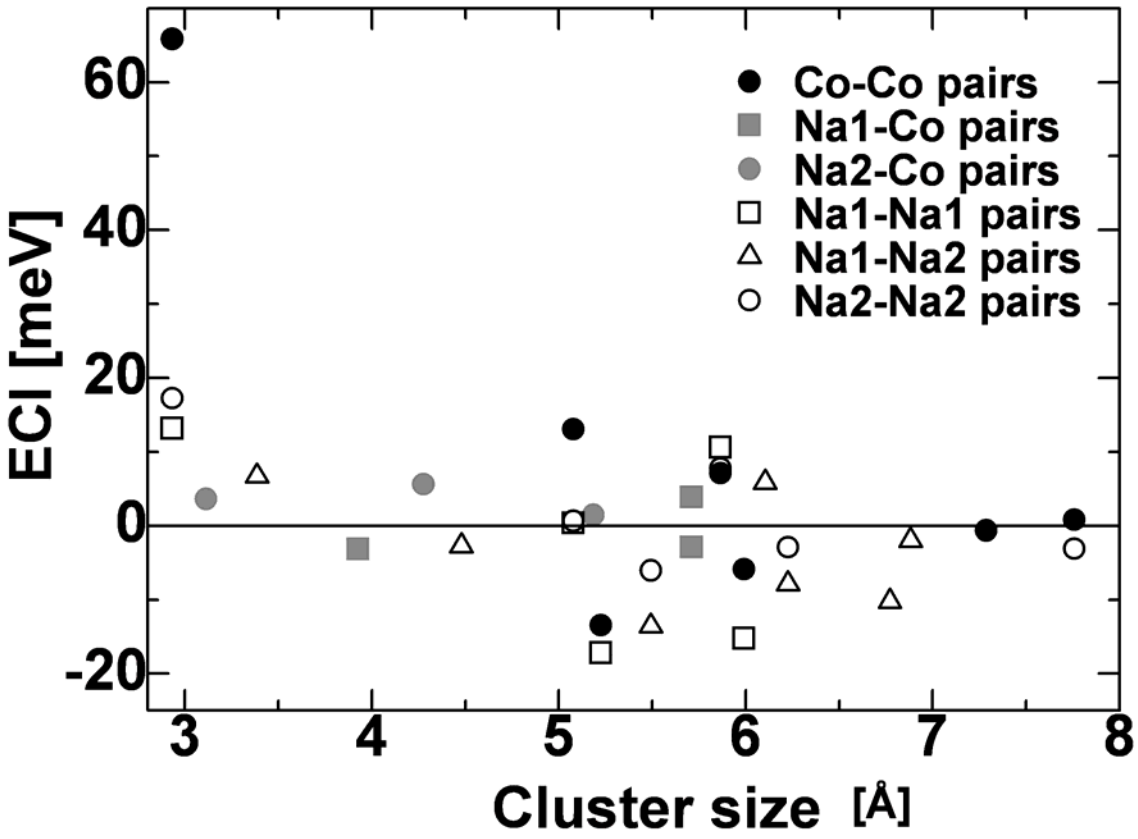

Figure 4-11. Pair and triplet ECI for the GGA+U cluster expansion. The Na-Co ECI have been multiplied by −1 to show interactions between more electrostatically repulsive species with a positive value.

Table 4-2. Effective Cluster Interactions (ECI) per meV for the cluster expansion in the GGA+U.

Points	
Cluster	**ECI**
1	–154.40
2	324.55

Pairs					
Na1-Na1		Na1-Na2		Na2-Na2	
Cluster	**ECI**	**Cluster**	**ECI**	**Cluster**	**ECI**
3	13.17	8	250.00	16	17.28
4	0.36	9	6.73	17	0.65
5	10.60	10	–2.70	18	7.77
6	–17.19	11	5.88	19	–3.08
7	–15.24	12	–10.23	20	–6.04
		13	–13.58	21	–2.89
		14	–7.87		
		15	–1.96		

Pairs					
Na1-Co		Na2-Co		Co-Co	
Cluster	**ECI**	**Cluster**	**ECI**	**Cluster**	**ECI**
22	–100.00	26	–3.64	29	65.86
23	3.17	27	–5.64	30	13.09
24	2.89	28	–1.48	31	7.11
25	–3.89			32	0.82
				33	–13.42
				34	–5.88
				35	–0.62

Triplets	
Cluster	**ECI**
36	–18.98
37	–2.64

4.4.2.3 Phase diagram

Figure 4-12 shows the phase diagram obtained from the GGA+U cluster expansion. The ground states at x = 0.5, 0.67 (2/3), and 0.75 are shown in Figures 4-9b, 4-9d, and 4-9e respectively. The order-disorder temperatures are typically higher than those in the GGA phase diagram, and the three ordered states are all stable at room temperature. The Monte Carlo simulations again suggest structures with short range order in the region $0.5 < x < 0.67$ that have lower energy than phase coexistence between known ordered patterns at x = 0.5, 0.6 and 0.67. We could not identify any regular ordering patterns at zero Kelvin, closely resembling the short-range order region in the GGA result. There are two order-disorder transitions at x = 0.67. The Na layer initially disorders at approximately 370K, followed by charge disorder in the Co layer at about 670K. Contrary to the GGA phase diagram in Figure 4-6, the six-Na1 droplet patterns are not stable in GGA+U because there is no high symmetry Co^{3+}/Co^{4+} ordering pattern commensurate with the six-Na1 droplet pattern. Instead there is a strong eutectic where the disordered phase is stable down to ~30K near $x \sim 0.86$.

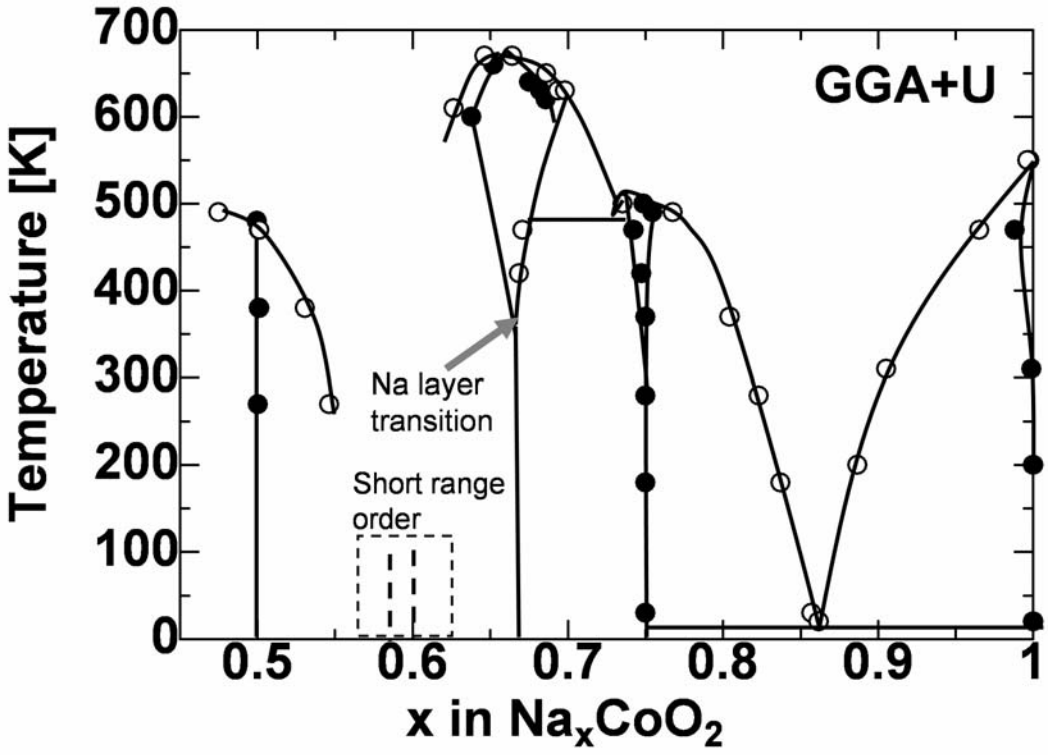

Figure 4-12. GGA+U phase diagram obtained by Monte Carlo simulation from the cluster expansion in Table 4-2.

4.5. Discussion

4.5.1 GGA phase diagram

Ground state structures are found at x = 0.5, 0.6, 0.67, 0.71, 0.77, and 0.81 in the GGA. In addition, the Monte Carlo simulations indicate that other structures are likely to be present around x = 0.56 though we could not identify these structures. In general, the lowest energy stacking is the one with the minimum amount of short adjacent-plane Na1-Na1 neighbors. This manner of stacking often reduces the symmetry of the unit cell.

For example, both the ground state structure of $Na_{0.67}CoO_2$ and structures with three-Na1 droplet motifs display that stacking destroys the in-plane three-fold rotation symmetry. while mirror symmetry perpendicular to the Na layers is retained in stronger ground states such as $Na_{0.50}CoO_2$ and $Na_{0.67}CoO_2$.

The following information can be deduced from comparison of the ground states with available experimental information: Clear evidence exists for the presence of a stable ordered state at x = 0.5 both experimentally (*16, 18*) and from computational suggestions (*24, 25*). A structural transition at x = 0.5 is observed experimentally at 210K (*34*), which is close to our GGA transition temperature at 220K.

The low temperature electron diffraction conducted by Zandbergen et al. shows no superstructure at x = 0.56 (*21*), however a few crystals display the diffraction pattern indicative of the x = 0.5 compound (*21*). This is in fair agreement with our calculations, where some x = 0.5 ground state motifs is seen in Figure 4-7. The Warren-Cowley short range order parameters (*59*) of the three shortest Na1-Na1 and Na2-Na2 bonds were calculated and summarized in Table 4-3 in order to understand the origin of the structures observed in the Monte Carlo cooling simulation between $0.5 < x < 0.6$. Included are values for the x = 0.56 first principles ground state (Figure 4-3c), a short-range ordered structure from Monte Carlo simulation (Figure 4-7, T = 100K), and a disordered structure from Monte Carlo simulation (T = 650K). The Warren-Cowley parameter (α_n) is defined

for the *n*th nearest neighbor on a binary sublattice with species A and B as:

$$\alpha_n = 1 - \frac{p_{AB}^{n}}{p_{AB}^{rand}}. \qquad (4.12)$$

Warren-Cowley parameters are calculated on both the Na1/vacancy and the Na2/vacancy sublattice. The two species, A and B, are chosen as Na1 and vacancies in the Na1 sublattice, or Na2 and vacancies in the Na2 sublattice. Here, p^{n}_{AB} is the probability of A-B (Na1-vacancy or Na2-vacancy in this work) pairs with *n*th nearest neighbor distance in the system in consideration, and $p_{AB}^{rand} = c_A c_B$ is the probability of A-B pairs if A and B were randomly distributed (*60*). The Warren-Cowley parameter is > 0 when the two species have an ordering tendency, < 0 when the species have a phase separating tendency, and 0 when fully random. In this paper, the two species are chosen as Na1 and vacancies in the Na1 sublattice, or Na2 and vacancies in the Na2 sublattice.

Table 4-3. The Warren-Cowley short-range order parameters (*59*) for competing phases at x ~ 0.56. The Warren-Cowley parameter is > 0 when the Na and vacancies have a phase separating tendency, < 0 when there is a phase separating tendency, and 0 when fully random. NN: nearest neighbor bond, FPGS: first principles ground state, SRO: short range order structure: DIS: disordered structure.

Bond type	**Na1-Na1 NN**	**Na2-Na2 NN**	**Na1-Na1 2nd NN**	**Na2-Na2 2nd NN**	**Na1-Na1 3rd NN**	**Na2-Na2 3rd NN**
FPGS	**-0.286**	**-0.167**	**0.143**	**0.000**	**-0.071**	**-0.167**
SRO	**-0.216**	**-0.172**	**0.000**	**-0.121**	**0.003**	**0.038**
DIS	**-0.130**	**-0.113**	**-0.028**	**-0.082**	**-0.035**	**-0.036**

It is clear from these Warren-Cowley parameters that the Monte Carlo simulation at 100K is not simply in a state between the ordered ground state and the random solution. While the NN Na1-Na1 Warren-Cowley parameter indicates lower order than the ground state, the NN and 2nd NN Na2-Na2 Warren-Cowley parameters indicate stronger ordering than in the ground state. This would indicate that there might be a lower energy ground state possible.

The ground state for $x = 0.6$ is the state predicted by previous computational work (*24, 25*), however this ground state has not been observed experimentally.

The electron diffraction results by Zandbergen et al. (*21*) for $Na_{0.64}CoO_2$ show no superstructure, but this does not contradict our result. Depending on the exact composition of the phase boundaries and the sample, our phase diagram (Figure 4-6) shows a two-phase region with mostly a disordered phase and possibly a small amount of $x = 0.67$ compound for $Na_{0.64}CoO_2$ at room temperature,

New ground states are found at 0.67 (2/3) and 0.714 (5/7), which exhibit a larger unit cell than thought in previous computational work (*24, 25*), perhaps the ground state ordering pattern was overlooked in those studies. We are not aware of experimental papers suggesting our ground state ordering patterns. Chou et al. (*61*) suggest a ground state at $x = 0.708$ (17/24) with $2\sqrt{3}a_{hex} \times 2\sqrt{3}a_{hex}$ ordering that has 3-Na1 droplet motifs

with trivacancies (Na concentration x = 9/12) in half of the layers and 3-Na1 droplet motifs with quadrivacancies (Na concentration x = 8/12) in the other half of the layers. However the GGA energy of that structure is 15meV/FU higher than two-phase coexistence of our x = 0.67 and 0.714 ground states.

Contrary to previous computational work (*24, 25*), no ground state is observed in the GGA approximation at x = 0.75, and the lowest energy state at this composition is two phase coexistence between x = 0.71 and 0.77. This is in excellent agreement with neutron diffraction results on powdered crystals by Huang et al. (*18*). Electron diffraction at low temperature by Zandbergen et al. (*21*) suggests a complicated and weak superstructure at x = 0.75, but it should be noted that the superstructure pattern was quickly modified by the electron beam during experiment. Therefore it is plausible that no stable ordering patterns exist at x = 0.75. During resistivity measurements two transitions are experimentally observed for the x = 0.75 system at around 285K and 315K (*20*). We also see two transitions for this Na concentration in the GGA phase diagram: a eutectic transition around 200K, and an order-disorder transition around 230K. Although the calculated temperatures are lower than what is observed, the temperature difference between the two transitions is strikingly similar. Hence, the simulation results may explain these transitions as two consecutive first order transitions towards the disordered state.

At the high concentration end we find the three-droplet phases first suggested by Roger et al. (*20*) and also identified in previous computational work (*24, 27*). The stacking in the *c*-axis direction is such that Na1 between adjacent layers are positioned as far away from each other as possible. Although ground states of the three-Na1 motifs seem to appear at random compositions, but in fact such ground states appear only at compositions $x = \frac{N-3}{N}$ where *N* is an integer and the unit cell has $\sqrt{N}a_{hex} \times \sqrt{N}a_{hex}$ ordering in-plane. The only exception is *x* = 13/16, where the structure with $4a_{hex} \times 4a_{hex}$ ordering has 1.6meV/FU higher energy than the ground state with $4a_{hex} \times \sqrt{13}a_{hex}$ ordering. This fact implies that in principle three-Na1 droplet motifs want to spread apart as far away as possible from each other without destroying the in-plane three-fold rotation symmetry. The four ground states shown in Figures 2g-j are part of an infinite series of ground states with $\sqrt{N}a_{hex} \times \sqrt{N}a_{hex}$ ordering in-plane, so it is possible that more ground states with 3-Na1 motifs may exist.

Six-Na1 droplets, although suggested computationally as ground states (*24, 27*), have not been observed experimentally. However, structures with six-Na1 droplets that was stable compared to phase separation between the three-Na1 droplet phase with P2 stacking at *x* = 0.86 and P2-$NaCoO_2$ were not found in first principles calculations. Furthermore, the six-Na1 droplet motifs would become metastable with regard to this two-phase formation if two phase formation between P2 three-Na1 droplet phase and O3-$NaCoO_2$ is allowed.

4.5.2 GGA+U phase diagram

We find ground state structures at x = 0.5, 0.67 and 0.75 in the GGA+U derived phase diagram, however additional stable structures are likely present around x = 0.60 though these structures could not be identified. The Na layer ordering patterns of x = 0.5 and 0.67 ground states are the same as in the GGA phase diagram. The 0.75 ground state, with three-Na1 droplet motifs, is the ordering proposed by Roger et al. (*20*), and did not appear in the GGA phase diagram. Figure 4-13 shows a snapshot of the Na layer from a Monte Carlo cooling simulation at 430K and composition $x \sim 0.76$. We also observe connected three-Na1 droplet motifs other than the x = 0.75 ground state patterns. The connected three-Na1 droplet motifs and Na2 show the "stripe" pattern proposed by Geck et al. (*22*) based on observations with high-energy XRD near x = 0.75. The concentration range $0.75 \leq x \leq 0.82$ is exactly where partial charge localization is experimentally observed (*30-33*).

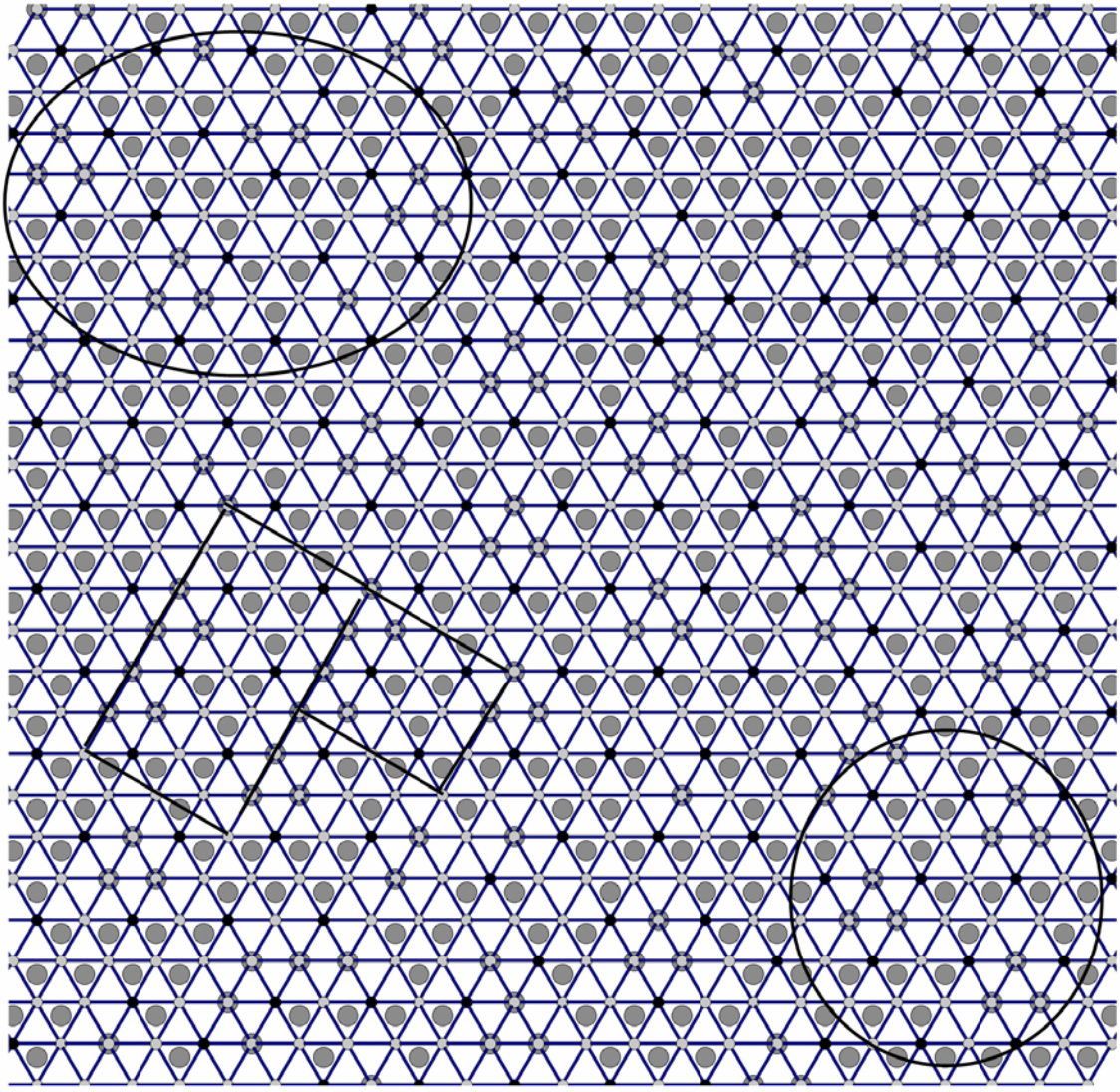

Figure 4-13. Snapshot of a Monte Carlo cooling simulation at 430K, concentration $x \sim 0.76$, GGA+U approximation. The "stripe" motif proposed by Geck et al. (*22*) (shown in rectangles) and the ground state motif for $x = 0.75$ (circled) are visible. Legend: Large dark gray circles: Na, small light gray circles: Co^{3+}, small black circles: Co^{4+}. Na1 sites are small light gray circles superimposed on dark gray circles.

There are very few stable ordered structures in the GGA+U phase diagram because charge localization to Co^{3+} and Co^{4+} is "complete", causing the dominant interactions to be between Co. Furthermore, ground states must have stable Na layer

ordering that is commensurate with the Co layer ordering, so that there is no Na1-Co^{4+} NN simultaneous occupancy. Only partial charge localization has been experimentally observed, therefore interactions between Co are expected to be weaker than observed with GGA+U approximation. Weaker interactions would allow more Co layer disorder to occur at lower temperature, so real Co layer order-disorder transition temperatures should be lower than those in the theoretical phase diagram. In fact, the calculated transition temperature at $x = 0.75$ is substantially overestimated in comparison with measurements by Roger et al. (*20*).

4.5.3 Comparison of GGA and GGA+U

4.5.3.1 Interactions

The GGA and GGA+U phase diagrams are considerably different, only at $x = 0.5$ and $x = 0.67$ do they give the same ground states. Additionally, the transition temperatures in the GGA+U phase diagram are considerably higher than in the GGA diagram. This difference between the results from the two electronic structure approximations should not be surprising. The mixed valence on Co is metallic and delocalized in GGA such that only interactions between Na^+ exist. The Na^+-Na^+ repulsion is strongly screened by the charge in the hybridized Co-O orbitals leading to weak effective interactions and low order-disorder transition temperatures. This situation is reminiscent of the related compound Li_xCoO_2 in which similar strong screening of the Li^+

by a Co-O rehybridization (*62-64*) also leads to rather low order-disorder transition temperatures (*65*).

Application of the GGA+U leads to completely different physics. The value of U is strong enough to cause charge localization and the phase diagram is largely governed by the strong Co^{3+}/Co^{4+} interaction. The Co^{3+}/Co^{4+} effective interaction is much stronger than the Na^{+}-vacancy interaction resulting in maximal separation of Co^{4+} in the ground states shown in Figures 4-9b-e. In addition, there are restrictions on how the Na layers and Co layers can stack because GGA+U imposes the constraint that Na1 and Co^{4+} cannot be adjacent. This results in strong ground states at x = 0.5, 0.67, and 0.75, which are able to retain mirror symmetry perpendicular to Na layers. Alternatively, Na1 have to stack on top of each other to retain mirror symmetry at a composition such as x = 0.6, which is energetically unfavorable and hence there is no ground state.

When two ordered states on different sublattices are coupled they can go through separate or single order-disorder transition. This depends mainly on the symmetry relation between the two sublattices (*66*). Co charge ordering does not break the symmetry on the Na2 sublattice, but reduces the number of available Na1 sites in the ground state structure at x = 0.67. In this case we see a distinct Na disorder transition before the Co charge state disorders. The Na disorder transition temperature at x = 0.67 is almost the same ($T \sim 370$K) as that obtained with GGA, indicating that both descriptions

are somewhat consistent for the Na configurational energy. At all other compositions the Na/vacancy and Co^{3+}/Co^{4+} sublattices disorder simultaneously, reflecting the fact that the Na ordering is determined by the break in symmetry arising from the charge ordering on the Co sublattice.

It is important to understand the limitations of the GGA+U cluster expansion and Monte Carlo simulation at elevated temperature. The Co^{4+} is fully localized and therefore contributes significant configurational-like electronic entropy to the system in our model. If the electronic hole were to delocalize (as in a metal-insulator transition), then this description would become invalid and a metallic Fermi-Dirac like entropy should be used to model the electrons.

4.5.3.2 Comparison to experimental Na potential, lattice parameter, and Na1/Na2 ratio

The Na intercalation voltage, *c* lattice parameter, and Na1/Na2 ratio from our Monte Carlo simulation results are compared with experimental observations to further assess the merits of the GGA and GGA+U methods to this system.

4.5.3.2.1 Na potential

Electrochemical cells have been constructed with a Na_xCoO_2 working electrode to examine Na removal in a controlled manner (*8, 19*). The voltage against an anode is measured as a function of Na^+ concentration in Na_xCoO_2. This represents the Na chemical potential in the material, and can accurately show the concentration at which stable phases exist and their relative energy differences. Plateaus in the voltage curve indicate two-phase regions while slopes are an indication of single phase formation. Figure 4-14a shows the Na intercalation / deintercalation voltage for GGA and GGA+U at 200K and 300K as a function of Na concentration. The computed voltage is the difference between the Na chemical potential at the cathode (Na_xCoO_2) and anode (pure Na), and can be obtained directly from the Monte Carlo simulations. The relatively different shape of the GGA and GGA+U voltage curves is reflective of the different physics in the two approximations. We were not able to point out the exact compositions of the ground states in the GGA above $x > 0.8$, therefore an accurate voltage curve cannot be obtained in this composition range. The GGA voltage curve has a larger average voltage drop of ~1V between $x = 0.5$ and 0.8. There is a stable phase at $x = 0.75$ in GGA+U that is not seen in GGA. Stable phases are observed at $x = 0.71$ and $x = 0.77$ in the GGA voltage curve at 200K, but these features are lost in the GGA 300K voltage curve.

Matching and comparing the experimental and computed voltage curves requires several adjustments. From work on the related Li materials, it is well known that in GGA the redox potential can be underestimated by 0.5 ~ 1V (*45*) due to the spurious self-interaction that the electron sees in the 3*d* orbital of Co. In addition, electrochemical measurements are highly accurate at measuring relative changes in Na content, but they often start with stoichiometry of the compound that is in doubt due to the volatility of Na during synthesis (*39, 40*). Hence, we mainly compare the shape of the computed and experimentally measured voltage curve in Figure 4-14b. The experimental data is from electrochemical measurements at room temperature by Delmas et al. (*8*). The computational data is the GGA voltage curve at 200K, with the voltage shifted upwards by 0.9V. Out of the voltage curves in Figure 4-14a, the GGA 200K curve shown in Figure 4-14b most closely matches the experimental curve in three aspects. First, the magnitude of the voltage drop between $x = 0.5$ and $x = 0.8$ is ~1V. Second, the magnitude of the stable voltage region at $x \sim 0.67$. Third, the existence of several stable phases at $x \sim 0.71$ and 0.77.

Electrochemical studies conducted by Shu et al. (*19*) suggest stable phases at $x = 0.5$, 0.55, 0.71, and 0.75. In addition, susceptibility measurements on samples with $x = 0.55$ are clearly different from those with $x = 0.5$, indicating that these two compositions may be distinct phases (*19*). No stable (or very weak) phase is reported for $x = 0.67$ in Shu et al.'s work (*19*), which is contradictory to previous electrochemical measurements

by Delmas et al. (*8*) that suggested a stable phase close to $x = 0.67$.

It is possible that at $0.7 < x < 0.8$ there is a consistent underestimation of the transition temperatures because stable phases do not exist in the GGA 300K voltage curve. Previous computational phase diagrams based on GGA approximations in Li_xCoO_2 (*65*) and Li_xNiO_2 (*67*) have overpredicted phase transition temperatures. The overestimation is not thought to be due to intrinsic errors of the GGA approximation, but rather to considering too few interactions in the in Li_xCoO_2 (*65*) and Li_xNiO_2 (*67*) cluster expansions, resulting in some overestimated short-range interactions. An alternative possibility considers that no direct Na-Co coupling was treated in the Na_xCoO_2 GGA cluster expansion. The Co sublattice affects interactions on the Na sublattice in Na_xCoO_2 (i.e. high site energies on Na1 sites), but in Li_xCoO_2 and Li_xNiO_2 there is little or no effect on Li from the Co (Ni) sublattice. Another explanation is that temporal Co charge localization occurs in the real system, causing errors in phase transition temperatures, because this is not captured with GGA. Experimental observation of Curie-Weiss behavior implies existence of some extent of charge localization (*19*).

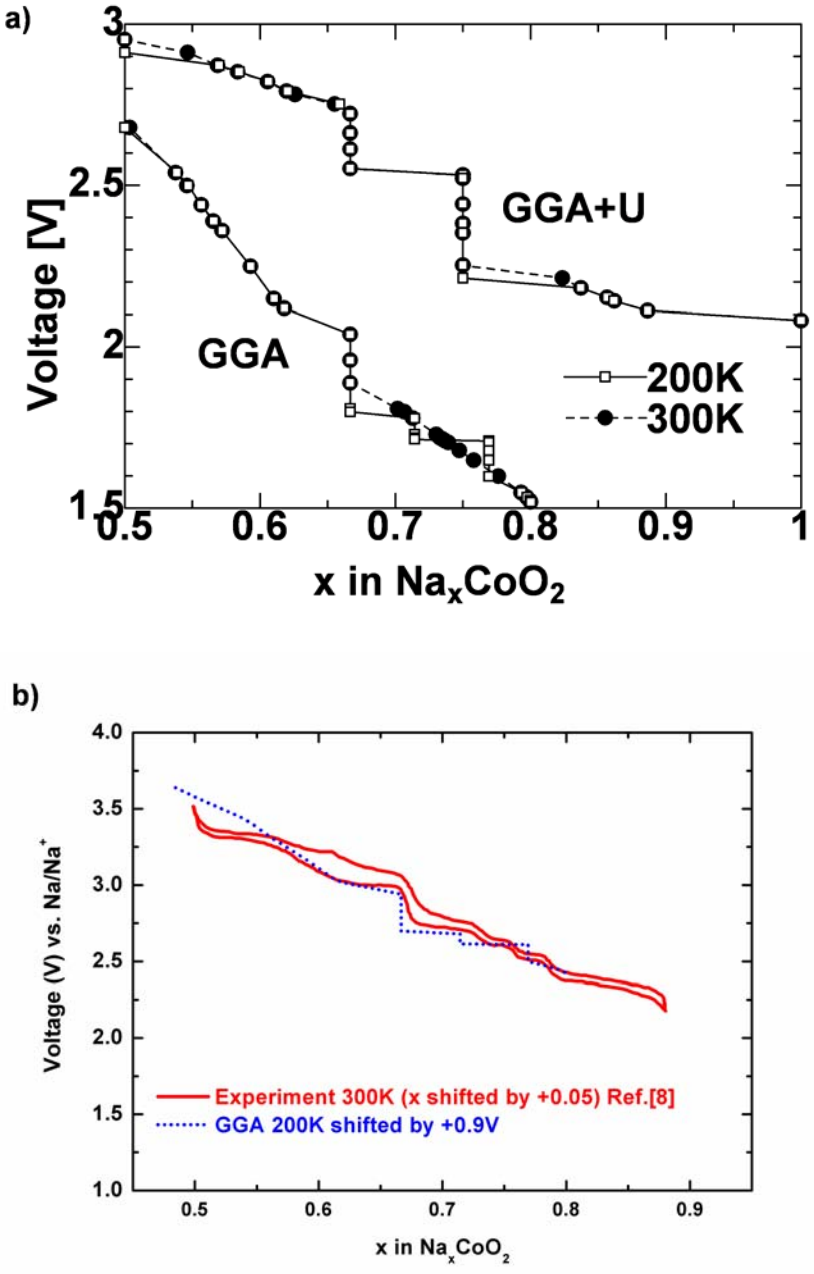

Figure 4-14. (a) Na intercalation / deintercalation voltage of Na_xCoO_2 when used as a cathode against pure Na anode which is derived from Monte Carlo simulations in the GGA and the GGA+U at 200 and 300K. (b) Comparison of experimental electrochemical voltage measurements from Delmas et al. (*8*) at room temperature (bold line) with GGA 200K voltage curve (dotted line). The concentration of the experimental curve is shifted by +0.05, and the voltage of the GGA 200K curve is shifted by +0.9V.

While the GGA+U voltage curves match the absolute average experimental voltage better than GGA, its shape does not reflect experimental information. Observation of the experimentally observed stable phases at $0.7 < x < 0.8$ is inhibited by the $x = 0.75$ stable phase in GGA+U. The stability of the $x = 0.75$ phase in GGA+U results solely from the overestimated strength of Co^{3+}/Co^{4+} interactions in GGA+U, leading to a very stable Co^{3+}/Co^{4+} ordering pattern at $x = 0.75$.

4.5.3.2.2 *c* lattice parameter

The *c* lattice parameter is a good measure of Na concentration because increasing Na concentration in the Na layer is proportional to decreasing space between adjacent oxygen layers. This relation may be used as a simple method of estimating the Na composition from diffraction data. Figure 4-15 compares the *c* lattice parameters of the ground states (Figures 4-3, 4-9) obtained from first principles GGA and GGA+U calculations at zero Kelvin against neutron powder diffraction data of polycrystalline Na_xCoO_2 by Huang et al. (*18*). The GGA *c* lattice parameter matches well with the experimental results for polycrystalline samples (*27*). The GGA *c* lattice parameter is well fit in quadratic form as

$$c = 11.79412 - 1.15505\,x - 0.18785\,x^2. \quad (4.13)$$

The *c* lattice parameter is systematically overestimated in GGA+U.

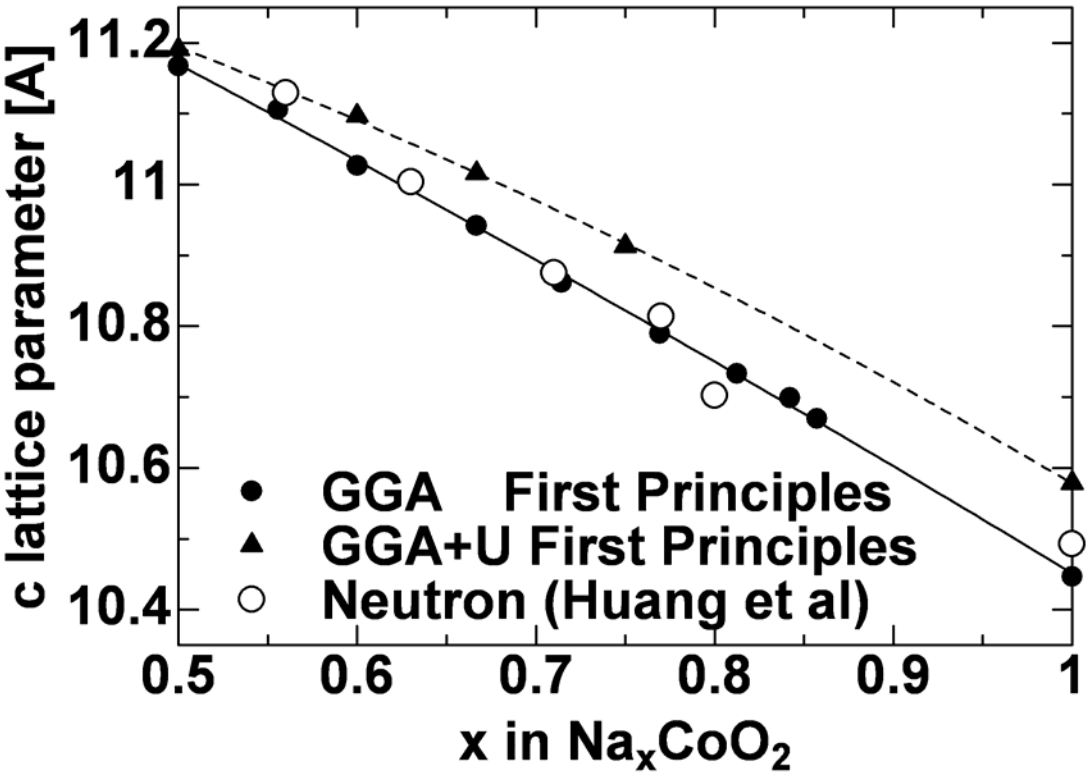

Figure 4-15. *c* lattice parameter as a function of Na concentration computed from GGA and GGA+U first principles calculations at zero Kelvin and from neutron powder diffraction results by Huang et al. (*18*). The lines show a parabolic fit to the calculated *c* lattice parameter values in the GGA and GGA+U approximations.

4.5.3.2.3 Na1/Na2 ratio

The Na1/Na2 ratio is a more detailed measure of the accuracy of our calculations than the *c* lattice parameter because errors in the Na1 and Na2 site energy difference are exposed that are not necessarily accounted for by evaluating the *c* lattice parameter. Figure 4-16 compares the Na1/Na2 ratio from Monte Carlo simulations at 200K and 300K in the GGA, and at 200K in the GGA+U, to values obtained from neutron diffraction (*18, 20, 23, 68, 69*). The Na1/Na2 ratio for GGA at 200K is shown because its corresponding voltage curve better matches with the experimental voltage curve taken at 300K than the GGA voltage profile at 300K. The Na1/Na2 ratio for 200K and 300K almost overlaps in GGA+U, therefore the latter is not shown in Figure 4-16. Huang et al.'s measurements (*18*) at $x \sim 0.56$ and 0.63 are very close to the GGA simulation results at 200K. When $x < 0.7$, the GGA results compare with the experimental Na1/Na2 ratio better; however neither approximation clearly matches the experimentally observed ratio when $x > 0.7$.

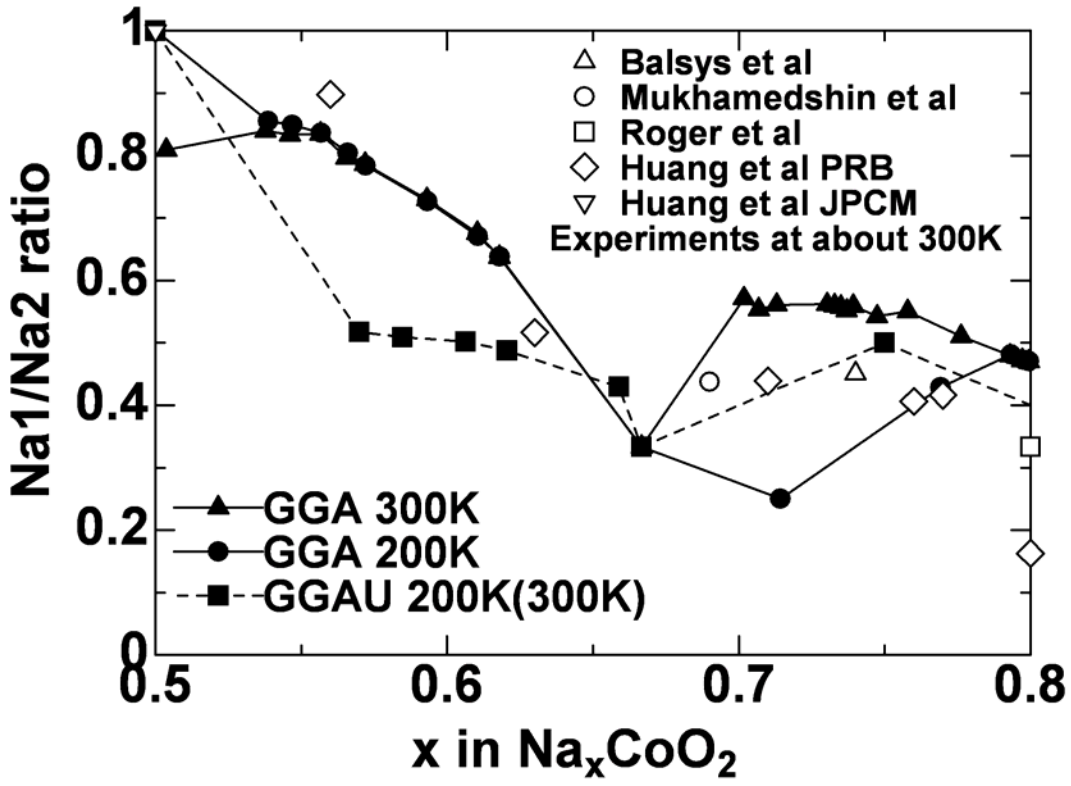

Figure 4-16. Na1/Na2 ratio from Monte Carlo simulations at 200K and 300K in GGA and 200K in GGA+U approximations, and from neutron diffraction results (*18, 20, 23, 68, 69*). Filled symbols show computational results, and open symbols represent experimental results.

4.5.3.3 General comments

At high Na concentrations, the Co^{4+} hole concentration is small and the holes are likely to be localized, leading to charge density variation in the Co layer. Slight charge localization is observed experimentally at $x = 0.75$ (*30-32*) and $x = 0.82$ (*33*), so GGA+U may be a relevant approximation in this case. However, even in this limit GGA+U results do require serious interpretation because it is a static method and dynamic fluctuations

may be needed to properly describe the electronic structure (*62*). Furthermore, the thermodynamically stable state in the high composition range $x > 0.82$ is two-phase separation into P2-Na_xCoO_2 and O3-$NaCoO_2$ (Figures 4-3, 4-9). Whether this occurs may depend on sample preparation and experimental conditions, further complicating a comparison between experiments and computation.

There are more holes in the Co layer of the system at lower Na concentrations, and when $x < 0.8$ the hole concentration is well above the critical concentration at which a Mott transition to a metallic state can occur (*62*). This is what occurs between $x = 0.75$ and $x = 0.95$ in the related system, Li_xCoO_2 (*14, 62*). The Co-Co separation in Na_xCoO_2 is larger because Na^+ is larger than Li^+, so a complete transition to a metallic state may not occur because the orbital overlap between neighboring Co is reduced. This effect is more evident at higher Na (Li) concentration when the Co-Co distance becomes ~2.89Å in O3-$NaCoO_2$ (*70*) and ~2.81Å in O3-$LiCoO_2$ (*71*). The Co-Co distance shortens to approximately 2.81Å when the Na content is reduced from $NaCoO_2$ to P2-$Na_{0.5}CoO_2$ (*16*). Even if the holes have tendency to localize, conductivity measurements indicate that they are mobile and can hop fairly quickly. As a result, the spatial distribution of holes would overlap when time-averaged, and the charge density becomes constant in the Co layer. Therefore, the GGA approximation may be appropriate at lower Na concentrations. Furthermore, the analysis of Na intercalation voltage, *c* lattice parameter, and ground states suggests that between $0.5 \leq x \leq 0.8$, GGA is a better approximation than GGA+U.

4.5.4 Relation to thermoelectricity

When attempting to improve thermoelectric properties, it is reasonable to choose a composition where the disordered phase is favored at low temperature. Disordered phases have low barriers for hole diffusion because holes are not trapped in very stable sites, and are expected to have high electronic entropy that contribute to increased thermopower (*37, 38*).

There exists a disordered phase between $0.75 < x < 0.8$ that is known to be a good thermoelectric material (*11*). Although this is the region where GGA is a good description of the system, it is difficult to analyze whether disorder in the Na layer leads to high *ZT*. Above $x > 0.8$, where charge localization may prevail, $x \sim 0.86$ is possibly a good candidate because the GGA+U phase diagram indicates that this is the eutectic composition with very low order-disorder transition temperature. In fact, high *ZT* is observed at $x \sim 0.85$ at 80K (*11*). It is also necessary to analyze three-layer Na_xCoO_2 at $x > 0.8$ because O3-$NaCoO_2$ is 40 meV/FU more stable than P2-$NaCoO_2$, so it is possible that P2-Na_xCoO_2 is metastable at $x > 0.8$ when compared to two phase formation of P2-Na_xCoO_2 and O3-$NaCoO_2$, or a stable three-layer Na_xCoO_2 phase.

4.5.5 Limitations to this work

It is important to note that it is impossible to observe metal-insulator transitions, or a Curie-Weiss metal to spin density wave metal transition (*28*) in both GGA and GGA+U methods, if any occur. Furthermore, magnetic transitions cannot be observed in the phase diagrams because the spins on Co were only allowed to be ferromagnetically aligned in this work. Partial Co charge localization cannot be achieved for itinerant electrons because GGA+U is a static method. Methods such as DMFT (*17*) could be attempted to incorporate effects of partial charge localization, but would be very computationally intensive for phase diagram constructions due to the large number of total energies required.

4.6 Conclusion

The cluster expansion technique and Monte Carlo simulations have been successfully applied to obtain temperature-composition phase diagrams of P2-Na_xCoO_2 in both GGA and GGA+U approximations. A new cluster expansion formalism incorporating long-range electrostatic interactions was used for the first time. The governing interactions between Na^+ are long-range electrostatics in-plane and relaxation effects in the GGA, while Co layer interactions dominate all other interactions such as Na layer interactions in the GGA+U. There are at least ten ground states in the concentration

range $0.5 \leq x \leq 1$ including the two end members in the GGA, compared to only five in the GGA+U. Most order-disorder transition temperatures for ground states are below room temperature in GGA, whereas transition temperatures of ground states are above room temperature in GGA+U. Comparison of Monte Carlo simulation results with experimental data, such as structural transition temperature, Na intercalation/ deintercalation voltage, *c* lattice parameter, and Na1/Na2 ratio, consistently suggest that GGA is a better approximation in the composition range $0.5 \leq x < 0.8$.

4.7 References

1. F. J. DiSalvo, *Science* **285**, 703 (1999).
2. A. F. Ioffe, *Infosearch, London* (1957).
3. D. A. Wright, *Metallurgical Reviews* **15**, 147 (1970).
4. Z. H. Dughaish, *Physica B: Condensed Matter* **322**, 205 (2002).
5. G. Min, D. M. Rowe, *Journal of Materials Science Letters* **18**, 1305 (Aug, 1999).
6. B. C. Sales, D. Mandrus, B. C. Chakoumakos, V. Keppens, J. R. Thompson, *Physical Review B* **56**, 15081 (1997).
7. S. R. Brown, S. M. Kauzlarich, F. Gascoin, G. J. Snyder, *Chemistry of Materials* **18**, 1873 (Apr 4, 2006).
8. C. Delmas, J. J. Braconnier, C. Fouassier, P. Hagenmuller, *Solid State Ionics* **3-4**, 165 (1981).
9. I. Terasaki, Y. Sasago, K. Uchinokura, *Physical Review B* **56**, 12685 (Nov 15, 1997).
10. http://ohtaki.cube.kyushu-u.ac.jp/Ohtaki_Lab/pages/research/TE/oxide.html.
11. M. Lee *et al.*, *Nature Materials* **5**, 537 (Jul, 2006).
12. K. Fujita, T. Mochida, K. Nakamura, *Japanese Journal of Applied Physics* . **40**, 4644 (2001).
13. K. Takada *et al.*, *Nature* **422**, 53 (Mar 6, 2003).
14. M. Menetrier, I. Saadoune, S. Levasseur, C. Delmas, *Journal of Materials Chemistry* **9**, 1135 (May, 1999).

15. C. Delmas, C. Fouassier, P. Hagenmuller, *Physica B & C* **99**, 81 (1980).
16. A. J. Williams, J. P. Attfield, M. L. Foo, L. Viciu, R. J. Cava, *Physical Review B* **73**, 134401 (Apr, 2006).
17. C. A. Marianetti, G. Kotliar, *Physical Review Letters* **98**, 176405 (Apr 27, 2007).
18. Q. Huang *et al.*, *Physical Review B* **70**, 184110 (Nov, 2004).
19. G. J. Shu *et al.*, *Physical Review B* **76**, 184115 (2007).
20. M. Roger *et al.*, *Nature* **445**, 631 (Feb 8, 2007).
21. H. W. Zandbergen, M. Foo, Q. Xu, V. Kumar, R. J. Cava, *Physical Review B* **70**, 024101 (Jul, 2004).
22. J. Geck *et al.*, *Physical Review Letters* **97**, 106403 (Sep 8, 2006).
23. Q. Huang *et al.*, *Journal of Physics-Condensed Matter* **16**, 5803 (Aug 18, 2004).
24. Y. L. Wang, J. Ni, *Physical Review B* **76**, 094101 (Sep, 2007).
25. P. H. Zhang, R. B. Capaz, M. L. Cohen, S. G. Louie, *Physical Review B* **71**, 153102 (Apr, 2005).
26. Y. S. Meng, A. Van der Ven, M. K. Y. Chan, G. Ceder, *Physical Review B* **72**, 172103 (Nov, 2005).
27. Y. S. Meng, Y. Hinuma, G. Ceder, *Journal of Chemical Physics* **128**, 104708 (2008).
28. M. L. Foo *et al.*, *Physical Review Letters* **92**, 247001 (Jun 18, 2004).
29. M. Onoda, T. Ikeda, *Journal of Physics-Condensed Matter* **19**, 186213 (May 9, 2007).
30. T. Motohashi *et al.*, *Physical Review B* **67**, 064406 (Feb 1, 2003).
31. J. Sugiyama *et al.*, *Physical Review B* **67**, 214420 (Jun 1, 2003).
32. L. M. Helme *et al.*, *Physical Review Letters* **94**, 157206 (Apr 22, 2005).
33. S. P. Bayrakci *et al.*, *Physical Review Letters* **94**, 157205 (Apr 22, 2005).
34. H. X. Yang *et al.*, *Solid State Communications* **134**, 403 (May, 2005).
35. T. Motohashi *et al.*, *Physica B-Condensed Matter* **329**, 914 (May, 2003).
36. Y. Y. Wang, N. S. Rogado, R. J. Cava, N. P. Ong, *Nature* **423**, 425 (May 22, 2003).
37. W. Koshibae, K. Tsutsui, S. Maekawa, *Physical Review B* **62**, 6869 (Sep 15, 2000).
38. W. Koshibae, S. Maekawa, *Physical Review Letters* **87**, 236603 (Dec 3, 2001).
39. F. C. Chou, E. T. Abel, J. H. Cho, Y. S. Lee, *Journal of Physics and Chemistry of Solids* **66**, 155 (Jan, 2005).
40. J. Molenda, C. Delmas, P. Dordor, A. Stoklosa, *Solid State Ionics* **12**, 473 (1984).
41. F. C. Chou, J. H. Cho, Y. S. Lee, *Physical Review B* **70**, 144526 (Oct, 2004).

42. P. E. Blochl, *Physical Review B* **50**, 17953 (Dec 15, 1994).
43. G. Kresse, J. Furthmuller, *Computational Materials Science* **6**, 15 (Jul, 1996).
44. J. P. Perdew, K. Burke, Y. Wang, *Physical Review B* **54**, 16533 (Dec 15, 1996).
45. F. Zhou, M. Cococcioni, C. A. Marianetti, D. Morgan, G. Ceder, *Physical Review B* **70**, 235121 (Dec, 2004).
46. F. Zhou, K. Kang, T. Maxisch, G. Ceder, D. Morgan, *Solid State Communications* **132**, 181 (Oct, 2004).
47. K. W. Lee, W. E. Pickett, *Journal of Applied Physics* **99**, 08P702 (Apr 15, 2006).
48. A. I. Liechtenstein, V. I. Anisimov, J. Zaanen, *Physical Review B* **52**, R5467 (Aug 15, 1995).
49. S. L. Dudarev, G. A. Botton, S. Y. Savrasov, C. J. Humphreys, A. P. Sutton, *Physical Review B* **57**, 1505 (Jan 15, 1998).
50. P. D. Tepesch, G. D. Garbulsky, G. Ceder, *Physical Review Letters* **74**, 2272 (Mar 20, 1995).
51. Y. Hinuma, Y. S. Meng, K. Kang, G. Ceder, *Chemistry of Materials* **19**, 1790 (Apr 3, 2007).
52. F. Zhou, T. Maxisch, G. Ceder, *Physical Review Letters* **97**, 155704 (Oct 13, 2006).
53. G. Ceder, G. D. Garbulsky, P. D. Tepesch, *Physical Review B* **51**, 11257 (May 1, 1995).
54. N. Metropolis, A. W. Rosenbluth, M. N. Rosenbluth, A. H. Teller, E.Teller, *Journal of Chemical Physics* **21**, 1987 (1953).
55. Fouassie.C, G. Matejka, J. M. Reau, Hagenmul.P, *Journal of Solid State Chemistry* **6**, 532 (1973).
56. J. Hubbard, *Physical Review B* **17**, 494 (1978).
57. D. Defontaine, G. Ceder, M. Asta, *Nature* **343**, 544 (Feb 8, 1990).
58. D. d. Fontaine, *Journal of Physics-Condensed Matter* **A17**, L713 (1984).
59. J. M. Cowley, *Journal of Applied Physics* **21**, 24 (1950).
60. J. Bursik, *Materials Science and Engineering A* **324**, 16 (Feb 15, 2002).
61. F. C. Chou *et al.*, *arXiv:0709.0085* (2007).
62. C. A. Marianetti, G. Kotliar, G. Ceder, *Nature Materials* **3**, 627 (Sep, 2004).
63. C. Wolverton, A. Zunger, *Physical Review Letters* **81**, 606 (Jul 20, 1998).
64. C. A. Marianetti, G. Kotliar, G. Ceder, *Physical Review Letters* **92**, 196405 (May 14, 2004).
65. A. Van der Ven, M. K. Aydinol, G. Ceder, G. Kresse, J. Hafner, *Physical Review B* **58**, 2975 (1998).

66. G. Ceder, P. D. Tepesch, A. F. Kohan, A. Van der Ven, *Journal of Electroceramics* **1**, 15 (1997).
67. M. de Dompablo, A. Van der Ven, G. Ceder, *Physical Review B* **66**, 64112 (Aug 1, 2002).
68. R. J. Balsys, R. L. Davis, *Solid State Ionics* **93**, 279 (Jan, 1997).
69. I. R. Mukhamedshin, H. Alloul, G. Collin, N. Blanchard, *Physical Review Letters* **93**, 167601 (Oct 15, 2004).
70. Y. Takahashi, Y. Gotoh, J. Akimoto, *Journal of Solid State Chemistry* **172**, 22 (2003).
71. Y. Shao-Horn, L. Croguennec, C. Delmas, E. C. Nelson, M. A. O'Keefe, *Nature Materials* **2**, 464 (Jul, 2003).

Chapter 5 Conclusion

The atomic engineering approach has been applied to the two systems $LiNi_{0.5}Mn_{0.5}O_2$ and Na_xCoO_2 in this research. Monte Carlo simulations, based on a cluster expansion fitted to first principles energies, enabled us to properly determine the thermodynamically stable phases as a function of temperature, and also as a function of Na concentration in Na_xCoO_2.

A binary-ternary cluster expansion, fitted to GGA+U energies, was used to model the cation disorder of $LiNi_{0.5}Mn_{0.5}O_2$. The phase with low (<3%) Li/Ni disorder between the Li-rich and transition metal-rich layers was found to be the thermodynamically stable state below ~600^{o}C. Upon heating above this temperature, the low-temperature phase irreversibly transforms into a phase with high (10~12%) Li/Ni disorder. Monte Carlo simulations has showed why the perfect "flower" ordering with 8.3% Li/Ni disorder has been never observed in experiment by revealing that partial disorder is a central component of the high-temperature phase.

Na_xCoO_2 phase diagrams were constructed based on GGA and GGA+U energies in the concentration range $0.5 \leq x \leq 1$. Holes are delocalized over the Co layer in GGA while the charges on the Co layer are completely localized in GGA+U, forming distinct Co^{3+} and Co^{4+} cations. The most significant interactions in GGA were found to be

long-range in-plane electrostatics and relaxation effects, whereas Co-Co interactions are found to dominate in GGA+U. The ordered structures were all line compounds in GGA, and most ground states had order-disorder transition temperatures below room temperature. In contrast, the ordered phases tolerate some disorder in GGA+U, enabling the transition temperatures to occur above room temperature. Comparison of theoretical ground states, *c*-lattice parameter, and Na1/Na2 ratio with those obtained from experiment consistently suggests that GGA is a better approximation in the range $0.5 \leq x \leq 0.8$. Na_xCoO_2 at the high concentration end ($x > 0.75$) is probably most suitable for thermoelectric applications because of low order-disorder transition temperature, although it is difficult to analyze to what extent disorder in the Na layer leads to high figure of merit in this system.

This research presents three new theoretical advances in the cluster expansion and Monte Carlo technique. First, a cluster expansion in limited phase space was successfully implemented by adding penalties to some ECI. This methodology requires minimum modifications to existing cluster expansion or Monte Carlo codes since only the table of ECIs needs to be changed. Second, an investigation of charge balance in constrained open systems was conducted by removing one point cluster in the coupled cluster expansion, and appropriately selecting the perturbation in the Monte Carlo simulations. Thirdly, long-range electrostatic interactions were successfully accounted for in the Na_xCoO_2 cluster expansion for GGA energies. The first principles energies were

separated into contributions from long-range interactions and short-range interactions. The energies associated with long-range interactions were obtained by using pair ECI, which correspond to electrostatic interactions that are defined beforehand. The remaining energies were fit in a manner that allowed us to obtain ECI of a cluster expansion, which includes only short-range clusters. The two sets of ECI are then added together to recover the ECI for the first principles energies.

Chapter 6 Ideas for future work

6.1 General ideas

The atomic engineering approach is limited to systems where cluster expansion is feasible. These systems must have few symmetrically non-equivalent disorder sites such as relatively high symmetry crystalline materials. Second, systems with too large a unit cell size (>200 atoms per unit cell) consume an inordinate amount of computation time (at the time of writing this thesis, a 150-atom unit cell calculation takes about 4 days with 12 to 16 CPUs). Thirdly, to ensure that the ground states are accurately reproduced in the cluster expansion, systems with many ground states in a small concentration range (e.g. “devil’s staircase” situations) and systems with near-degenerate ground states should be avoided. These restrictions may become less stringent with further improvement in cluster expansion methodology.

Obtaining accurate energies in a timely manner is quite difficult to do for some systems. In addition, difficulties arise because DFT methods are static and cannot correctly treat systems where correlated electron dynamics is important. Furthermore, partial charge localization cannot be exactly treated with GGA or GGA+U because the electron distribution is overdelocalized in the former and overlocalized in the latter.

Improvement to techniques that implement DFT, or more generally to total energy calculation theory is necessary in these cases.

The time necessary to compile a phase diagram should decrease with improvement in cluster expansion methodology and expertise. Currently, the majority of time is taken up by repeated need for first principles energy computation of relevant structures suggested by the cluster expansion. Therefore finding a more efficient way to choose structures, and/or weights to converge the cluster expansion with fewer number of iterations. would greatly reduce the time it takes to create an accurate cluster expansion.

The possibility of automated atomic engineering should be discussed as a means to improve speed and understanding of this methodology. Currently, ideas for ground state candidates and necessary interactions are based on physical intuition, however automated comparison with a database containing results of many applications of atomic engineering may be possible. Implementing automatic detection of new ground state candidates and relevant excitations from snapshots of Monte Carlo simulation is a difficult task at this time, but this could be realized with advances in image recognition technology.

6.2 System specific ideas

Successful development of experimental processing techniques to form the low temperature phase of $LiNi_{0.5}Mn_{0.5}O_2$ quickly, cheaply, and in large batches will have tremendous impact. Currently the low temperature phase is being formed by ion exchange from $NaNi_{0.5}Mn_{0.5}O_2$, however this takes time and is currently successful in only batches of ~1g.

Obtaining a cluster expansion of $Li_xNi_{0.5}Mn_{0.5}O_2$ ($0 \leq x \leq 1$) to compile a phase diagram may seem like a natural improvement over the $LiNi_{0.5}Mn_{0.5}O_2$ cluster expansion. However, the simplest form of a cluster expansion in $Li_xNi_{0.5}Mn_{0.5}O_2$ is a ternary-ternary-quaternary cluster expansion. The Li layer has ternary disorder (Li, Ni, vacancies) and the TM layer has quaternary disorder (Li, Ni, Mn and vacancies). Furthermore, upon delithiation from $LiNi_{0.5}Mn_{0.5}O_2$ some tetrahedral sites are occupied that have ternary disorder (Li, Ni, vacancies), which result in a large number of structures that need to be fit to this cluster expansion. In addition, it may be necessary to treat Ni with different valences (Ni^{2+}, Ni^{3+}, and Ni^{4+}) as different species. In order for such a cluster expansion to be possible, significant, substantial, or even drastic increase in computational speed would be necessary for the project to finish within a reasonable period of time. A related system of interest would be $LiNi_{1/3}Co_{1/3}Mn_{1/3}O_2$, however this

system is difficult to computationally analyze because GGA+U more accurately approximates Ni and Mn oxide systems, but GGA describes Co oxide systems better.

There are two main ideas for future work in Na_xCoO_2. First, the phase diagram for the remaining concentration range in P2-Na_xCoO_2 ($0 \leq x \leq 0.5$) should be obtained. At the low Na concentration end, it is expected that no Na1 sites be occupied at low temperatures because the distance between Na are large enough such that there is no energetic incentive to situate Na in high-energy Na1 sites because electrostatic repulsion is minimal. Second, obtaining the phase diagram of O3-Na_xCoO_2 is necessary to determine the optimum Na content for a thermoelectric material. Construction of the cluster expansion should be simpler than compared to P2-Na_xCoO_2 because there is only one symmetrically different Na site in O3-Na_xCoO_2 compared to two in P2-Na_xCoO_2. However, since the primitive cell of O3-Na_xCoO_2 is 1.5 times larger than in P2-Na_xCoO_2, computation time to obtain first principles energies will be significantly longer.